CHARGE TRANSPORT IN MIX-CONDUCTING HETERO-IONIC JUNCTIONS OF POLYACETYLENE IONOMERS

by

FUDING LIN

A DISSERTATION

Presented to the Department of Physics
and the Graduate School of the University of Oregon
in partial fulfillment of the requirements
for the degree of
Doctor of Philosophy

June 2009

University of Oregon Graduate School

Confirmation of Approval and Acceptance of Dissertation prepared by:

Fuding Lin

Title:

"Charge Transport in Mix-Conducting Hetero-ionic Junctions of Polyacetylene Ionomers"

This dissertation has been accepted and approved in partial fulfillment of the requirements for the degree in the Department of Physics by:

J David Cohen, Chairperson, Physics
Mark Lonergan, Advisor, Chemistry
Roger Haydock, Member, Physics
David Strom, Member, Physics
David Tyler, Outside Member, Chemistry

and Richard Linton, Vice President for Research and Graduate Studies/Dean of the Graduate School for the University of Oregon.

June 13, 2009

Original approval signatures are on file with the Graduate School and the University of Oregon Libraries.

An Abstract of the Dissertation of

Fuding Lin for the degree of Doctor of Philosophy

in the Department of Physics to be taken June 2009

Title: CHARGE TRANSPORT IN MIX-CONDUCTING HETERO-IONIC

JUNCTIONS OF POLYACETYLENE IONOMERS

Approved: _____

Dr. Mark C. Lonergan

Experimental studies on mix-conducting hetero-ionic junctions of anionically (PA_A) and cationically (PA_C) functionalized polyacetylene ionomers, as well as each individual ionomer, in thin-film sandwich configurations are reported for the purpose of better understanding the interaction between ionic and electronic charge transports in mixed ionic-electronic conductor (MIEC) systems.

The transport of ions in both individual ionomers as well as their hetero-ionic junction was investigated via small-amplitude AC impedance spectroscopy in the absence of significant interference from the electronic charge transport. Modeling of the impedance results reveal important information about the materials such as: ion conductivity, activation energy of ion conduction, ion hopping frequency, dielectric constant, interfacial capacitance, and estimates of effective ion density.

Electrochemical injection of electronic charge carriers into PA_A and PA_C from gold electrodes was monitored to determine the applied potentials needed to drive hole and electron injection into each ionomer. It is found that for both ionomers, the onset voltages for unipolar and bipolar charge injection are similar, and holes can be injected at close to zero bias.

The responses of the complete $Au|PA_A|PA_C|Au$ hetero-ionic junction, as well as each constituent ionomer layer in $Au|Ionomer|Au$ configuration, to various stepping biases were investigated through current-voltage and impedance measurements to study the origin of the asymmetric current-voltage response observed in the hetero-ionic junction. Analysis of the results reveal a working mechanism of a mix-conducting junction that is fundamentally different from that of a purely electronic pn junction.

When illuminated with light, the $Au|PA_A|PA_C|Au$ junction exhibits unidirectional photovoltage and photocurrent with the PA_A side at higher potential, while the $Au|PA_A|Au$ and $Au|PA_C|Au$ samples exhibit symmetric photoresponses. The efficiency of photocurrent generation in the $Au|PA_A|PA_C|Au$ junction was found to be strongly dependent on the direction of illumination and on the sample thickness. These observations can be explained by the difference in the mobility of holes and electrons and the existence of a built-in ionic space charge region at the $PA_A|PA_C$ interface. A mechanism of photoresponse unique to MIEC junctions was proposed, and the magnitude of built-in potential was estimated.

CURRICULUM VITAE

NAME OF AUTHOR: Fuding Lin

PLACE OF BIRTH: Fujian, P. R. China

DATE OF BIRTH: November, 1975

GRADUATE AND UNDERGRADUATE SCHOOLS ATTENDED:

  University of Oregon, Eugene, Oregon, USA
  Xiamen University, Xiamen, Fujian, China

DEGREES AWARDED:

  Doctor of Philosophy in Physics, 2009, University of Oregon
  Bachelor of Science in Physics, 1997, Xiamen University

AREAS OF SPECIAL INTEREST:

  Organic semiconductor device physics
  Mixed ionic-electronic conductors

PROFESSIONAL EXPERIENCE:

  Research assistant, Lonergan lab, University of Oregon, 2003–2009
  Teaching assistant, Dept. of Physics, University of Oregon, 2001–2003
  Teaching assistant, Dept. of Physics, Xiamen university, 1999-2001

PUBLICATIONS:

Fuding Lin, Yongjun Wang, and Mark C. Lonergan, "Ion transport in polyacetylene ionomers", J. Appl. Phys. 104, 103517 (2008).

Fuding Lin and Mark C. Lonergan, "Gate electrode processes in an electrolyte-gated transistor: non-Faradaically versus faradacially coupled conductivity modulation of a polyacetylene ionomer", Appl. Phys. Lett. 88(13), 133507/1-133507/3 (2006).

Calvin H. W. Cheng, Fuding Lin, and Mark C. Lonergan, "Charge Transport in a Mixed Ionically/Electronically Conducting, Cationic, Polyacetylene Ionomer between Ion-Blocking Electrodes", J. Phys. Chem. B 109(20), 10168-10178 (2005).

ACKNOWLEDGMENTS

This work would not have been possible without the continuous support and guidance from my adviser Dr. Mark C. Lonergan. During the past several years I've benefitted immensely from working with an open-minded, intelligent, and resourceful advisor like Mark. The friendly and supportive atmosphere that Mark has created and maintained in his group has made my pursuit of a doctoral degree a wonderful experience.

I want to take this opportunity to thank Dr. Calvin H.W. Cheng for teaching me several experimental techniques that are very important for my project, and Dr. Lei Gao for guiding me through the synthesis of anionic ionomers. I would like to thank Dr. Yongjun Wang, Dr. Dean H. Johnston, David Stay, Ian Moody, Ethan Walker, Chris Weber, T. J. Mills, Stephen Robinson, and other Lonergan group members for their invaluable friendship and for generously sharing with me their knowledge and experience about things that matters in my life. It was a great pleasure to work with these warm hearted and talented people.

I also want to thank my wife, Yan Xiong, for her love. I'm truly grateful for her decision to put off her own career and take care of our kids during my pursuit of a Ph.D. degree. A special thank you goes to my beloved parents who worked very hard to make sure that I get a college education and inspired me to strive for the best.

To my wife Yan Xiong,

and our family.

TABLE OF CONTENTS

LIST OF FIGURES

CHAPTER I

INTRODUCTION

In this chapter, I will first introduce the topic of this dissertation and explain its relevance to current efforts in developing the organic counterparts of silicon-based semiconductor devices, which has played a crucial role in the modernization of our society. Then I will define the goal of this dissertation and describe the approaches used towards achieving this goal. An overview of the dissertation is given at the end of this chapter.

1.1 Organic semiconductor devices and the role of polyacetylene ionomers

Semiconductor devices have been essential to the improvement of technologies during the last few decades of our civilization. They are at the heart of almost every modern electronic devices like personal computers and cell phones. Since the early days of semiconductor devices, inorganic materials represented by silicon and germanium have been the focus of intense research efforts. However, thanks to the major discovery in 1977 by Chiang et al. that the electronic conductivity of polyacetylene can be continuously changed from insulating to metallic through chemical doping,[1] more and more attention have been paid to a new class of carbon-based materials called "organic semiconductors". The fast growing interest in organic semiconductors is largely driven by the comparative advantages of these materials over their traditional inorganic counterparts, such as low-cost processing, mechanical flexibility, and the vast possibilities to tailor specific properties of the material through organic synthesis. This new class of materials could play important roles

$$\overset{-}{SO_3}\overset{+}{NMe_4} \qquad \overset{-}{CF_3SO_3}\overset{+}{NMe_3}$$

PA$_A$ PA$_C$
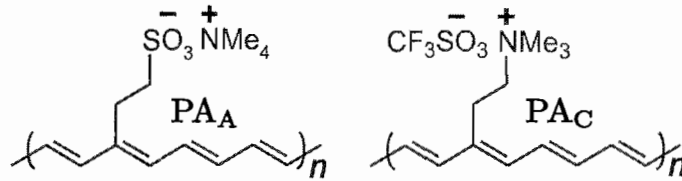
FIGURE 1.1: Chemical structure of polyacetylene ionomers PA$_A$ and PA$_C$

in future technologies like lighting,[2, 3, 4, 5] solar energy conversion,[6, 7, 8, 9, 10] and flexible electronics.[11, 12, 13, 14]

In the development of organic semiconductor devices, the ability to form stable *pn* junctions between dissimilarly doped materials is of vital importance, and such stable junctions can be formed only if the dopants can be immobilized. For inorganic semiconductors, this was achieved by exploiting the strong temperature dependence of dopant mobility, i.e. introducing dopant atoms at high temperature and then cool down the material to immobilize those dopant atoms. For organic semiconductors, there are multiple approaches to immobilize the dopants. One of which is the same as that being used for silicon *pn* junctions — establish an in-situ *pn* junction at a temperature when the dopant mobility is high, then freeze the dopants in place by quickly lowering the temperature.[15, 16] The drawback of this approach is the limited temperature range within which the device thus fabricated can function.

Another approach takes advantage of a special type of material called a "conjugated ionomer" or "conjugated polyelectrolyte",[17] where the charge compensating dopant ions are covalently attached the the host polymer martix. Two interesting examples of conjugated ionomers are the anionically and cationically functionalized polyacetylene, PA$_A$ and PA$_C$, respectively, that are shown in Figure-1.1. In these two ionomers, an ionic functional group is attached to the conjugated backbone during the synthesis, the conjugated backbone provides the pathway for electronic carriers, while the unattached ions are free to move within the polymer matrix, making the material a mixed ionic-electronic conductor(MIEC) in its intrinsic

state. When the mobile counterions are completely replaced by electronic charge carriers of the same sign, the material is doped to its fully-internally-compensated (FIC) state and becomes a purely electronic conductor. The ionomers in FIC states can be either p-doped(for an anionic ionomer) or n-doped (for a cationic ionomer) depending on the charge of the bonded ions. Since the dopant ions are immobilized, when two dissimilarly doped ionomers in FIC states are put into contact, they are able to form a stable pn junction that exhibits rectifying I-V. [18]

The ability of polyacetylene ionomers to form purely electronic pn junction in its FIC state is desirable. However, the mix-conducting nature of polyacetylene ionomers in its undoped or partially doped state is a complex system of great interest by itself. Such so called "Mixed Ionic-Electronic Conductor (MIEC) systems" have attracted much attention due to their intriguing properties. For instance, it was found that in MIECs, the onset of charge injection happens at close to the bandgap voltage and shows little dependance on electrode work function.[3] Furthermore, an asymmetric current-voltage response was reported in a hetero-ionic junction of undoped anionic and cationic polyacetylene ionomers,[19] and photovoltaic response was observed in an undoped hetero-ionic MIEC junction between DPAS$^-$Na$^+$ and $[\mathrm{Ru(bpy)_3}]^{2+}(\mathrm{PF_6^-})_2$.[20] It is generally agreed that the interaction between ionic charge transport and electronic charge transport in these MIEC systems plays a crucial role in the system's response, but the details of the interaction remains largely controversial. Better understanding of how MIEC systems work is essential to further utilizing the novel features of these complex systems.

The coexistence of ionic and electronic conductivity within a single phase makes polyacetylene ionomers a valuable platform for studying mixed conduction in MIEC system. In this work, I hope to make my contribution to the understanding of charge transport in MIEC systems and their junctions, through a series of experiments carried out on devices based on polyacetylene ionomers.

1.2 Charge transport in mix-conducting hetero-ionic junction: existing hypotheses

The focus of this dissertation is to understand the mechanism of asymmetric charge transport through the mix-conducting $Au|PA_A|PA_C|Au$ hetero-ionic junction, as illustrated in Fig-1.2.
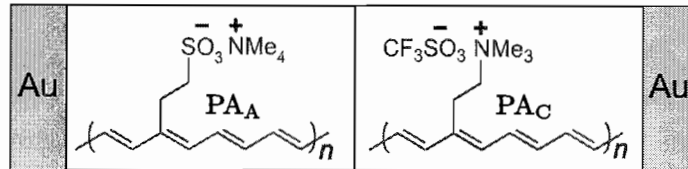
FIGURE 1.2: Schematic of the polyacetylene hetero-ionic junction with electrodes.

Up to date, there has been relatively few published studies on the subject of charge transport in mix-conducting hetero-ionic junctions. More efforts have been focused on purely electronic junctions such as silicon pn junction, purely ionic junctions such as bipolar membranes,[21] and membrane-separated redox junctions[22] resembling batteries where no continuous current could be sustained at steady state. The lack of more detailed studies on mix-conducting hetero-ionic junctions likely contributed to the fact that the working mechanism of such junction is still not well understood. So far two hypotheses has been proposed.

1.2.1 The asymmetric injection hypothesis

In 2004, Cheng et al. first reported the observation of unidirectional current in a mix-conducting polyacetylene hetero-ionic junction.[19] The authors hypothesized that the asymmetry in the MIEC junction's I-V response is the result of an asymmetry in the charge injection process at the two electrode|ionomer interfaces due to (1) difference in interfacial capacitances of ionic double layers formed at different electrode surfaces and (2) only holes can be injected into PA_A. The proposed working

mechanism is illustrated in Figure-1.3. This hypothesis will be called the "asymmetric injection" hypothesis based on the underlying assumptions.
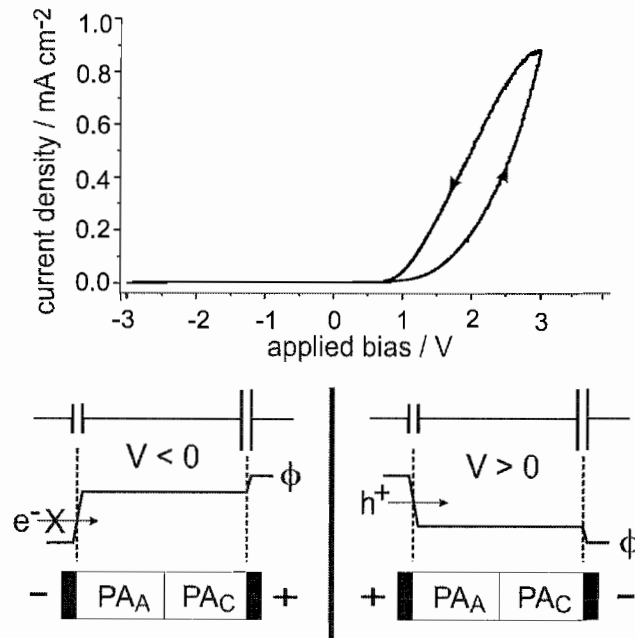
FIGURE 1.3: Working mechanism of the polyacetylene hetero-ionic junction according to the asymmetric injection hypothesis. For both forward and reverse bias, applied potential drops almost entirely on the Au|PA_A interface. At forward bias(Right), hole injection was enhanced, while at reverse bias(Left), electron injection into PA_A could not happen due to special property of PA_A.

Two previous experimental results are central to this hypothesis: (i) The capacitance of the Au|PA_C interface was estimated to be much larger than that of the Au|PA_A interface,[23] and (ii) PA_C can be both reversibly p and n doped through electrochemistry, but only reversible p doping of PA_A was observed.[24] According to this hypothesis, the PA_A|PA_C interface does not play a crucial role and can be omitted for simplicity. Because of (i), the applied potential will drop almost entirely at the Au|PA_A interface. At forward bias (see right half of Fig-1.3) the large potential drop at the Au|PA_A interface drives hole injection into PA_A and eventually electron injection into PA_C as well. The bipolar injection allows the total amount of electronic

charge carriers in the junction to be substantially increased to improve the overalll conductivity of the junction. At reverse bias (see left half of Fig-1.3), however, the large potential drop at Au|PA$_A$ interface does not lead to electron injection into PA$_A$ as implied by (ii), consequently only a limited amount of holes can be injected into the PA$_C$ layer. The unipolar electronic charge injection at reverse biases limits the total amount of charge carriers in the junction and leads to much lower current than at forward biases.

1.2.2 The ionic P-N junction hypothesis

Later in 2006, another work on MIEC hetero-ionic junction was reported by Bernards et al.. Asymmetric current-voltage response and light emission as well as photovoltaic response was observed from a ITO|DPAS$^-$Na$^+$|[Ru(bpy)$_3$]$^{2+}$(PF$_6^-$)$_2$|Au junction.[20] The authors proposed a different working mechanism which will be called the "ionic P-N junction" hypothesis, as illustrated in Fig-1.4, to explain the origin of these observations.

According to the "ionic P-N junction" hypothesis, the equilibration of mobile charges between the two constituent MIECs is analogous to what happens in a silicon pn junction except that holes and electrons are now replaced by mobile Na$^+$ ions and mobile PF$_6^-$ ions. The junction is thus termed an "ionic P-N junction" by the author. As a result of the mobile ion equilibration, an electric field was set up by uncompensated ionic charges across the DPAS$^-$Na$^+$|[Ru(bpy)$_3$]$^{2+}$(PF$_6^-$)$_2$ interface to balance the diffusion current of mobile ions. This built-in field also sets up a barrier for hole transport from DPAS$^-$Na$^+$ into [Ru(bpy)$_3$]$^{2+}$(PF$_6^-$)$_2$ and vice versa for electrons.

At forward bias, the built-in field is suppressed and the barrier for hole injection into [Ru(bpy)$_3$]$^{2+}$(PF$_6^-$)$_2$ is reduced, at the same time the injection of holes from ITO electrode into DPAS$^-$Na$^+$ is enhanced by increased potential drop across that interface. The electron transport is enhanced in a similar way, thus the overall
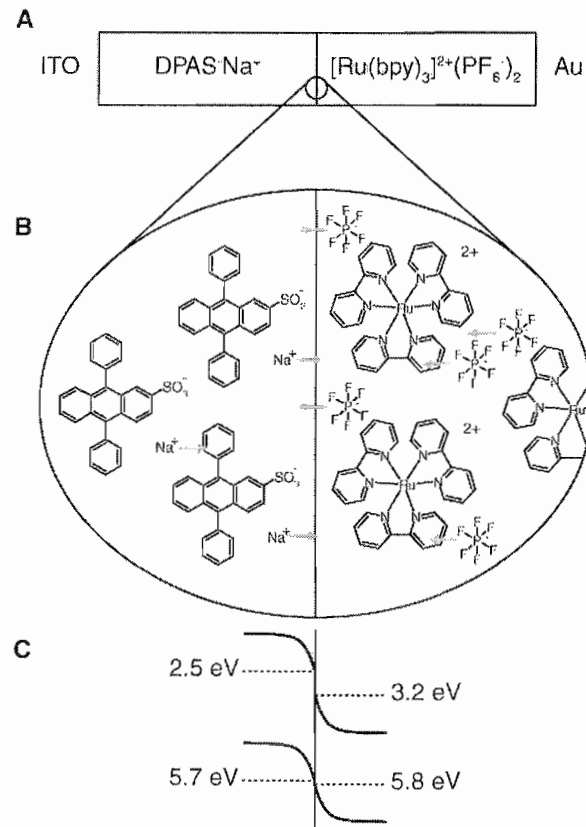
FIGURE 1.4: Schematic of the ITO|DPAS$^-$Na$^+$|[Ru(bpy)$_3$]$^{2+}$(PF$_6^-$)$_2$|Au ionic junction according to Bernards et al.. (A) The device structure. (B) Details at the junction interface. (C)Relevant energy levels before (dotted lines) and after(solid lines) contact.

current is increased and light is emitted from the recombination of injected holes and electrons. Reverse bias increases the magnitude of the built-in field across the DPAS$^-$Na$^+$|[Ru(bpy)$_3$]$^{2+}$(PF$_6^-$)$_2$ interface and as a consequence, only a small portion of the applied potential drops at the electrode interfaces to help electronic carrier injection. The poor injection at reverse bias leads to lower overall current than forward bias.

When the junction is illuminated, the built-in electric field assists in the dissociation of excitons and the separation of holes and electrons, which leads to the observation of a photovoltaic response.

1.3 Testing the hypotheses

The two different hypotheses described in the previous section both seemed capable of explaining what was observed in the corresponding system. One question that naturally arises, is whether the two systems are indeed so different that they entail drastically different working mechanisms, or, since both systems are examples of the same broader family of MIEC junctions, they share the same fundamental working mechanism and only differ at the level of specific details inherent to each system.

Two specific details might be important. The first detail is about the MIEC|MIEC inteface. The $ITO|DPAS^-Na^+|[Ru(bpy)_3]^{2+}(PF_6^-)_2|Au$ was fabricated by soft lamination of the two constituent layers, which supposedly produces an abrupt junction interface. Whereas the $Au|PA_A|PA_C|Au$ junction was fabricated by spin-coating PA_A on top of a dried PA_C layer, taking advantage of the fact that the solvent in PA_A solution doesn't dissolve PA_C. Due to the possibility that PA_C could be swelled during the deposition of PA_A layer, the resulting junction interface could have a significantly larger effective area than that of an abrupt junction.

The second detail is that for the $Au|PA_A|PA_C|Au$ junction, it was believed that only holes can be reversibly injected into PA_A while both electrons and holes can be injected into PA_C, but otherwise the two ionomers have similar electronic energy levels as implied by similarities in their optical absorbtion spectrum (see Fig-1.5) and oxidative doping potential.

One major difference between the two hypotheses is the role of the MIEC|MIEC interface. In the "asymmetric injection" hypothesis, the MIEC|MIEC interface was considered unimportant to the asymmetric I-V response, while in the "ionic P-N junction" hypothesis, the MIEC|MIEC interface was considered the source of the observed asymmetries in the device's response to applied bias and illumination.

It is important to point out that the "asymmetric injection" hypothesis does not preclude the existence of a built-in field across the MIEC|MIEC interface,
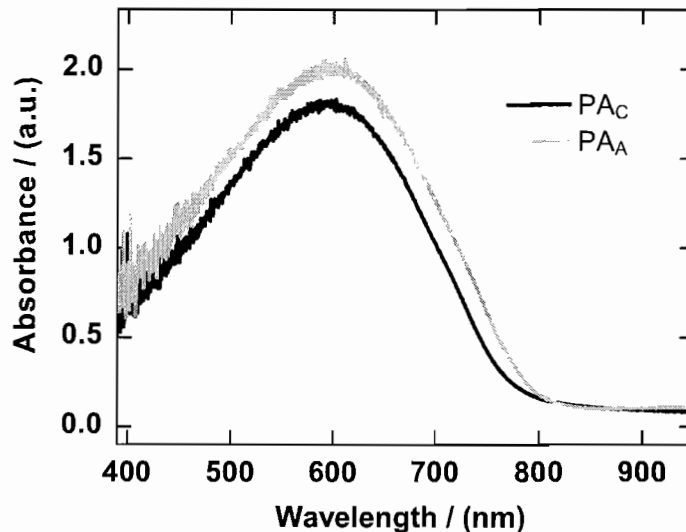
FIGURE 1.5: The UV-Visible optical absorbtion spectrum of PA_A and PA_C.

since the existence of such a built-in field will indeed strengthen the asymmetric response according the hypothesis. It is possible that due to the spin-coating process, the $PA_A|PA_C$ interface was indeed quite rough and therefore has a much higher capacitance than both the $Au|PA_A$ interface and the $Au|PA_C$ interface. In such case the $PA_A|PA_C$ interface would still be relatively unimportant even if a built-in electric field exist.

The situation in the "ionic P-N junction" hypothesis was complicated by the existence of another asymmetry in the junction – the specific energy level alignment of the two materials already implies a low barrier for hole transport from $DPAS^-Na^+$ into $[Ru(bpy)_3]^{2+}(PF_6^-)_2$ and a higher barrier for electron transport in the other direction. This additional asymmetry could give rise to similar observations.

Considering the above details, the following additional experiments will be helpful to our further understanding of the MIEC junction:

Expt-A: *Photovoltaic response of a MIEC junction that has negligible electronic energy level asymmetry, or a weak asymmetry that is in the opposite direction of the hypothesized ionic P-N junction.*

Expt-B: *A comparison of injected charge carriers between forward and reverse bias.*

Expt-C: *Measurement of capacitance ratios among the three interfaces involved in the "asymmetric injection" hypothesis, through an independent method.*

If a photovoltaic response is observed in **Expt-A**, the existence of a built-in electric field according to the "ionic P-N junction" hypothesis will be strongly supported. On the other hand, the result of **Expt-B** will be a direct test of the difference in the amount of injected charged carriers predicted by both hypotheses, and the result of **Expt-C** will be an independent verification of the "asymmetric injection" hypothesis. Since PA_A and PA_C have similar electronic energy levels, all of the above experiments could be conducted on the $Au|PA_A|PA_C|Au$ system.

1.4 Dissertation overview

The reminder of this dissertation is organized as following. Chapter-II focus on the characterization of ionic charge transport in PA_A and PA_C as well as in the complete junction via small amplitude ($\leq 50mV$) AC impedance spectroscopy. The work in this chapter provides important information about the ionic aspects of the system such as the ionic conductivity, the capacitance of each interface, the effective ion density, and the ion hopping frequency.

Then the electronic charge injection processes for both ionomers are investigated in Chapter-III, by isolating the injection process from the electronic conduction process through the use of separating electrolyte. The results in this chapter will provide answers to important questions such as, what are the onset voltages of hole and electron injection into PA_A and PA_C from Au electrode, how the injected charge carriers are balanced, and how the materiail's electronic conductivity is influenced by the electronic charge carrier injection.

In Chapter-IV and Chapter-V, steady state and time dependent current-voltage measurements on $Au|PA_A|PA_C|Au$, $Au|PA_A|Au$, and $Au|PA_C|Au$ under various

conditions are conducted to learn how ionic and electronic charge transport interact with each other. The results from these two chapters will provide information on how the system evolves under different applied bias, the amount of charge carriers being injected at each bias, how strongly they affect the overall current, and the likely concentration profile of ionic charge carriers at steady-state. These information will be used to identify the origin of the $Au|PA_A|PA_C|Au$ junction's asymmetric current-voltage response.

The photovoltaic response of $Au|PA_A|PA_C|Au$ as well as each individual ionomer with Au electrodes are presented in Chapter-VI, with a proposed mechanism that is unique to MIEC junctions to explain the observations.

Finally, results are summarized and future works suggested in Chapter-VII.

CHAPTER II

CHARACTERIZATION OF ION TRANSPORT THROUGH IMPEDANCE SPECTROSCOPY

In this chapter, the ionic charge transport in both PA_A and PA_C will be investigated through small amplitude ($\leq 50mV$) AC impedance spectroscopy. The use of a small amplitude signal is intended to minimize the interference from electronic charge transport. By analyzing the impedance data, we will be able to obtain important information about ionic transport in each ionomer, such as the ionic conductivity, the ionic double layer capacitance, the effective ion density, the dielectric constant of the polymer matrix, and the ion hopping frequency. Small amplitude impedance measurements on $Au|PA_A|PA_C|Au$ samples are also conducted and compared to individual ionomers.

2.1 Introduction

Undoped conjugated ionomers such as PA_A and PA_C are important to the study of electronic devices based on polymeric mixed ionic/electronic conduction. These polyacetylene ionomers have been used to explore the fundamentals of conjugated ionomer electronics. For instance, they have been used in developing a conjugated polymer pn junction[18] and in the observation of unidirectional current flow in a so-called hetero-ionic junction.[19]

The ionic charge transport in these mix-conducting materials play a crucial role in determining their chemistry, electronic properties, and device physics. In Chapter-I we have seen that one important assumption in the "asymmetric injection" hypothesis is the asymmetry in ionic double layer polarization between PA_A and PA_C, but the

double layer capacitance was estimated through discharging measurements – a rather indirect method that could be complicated by the presence of injected electronic charges. A careful study on the fundamentals of ion motion through these materials could be very helpful in understanding the device physics of the MIEC hetero-ionic junction.

Additionally, due to the fact that both PA_A and PA_C are X-ray amorphous materials in their glassy states,[25] these materials provide an interesting bridge between traditional crystalline solid ionic conductors[26, 27] and high performance polymer electrolytes exhibiting high ionic conductivities above their glass transition temperatures.[28, 29, 30, 31] They are perhaps most comparable to ionically conducting inorganic glasses, where there has been substantial work on transport mechanisms and on the interpretation of their dielectric response.[32]

Small amplitude impedance spectroscopy presents an ideal tool for the study of ion transport in these mix-conducting ionomers. Substantial ion polarization in these materials is known to facilitate charge injection into the material, therefore the small amplitude is desirable since the effect of charge injection is thus minimized and complication of results avoided. Furthermore, the methods for analyzing impedance data from ion conducting materials have been well established.

2.2 Experimental details

2.2.1 Materials

The mostly trans form poly[2-cyclooctatetraenylethyltrimethylammonium triflate], PA_C, and poly(tetramethylammonium 2-cyclooctatetraenylethanesulfonate), PA_A, were synthesized using the methods described in a previous study.[33] The non-ionic control material poly(trimethylsilylcyclooctatetraene) was synthesized as described in the literature.[34] Polymer structure was confirmed by ^{1}H NMR and
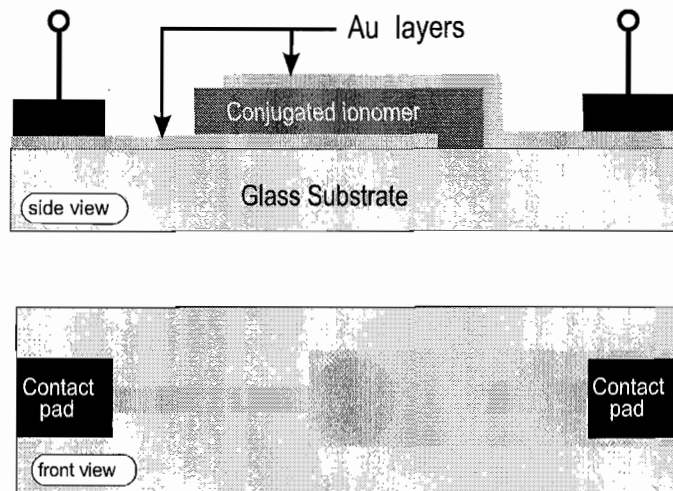
FIGURE 2.1: Schematic of a single layer ionomer in sandwich geometry

UV/vis spectroscopy. Acetonitrile was distilled and freeze-pump-thaw degassed prior to use. Anhydrous dimethylformamide and methanol (Aldrich) were filtered through teflon membrane filters (0.2 μm) before use.

2.2.2 Sample preparation

The Au|Ionomer|Au sandwich structures were prepared on glass-slide substrates. A schematic of a complete sample is shown in Fig-2.1 for a single layer structure. The glass slides were cleaned by first soaking them in concentrated HCl for at least 4 hours followed by a thorough rinse with deionized water. Bottom electrodes were prepared by sequential thermal evaporation of a Cr adhesion layer (3 nm) followed by an Au layer (12 nm) onto the glass slides. A circular electrode area of $A = 0.12$ cm^2 was defined by using a physical evaporation mask. During the fabrication of single layer devices, polymer films were deposited onto the bottom gold electrodes via spin-coating from a 10 mg/ml solution of either PA$_C$ in dimethylformamide or PA$_A$ in methanol. During the fabrication of bi-layer ionomer junctions, a layer of PA$_A$ was

spin-coated on top of a dried PA_C layer. After spin-coating, the excess material outside of the predefined electrode area was carefully removed. The thickness of the film was controlled by varying the spin speed and was measured using a Dektak–6M profiler at 10mg stylus force. After spin-coating, films were dried under vacuum (20 mTorr) for at least 4 hours. A 15-nm-thick Au layer was then thermally evaporated onto the polymer film to complete the sandwich structure. The top Au contact was evaporated at a rate of at least 10nm/min, and the substrate temperatures was typically below 40°C during evaporation. Electrical contacts to the electrodes were made by silver printing tinned-copper wires onto the contact pads of the metal films. Epoxy was then used to strengthen each contact. After thermal evaporation of the top contact, all samples were stored under vacuum (20 mTorr) for at least 4 hours and then annealed at 125°C under active vacuum for 8 hours to drive out residual solvent. UV-Vis spectroscopy was used to monitor any change in the material due to annealing and minimal changes were observed.

2.2.3 Impedance measurements

The sample in sandwich geometry was put into a stainless steel container fitted with electrical feedthroughs and a valve for evacuation. After contact wires were attached to the sample and a thermocouple fixed to the surface of the glass substrate, the container was evacuated to less than 20 mTorr and then kept under active vacuum during the annealing process and throughout the dielectric measurements. The temperature of the sample was controlled by a SUN EC10 Environmental Chamber. A Solartron SI-1296A dielectric interface in combination with a Solartron SI-1260 impedance analyzer was used for all dielectric measurements. The SMART software from Solartron Analytical was used for interfacing both the SI-1296A and the SI-1260. The amplitude of the voltage signal was 10 mV for PA_A and 50 mV for PA_C and $PA_A|PA_C$ junction. The measurements were independent of drive amplitude over the range 10-100 mV. Exposure to acetonitrile vapor was accomplished under passive
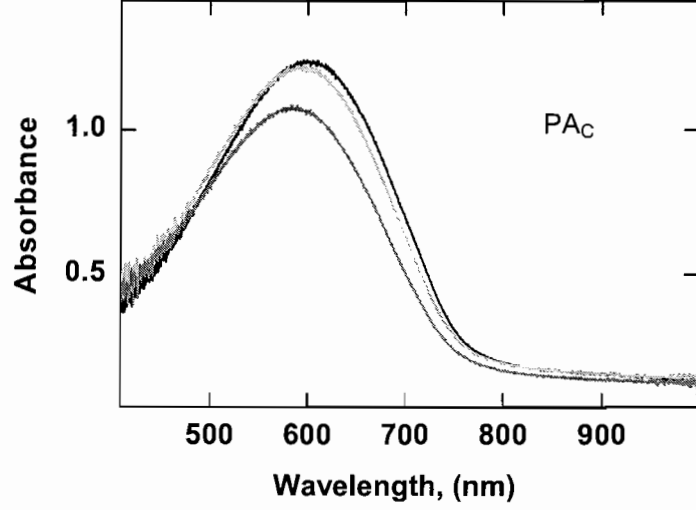
FIGURE 2.2: The change in UV/Vis spectra of a PA_C sample with thermal history. The sample was annealed under active vacuum (P < 20 mTorr). *black line*: before annealing, *red line*: after annealing at 398K for 10 hours, *blue line*: after annealing at 398K for 10 hours and 408K for 10 hours.

vacuum by exposing the sample chamber to acetonitrile vapor from a reservoir of degassed liquid acetonitrile.

The apparent relative permittivity, $\epsilon_{app} = \epsilon'_{app} - i\epsilon''_{app}$, and conductivity, $\sigma_{app} = \sigma'_{app} + i\sigma''_{app}$, were calculated from the raw complex impedance Z in the standard manner: $\epsilon_{app} = \sigma_{app}/i\omega\epsilon_0 = L/i\omega AZ\epsilon_0$, where ϵ_0 is the vacuum permittivity. The dielectric loss tangent, $\text{Tan}\,\delta = \epsilon''_{app}/\epsilon'_{app} = \text{Tan}(\theta + \pi/2)$ where θ is the measured phase angle, was also calculated. The capacitance of the sample is usually expressed in terms of capacitance per unit area, $Farad/cm^2$.

2.3 Results from single layer samples

Dielectric spectra were collected for PA_C and PA_A thin films sandwiched between gold electrodes. The spectra were collected over the temperature range of 298K to 398K and with thicknesses ranging from 155 nm to 1740 nm for PA_A and 150 nm to 835 nm for PA_C. The temperature range was dictated by the measurable

impedance on the low end and by stability on the high end. At temperatures higher than 408K, noticeable degradation of the cell impedance and absorption spectrum of the polymer were observed (see Fig-2.2). The range over which high quality thin films could be reproducibly fabricated dictated the thicknesses studied. In this study, the change of sample thickness L due to thermal expansion was assumed negligible based on the fact that the thermal expansion coefficient of similar polymers is on the order of 10^{-4} mm/mm/K. [35] Although the diffusion of Au into the polymer during top contact evaporation could be significant for thin films under certain evaporation condition,[36, 37] it was considered negligible in this study based on the fast evaporation rate($\geq$10nm/min) and low substrate temperature ($<$40°C) during our evaporation process. The lack of apparent thickness dependance in the calculated high frequency limiting dielectric constant also supports this assumption.

2.3.1 The effect of residual solvent and reproducibility of data

During the early exploration of the impedance experiments, it was found that residual solvent has a strong effect on the measured impedance spectrum. Minute changes in the amount of residual solvent over time under active evacuation causes considerable change in the impedance spectrum measured successively, and the results are consequently not very reproducible. A more dramatic change in conductance due to intentionally introduced acetonitrile solvent vapor is shown in Fig-2.3.

Annealing of the sample at elevated temperature under active vacuum seemed to reduce residual solvent to a point that successive impedance measurements done on the sample yield almost identical results, as exemplified by the excellent overlap of two sets of data in Fig-2.4 from the same sample. The annealing process was then used as a standard procedure to reduce variations due to residual solvent between samples.
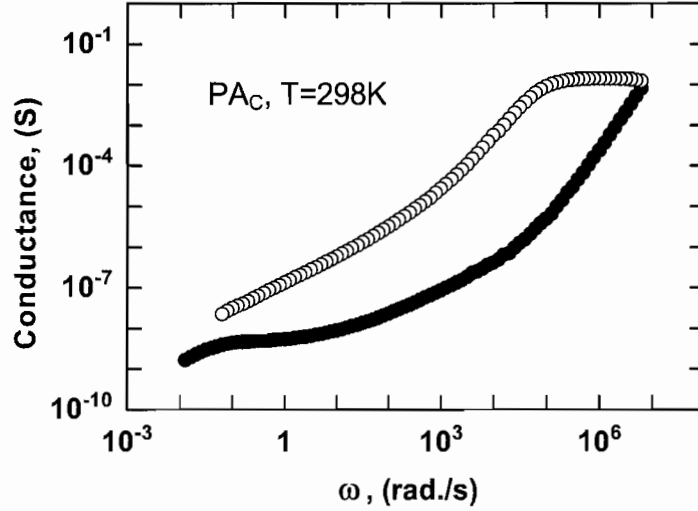
FIGURE 2.3: The change in conductance of a PA_C sample after exposing it to saturated acetonitrile vapor at room temperature. *solid circles*: under vacuum, *open circles*: after equilibrated with acetonitrile vapor. The experiment was done in an oxygen free environment.

2.3.2 Temperature dependence, thickness dependence, and general features of impedance data

In presenting the basic features of the experimental results, the PA_C samples are used as representative. Qualitatively similar results were observed for the PA_A samples. Fig-2.5 shows the results for a PA_C sample of thickness $L = 150$ nm at $T = 338$ K. To illustrate the various features of the response, the data are shown in terms of the complex permittivity $(\epsilon_{app}(\omega) = \epsilon'_{app}(\omega) - i\epsilon''_{app}(\omega))$, the real part of the conductivity $(\sigma'_{app}(\omega))$, and the loss tangent (Tan δ) in part A. The temperature dependence of $\epsilon'_{app}(\omega)$ is shown in part B. The subscript "app" is to emphasize that these are apparent quantities calculated directly from the experimentally measured impedance and phase angle of the entire sample cell.

Because of the relatively thin film geometry used, the onset of the experimental cell's RC relaxation was observed at the high frequency end of the dielectric spectrum. The RC time constant predicted from the cell geometry, ϵ' in the relevant frequency
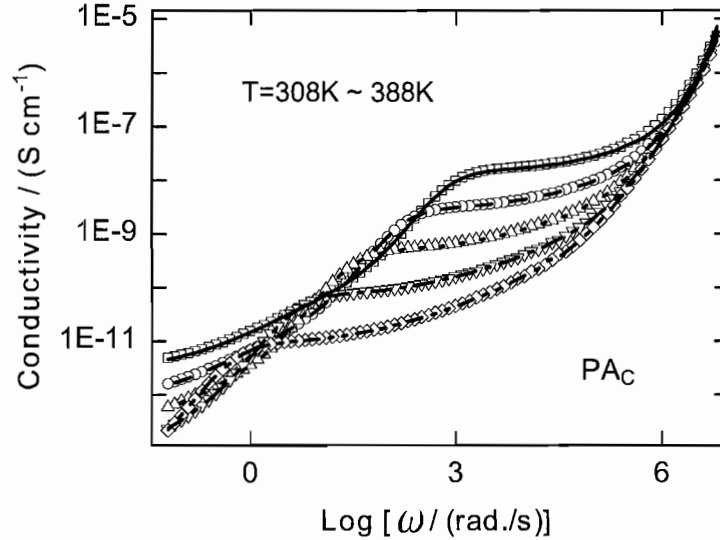
FIGURE 2.4: Two sets of temperature dependent conductivity data measured from the same PA$_C$ sample consecutively, after annealing. *open symbols*: fist set of measurement, *lines*: second set of measurement.

range, and lead resistance is $\sim 1 \times 10^{-7}$ s. This time constant is just outside the experimentally measured range of frequency and consistent with the onset of this process being visible. The assignment of the RC cell relaxation to the high frequency portion of the spectrum is also supported by the weak temperature dependence of $\epsilon'_{app}(\omega)$ observed in the high frequqency region (see Fig-2.5-b).

Aside from the RC relaxation of the experimental cell, there are two primary regimes of behavior observed: an electrode polarization process at low frequency and a dispersive ion transport regime at intermediate frequency. These two regimes are typical for measurements of glassy ionic conductors using blocking electrodes, and their assignment to physical processes at the outset is made for clarity. The validity of this assignment will be further supported throughout the remainder of this section.

The electrode polarization resulted in a peak in the dielectric loss at ω_{ep} and a corresponding sharp decrease in $\sigma'_{app}(\omega)$ as ω decreased below ω_{ep}. In this low frequency regime, the limiting slope in the log-log representation ($s \equiv d\log[\sigma'_{app}(\omega)/\sigma'_{app}(\omega_{ep})]/d\log(\omega/\omega_{ep})$) was not observed to be two as would be
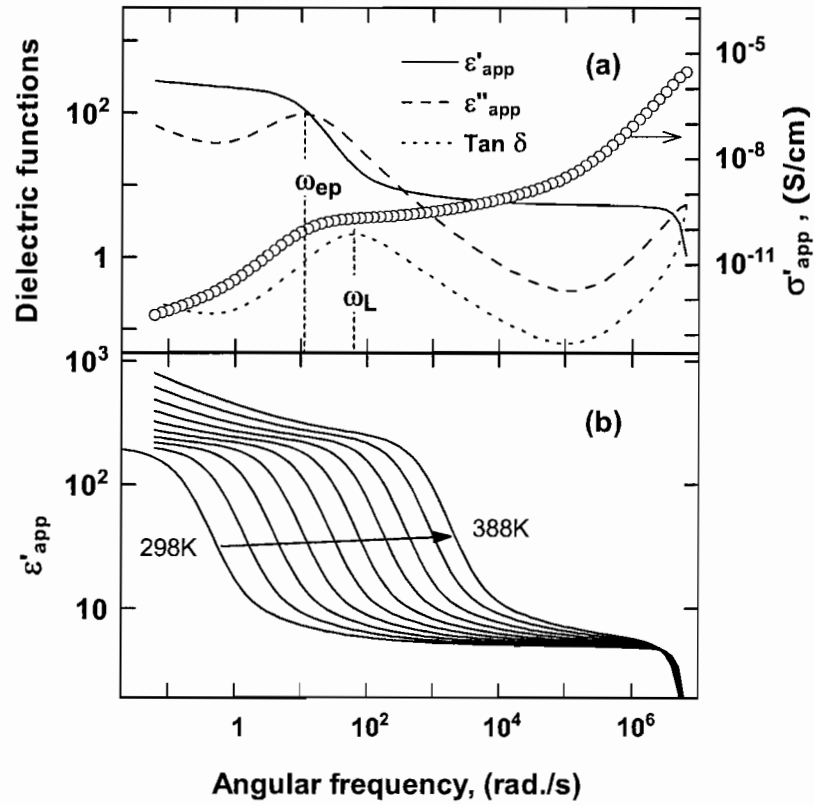
FIGURE 2.5: a: A representative set of impedance data collected from a 150 nm thick PA$_C$ sample at T=338K. The real part (solid line) and imaginary part (dashed line) of apparent relative permittivity, the real part of apparent conductivity (open circles, right ordinate), and the loss tangent (dotted line). b: the change of $\epsilon'_{app}(\omega)$ with temperature for the same sample.

predicted for a pure capacitance. Rather, s was frequency dependent with a maximum near $s = 1.5$. Correspondingly, the $\epsilon'_{app}(\omega)$ was not observed to plateau at low frequency, but to gradually rise with decreasing frequency. At frequencies just above ω_{ep}, a near plateau in the $\sigma'_{app}(\omega)$ was observed then giving way to a gradual increase in $\sigma'_{app}(\omega)$ with increasing frequency. At the highest frequencies, the limiting value of $s = 2$ was observed consistent with the ideal RC relaxation of the sample cell.

The thickness dependence of the dielectric response was measured to aid in assigning the various regimes of behavior. Fig-2.6 shows the frequency dependence of $\sigma'_{app}(\omega)$ and $\omega \partial \epsilon'_{app}/\partial \omega$ for PA$_C$ at two different thicknesses. The logarithmic derivative is shown to highlight changes in the slope of $\epsilon'_{app}(\omega)$. The derivative spectrum can also be viewed as a representation of the dielectric loss, obtained through the Kramers-Krönig relation, omitting purely dissipative transport processes that only contribute to $\epsilon''_{app}(\omega)$ but not to $\epsilon'_{app}(\omega)$.[38, 39] In Fig-2.6, the data are shown only up to the onset of the RC cell relaxation to focus on the ionic processes and provide a clearer picture of the dispersive transport regime than in Fig-2.5.

The responses from dispersive ion transport versus electrode polarization exhibited different thickness dependencies as expected for bulk versus interfacial processes. The peak in the derivative spectrum of $\epsilon'_{app}(\omega)$ (and in $\epsilon''_{app}(\omega)$) at ω_{ep} was observed to shift to lower frequency with increasing thickness. This is consistent with an electrode polarization process governed by a thickness-independent, double-layer charging capacitance and a resistance to ion transport that increases with film thickness. Both $\sigma'_{app}(\omega)$ and $\epsilon'_{app}(\omega)$ in the intermediate-frequency, dispersive-transport regime were observed to be independent of thickness. The thickness independent and gradually increasing $\sigma'_{app}(\omega)$ with $s < 1$ implies a bulk dispersive process with contributions from both long-range transport – as evidenced by the plateau in $\sigma'_{app}(\omega)$ – and polarization.[40, 41] The latter was also evidenced by the observation of a shoulder in the derivative spectrum of $\epsilon'_{app}(\omega)$ at frequencies above
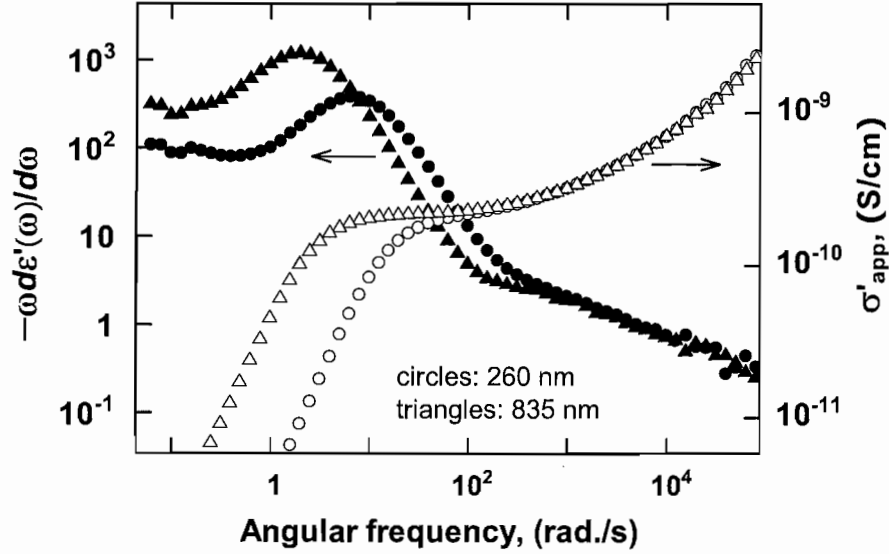
FIGURE 2.6: The logarithmic derivative of real relative permittivity (solid symbols, left ordinate) and apparent conductivity (open symbols, right ordinate) of two PA_C samples of different thickness at 338K

ω_L (see fig-2.6). The onset of this shoulder was observed to correspond with the dispersive rising in $\sigma'_{app}(\omega)$.

The dielectric data in the electrode polarization and dispersive transport regimes were observed to be strongly temperature dependent as shown for $\epsilon'_{app}(\omega)$ in fig-2.5. Normalizing the frequency axis by ω_{ep} to construct a master plot superimposed the $\epsilon'_{app}(\omega)$ and $\sigma'_{app}(\omega)$ spectra in the frequency range corresponding to dispersive transport and the onset of electrode polarization (see Fig-2.7). At frequencies substantially lower than ω_{ep}, the spectra were not observed to superimpose. Rather, the magnitude of the ϵ'_{app} in the low frequency regime was observed to increase with temperature.

2.3.3 DC ionic conductivity and activation energy

A key quantity of interest is the temperature dependence of the DC ionic conductivity. Ideally, the DC conductivity, σ_{DC} would be extracted from the low
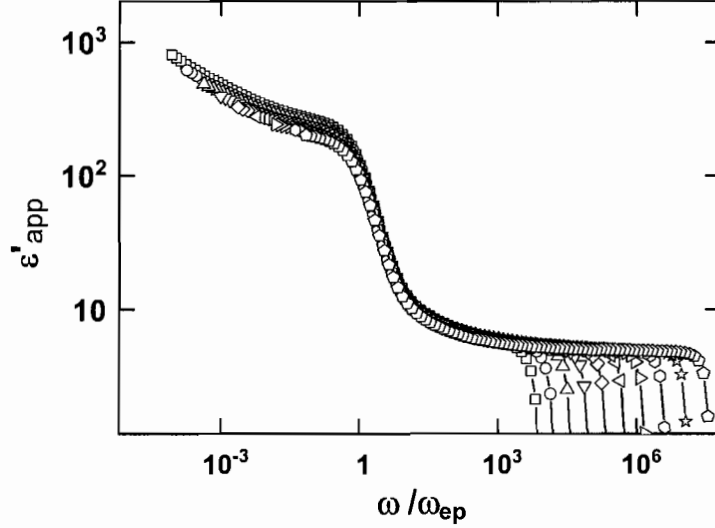
FIGURE 2.7: A master plot of real relative permittivity $\epsilon'_{app}(\omega/\omega_{ep})$ for a 150 nm thick PA_C sample within the temperature range from 298K to 388K in 10K increment.

frequency plateau of the AC conductivity. When blocking electrodes are employed, the extent of this low frequency plateau is limited by the onset of electrode polarization. In our system, s was observed to approach zero near the peak in the loss tangent ω_L, and consequently, the $\sigma'_{app}(\omega_L)$ was taken as an estimate of the DC conductivity. Although the validity of this approach relies on the extent to which $\sigma'_{app}(\omega)$ truly plateaus, it is a model-free estimate that can be applied in a straightforward and consistent manner to all of our data. This estimate is latter compared and found to be consistent with values obtained by modeling the full $\sigma_{app}(\omega)$ spectrum.

Fig-2.8 shows the temperature dependence of $\sigma'_{app}(\omega_L)$ for PA_A and PA_C samples of different thicknesses. As can be seen, there is little dependence on film thickness again consistent with the assignment of $\sigma'_{app}(\omega_L)$ to a bulk process. The $\sigma'_{app}(\omega_L)$ was observed to vary less than 15% over the four PA_C samples. The activation energies extracted from the temperature dependence of the $\sigma'_{app}(\omega_L)$ data are 0.94 eV for PA_C and 0.97 eV for PA_A.
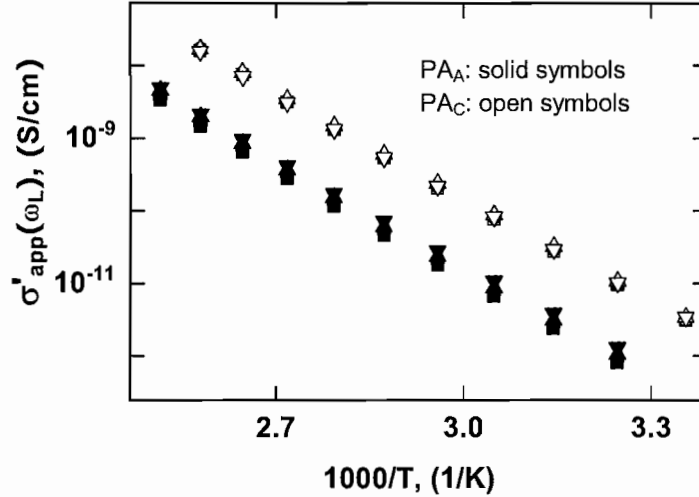
FIGURE 2.8: Arrhenius plot of the AC conductivity value at loss tangent peak frequency ω_L from four PA_A samples (solid symbols) and four PA_C samples (open symbols) of varying thickness.

To assist in assigning the type of charge carrier – electronic or ionic – samples swollen with acetonitrile vapor were also studied. Equilibration of films with acetonitrile vapor resulted in $\sigma'_{app}(\omega_L)$ increasing by six orders of magnitude (see Fig-2.3). A nonionic analogue to PA_C and PA_A with the ionic side chains replaced by a trimethylsilyl group (specifically, poly(trimethylsilylcyclooctatetraene)) was also studied at T = 338K, and it was observed to have a substantially lower $\sigma'_{app}(\omega_L)$ than either of the ion containing polymers at this temperature.

2.4 Equivalent Circuit Modeling

There have been a wide range of approaches to modeling the dielectric spectrum of dispersive ionic conductors. These typically involve a phenomenological model of ion transport incorporated into an equivalent circuit that also takes into account geometric and electrode polarization processes.[42] Such modeling can provide a more complete parameterization of the dielectric response and additional insights into its underlying physical basis.

2.4.1 Details about the modeling

Complex non-linear least-squares was used to fit $\sigma_{app}(\omega)$ for PA_A and PA_C to the equivalent circuit shown in Fig-2.9 using the LEVM program developed by Macdonald and coworkers.[42, 43] The circuit used contained a distributed resistive element (ρ_{KWW}) to model the bulk ionic processes within the ionomers. Taken in series with ρ_{KWW} was a pure capacitor (C_{dl}) to model interfacial double layer charging. It was found that fitting result could be improved by using a distributed model of double layer charging(see below). Both C_{dl} and ρ_{KWW} were taken in parallel with a second pure capacitance $C_p = \epsilon_D\epsilon_0 A/L$ to model the polarization response of the ion-free polymer matrix. The use of the pure parallel capacitance C_p assumes that there are no relaxations (e.g. dipolar) attributable to the polymer matrix throughout the frequency range modeled. The dielectric constant ϵ_D can be assigned to that describing the polarization response of the system in the absence of mobile charge carriers. For the glassy and conjugated polymers studied herein, this likely consists of mainly electronic polarization processes that persist up to frequencies beyond the upper limit of the measurement range.
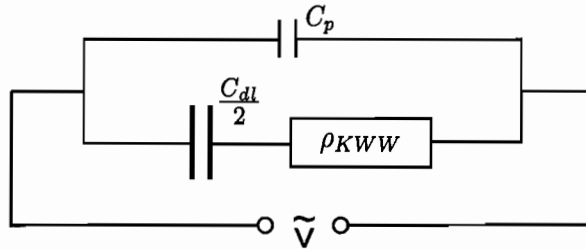
FIGURE 2.9: Equivalent circuit of the Au|Ionomer|Au structure.

The ρ_{KWW} used is that originally described by Macedo et $al.$[44] and is often referred to as the modulus formalism; this approach is based on a modulus level description and a Kohlrausch-Williams-Watts (KWW)[45] stretched exponential decay of the electric field under the constraint of constant displacement. The KWW

decay function $\phi(t)$ is characterized by a characteristic time τ_{KWW} and exponent β:

$$\phi(t) = \exp\left[-\left(\frac{t}{\tau_{KWW}}\right)^{\beta}\right] \tag{2.1}$$

When cast in terms of $\rho(\omega) = 1/\sigma(\omega)$, the ρ is given by:

$$\rho(\omega) = \frac{\rho_0 - \rho_\infty}{i\omega\langle\tau\rangle}[1 - I(\omega)] + \rho_\infty \tag{2.2}$$

where $\rho_0 \equiv \sigma_0^{-1} \equiv \rho(\omega = 0) = \rho'(\omega = 0)$, $\rho_\infty \equiv \rho(\omega = \infty) = \rho'(\omega = \infty)$, and $I(\omega)$ is the response function:

$$I(\omega) = \int_0^\infty \frac{g(\tau)}{1 + i\omega\tau}d\tau = \int_{0-}^\infty -\frac{d\phi(t)}{dt}\exp(-i\omega t)dt \tag{2.3}$$

The $g(\tau)$ is the distribution of relaxation times τ describing the KWW electric field decay at constant displacement. The average of this distribution, $\langle\tau\rangle$, is given by:

$$\langle\tau\rangle = \int_0^\infty \frac{\tau g(\tau)}{1 + i\omega\tau}d\tau = \tau_{KWW}\frac{\Gamma[\beta^{-1}]}{\beta} \tag{2.4}$$

where Γ is the gamma function. The related distribution defined by $\tau g(\tau)$ has also been interpreted in terms of a distribution of resistivity relaxation times arising, for instance, from a distribution of activation energies for carrier transport.[46] The approach above has been used to model a variety of ionically conducting glasses, and it can be related to the microscopic hopping model of Scher and Lax[47] with $\langle\tau\rangle$ being identified as the mean waiting time.[48]

The ρ_{KWW} used herein is provided within the LEVM program as the "KWW1" distributed element. The complete set of parameters for the equivalent circuit model are $\langle\tau\rangle$, β, ρ_0, ρ_∞, C_{dl}, and ϵ_D. Typically and herein, ρ_∞ is assumed zero because the experimental frequency range does not extend sufficiently high for the resistivity to approach this limit. A cutoff of τ is set at $\ln(\tau_{min}/\tau_{KWW}) = -6.7$.

The $\sigma(\omega)$ data were first fit with a freely varying β. The value of β in this approach was found to vary somewhat with temperature, but it was typically found to be near $\beta = 1/3$ as is typical for glassy ionic conductors.[41, 49] Consequently, β

was fixed at a value of 1/3 for all of the fits. This not only reduced the number of fitting parameters to a total of four ($\langle \tau \rangle$, ρ_0, C_{dl}, ϵ_D), but it also made possible the use of exact rather than numerical approximations in the evaluation of $I(\omega)$ within the LEVM program.
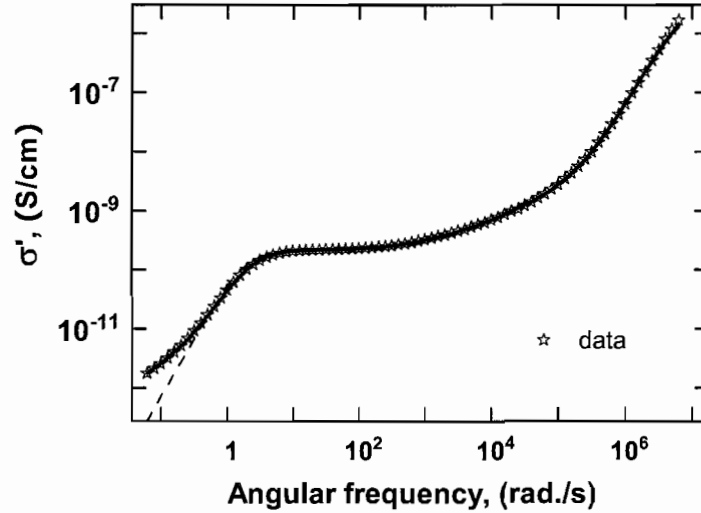
FIGURE 2.10: A comparison of LEVM fitting results for a 835nm thick PA$_C$ sample at T=338K. KWW1 response with $\beta = 1/3$ and cutoff at $\ln(\tau_{min}/\tau_{KWW}) = -6.7$ was chosen to represent ρ_{KWW} in the equivalent circuit. Solid line: C_{dl} treated as a distributed element. Dash line: C_{dl} treated as an ideal capacitor.

2.4.2 Modeling results

The results of two fitting approaches are compared in Fig-2.10 for a typical set of experimental data. The dashed line in Fig-2.10 was obtained by using an ideal capacitor to account for ionic double layer charging. The near room temperature values of C_{dl} were 3.5×10^{-6} Fcm^{-2} and 2.5×10^{-6} Fcm^{-2} for PA$_A$ and PA$_C$, respectively. It can be seen that the very low frequency data were not well modeled by a simple ideal capacitor. A better fit over the entire frequency range was achieved by using a distributed circuit element to model the double layer charging as shown by the solid line in Fig-2.10. The use of a distributed element, however, does require

additional parameters beyond those mentioned above. The differences in the resulting ρ_0 and $\langle \tau \rangle$ between the two fitting approaches are 5% and 15%, respectively. Hence, for these parameters of interest, the choice of a pure capacitance versus a distributed capacitance results in only a small difference. The values of σ_0 obtained from the distributed capacitance approach are compared with $\sigma'_{app}(\omega_L)$ in Fig-2.11. The two estimating methods yield essentially the same result. The best-fit values of ϵ_D were found to be 4.2 for PA$_A$ and 4.5 for PA$_C$ near room temperature (T=308K).
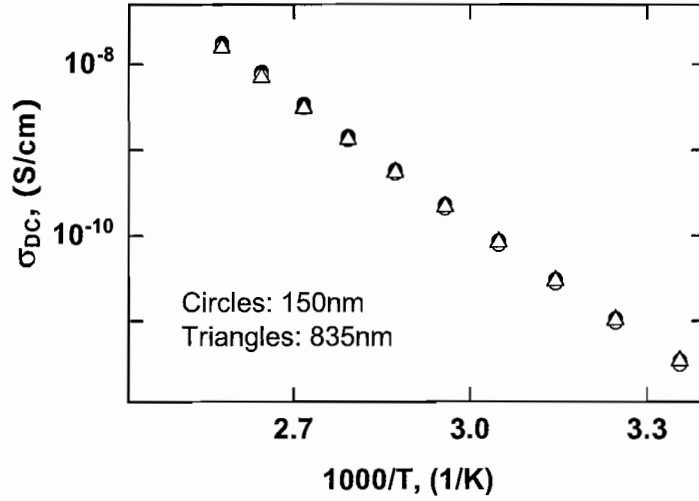
FIGURE 2.11: DC conductivity values of two PA$_C$ samples, estimated through different methods. Open symbols are the AC conductivity values at loss tangent peak frequency ω_L, solid symbols are results from Complex Nonlinear Least Square fitting.

The temperature dependance of ion hopping rate $\omega_h = \langle \tau \rangle^{-1}$ for four different samples of both PA$_A$ and PA$_C$ are shown in Fig-2.12. The ω_h are independent of the sample thickness, and the average activation energies obtained through the temperature dependance of ω_h are identical to that obtained through the temperature dependance of $\sigma'_{app}(\omega_L)$.
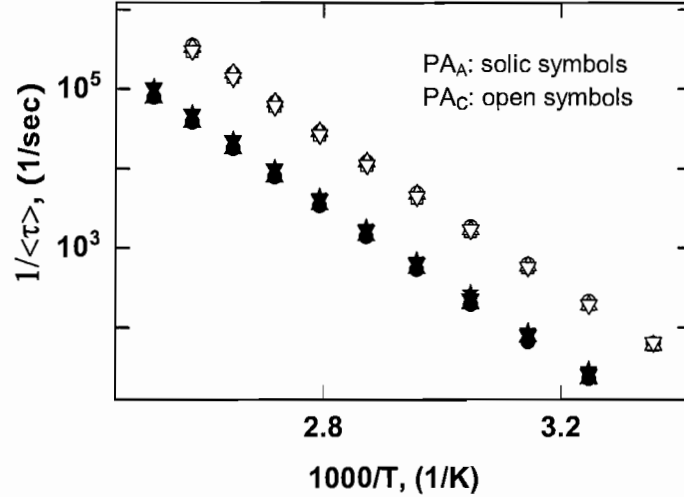
FIGURE 2.12: The temperature dependence of ion hopping rate $\omega_h = \langle\tau\rangle^{-1}$ for four PA_A (solid symbols) and four PA_C (open symbols) samples of different thickness.

2.4.3 Discussion

The observed frequency and temperature dependencies of σ_{app} for PA_A and PA_C are more similar to that observed in ionically conducting inorganic glasses than in conventional polymer electrolytes. This is as expected because the latter are typically polymer-salt complexes characterized above their glass transition temperatures[28, 29, 30, 39] whereas PA_A and PA_C are both in their glassy state over the entire temperature range studied. The σ_{DC} for both the PA_A and PA_C ionomers is strongly activated with T = 308K values (1.1×10^{-11} S/cm and 1.3×10^{-12} S/cm, respectively) that are low relative to high performance solid electrolytes. [28, 29, 30, 31] Although the temperature range of the measurements was only 90K, the strongly activated transport still provided over three orders of magnitude change in σ_{DC} to establish Arrhenius behavior. The Arrhenius temperature dependence is comparable to that observed in glassy and crystalline solid-state ionic conductors.[50, 27] It differs from classic polymer electrolytes where

Vogel-Tamman-Fulcher behavior is typically observed because of the importance of polymer segmental motion above the glass transition temperature.[28]

The observed activation energies describing $\sigma_{DC}(T)$ for the ions in PA_A and PA_C were very similar, and they are on the high end of that observed in inorganic glasses. For instance, the widely studied sodium silicate glasses have activation energies for the transport of Na^+ in the range of 0.5-1.0 eV depending on network modifier. The relatively large activation energies for the transport of the organic ions Me_4N^+ and $CF_3SO_3^-$ is not surprising given their size. Molecular modeling reveals that the ion sizes are r~1.9Å for the $CF_3SO_3^-$ anion in PA_C and r~2.2Å for Me_4N^+ cations in PA_A. These ions are much larger than the typical alkali metal ions studied in solid-state ionic conductors. Within a classical model such as that of Anderson and Stuart, the large activation energy for transport is correlated with the need to open a relatively large "doorway" within the matrix for the ion to pass through in addition to any electrostatic energy terms.[51]

The activation energy for ionic conductivity has important consequences for applications of conjugated ionomers. First, it plays a central role in determining the room temperature ionic conductivity, which determines the time response for any devices that relies on the redistribution of ions within the material. The relatively large activation energies for PA_A and PA_C imply that devices based on their mixed ionic/electronic character will have relatively slow response times. Second, it determines the extent to which ions can be redistributed at one temperature and then frozen in at a second temperature. There have been a number of studies on so-called frozen junctions based on mixed ionic/electronic conducting polymers.[15, 16] In these junctions, an applied bias is used to redistribute ions within the active material at an elevated temperature and this new structure is then frozen in place by quenching the sample to low temperature, thereby freezing in the ion distribution established with the applied bias. The extent to which this approach is successful is intimately coupled to the activation energy for ion motion. A large activation energy

is beneficial when a large contrast in the time scale for ion motion at high vs. low temperature is desired.

Ionic conductivity in solid-state crystalline and glassy conductors is usually described in terms of the hopping of charge carriers in a random walk, in which case the DC conductivity is given by:[52]

$$\sigma_{DC} = \frac{ge^2a^2}{k_BT}N\omega_h \tag{2.5}$$

where ω_h is the mean hopping rate, g is a geometrical factor that is set to 1/6 for a 3D hopping network, N is the the concentration of mobile ions, and a is the mean hopping distance. In many applications of Eq.2.5 , both N and ω_h have been considered temperature dependent. The dependence of N on temperature arises from considering two populations of ions: one mobile and the other not.[53, 50, 32] This leads to the activation energy for σ_{DC} being a composite of the activation energy for ion hopping and the enthalpy for free carrier formation. The extent to which this is true can be probed if separate measures of both the ω_h and σ_{DC} are available. The distributed nature of the ionic transport was well modeled by the modulus formalism. As mentioned above, the modulus formalism can be interpreted in terms of the microscopic continuous time random walk model of Scher and Lax[47] with $\langle\tau\rangle$ the mean waiting time for a hop. Hence, the analysis of $\sigma_{app}(\omega)$ within the modulus formalism yields measures of both σ_{DC} and ω_h in Eq.2.5.

The activation energies for $\langle\tau\rangle^{-1}$ and σ_0 were found to be identical within experimental error. This close parallel argues for a single type of mobile ions, albeit one described by a distribution of hopping times. This is perhaps not surprising given the high ion density and amorphous nature of PA_A and PA_C. In such disordered materials, it is difficult to draw a clean distinction between a mobile and immobile ion population.

The similarity of the activation energy for $\langle\tau\rangle^{-1}$ and σ_0 implies that the quantity N is the stoichiometric ion density, which is $\sim 2.1 \times 10^{21} \text{cm}^{-3}$ for PA_A and $\sim 1.8 \times 10^{21} \text{cm}^{-3}$ for PA_C. Hence it is possible to estimate the quantity a within Eq.2.5

leading to the value of $a = 0.5\text{Å}$ and $a = 0.6\text{Å}$ for PA_A and PA_C, respectively. For comparison, the average distances between ions in PA_A and PA_C are $\sim 7.8\text{Å}$ and $\sim 8.2\text{Å}$, respectively. The small value of a calculated is consistent with the idea that only relatively small displacements are possible because of the substantial dilation or rearrangement of the polymer required for ion motion. The small a could also be interpreted in terms of hops of longer distance but on a nearly filled lattice. In this case, the N term in Eq. 2.5 is replaced by $c(1 - c)N_s$ where c is the fraction of N_s equivalent lattice sites per unit volume that are occupied by a mobile ion ($N = cN_s$). A larger value of a would be calculated for c approaching one. The extreme case of hops on the order of the ion to ion distance would correspond to c = 0.996.

The ionic transport processes discussed above dominated the intermediate frequency regime of the observed dielectric spectrum, but the low and high frequency extremes can also yield important parameters describing the ionomers, namely, C_{dl} and ϵ_D. Typically ϵ_D is extracted from the high frequency side of the dielectric spectrum. The onset of the RC sample cell relaxation and the likelihood that ionic polarization processes still contribute to the measured $\epsilon'_{app}(\omega)$ in this region, however, complicates such direct extraction. Consequently, ϵ_D was extracted from equivalent circuit modeling. The room temperature values of ϵ_D were found to be 4.2 and 4.5 for PA_A and PA_C, respectively. In comparison, the high frequency values of ϵ'_{app} just before the RC cell relaxation, ϵ'_{hf}, were found to be 4.6 and 5.0, respectively. The difference between ϵ_D and ϵ'_{hf} can be explained by the presence of some small remaining contribution from ionic polarization as required by the form of ρ_{KWW} with $\rho_\infty \equiv 0$. The ϵ_D values are slightly lower than that reported for non-functionalized polyacetylene [54, 55].

The double layer charging processes as would be most simply described by a pure capacitance C_{dl} are not so clear. Characterizing the double layer charging process in the single-layer ionomer structures herein is important to understanding the electrostatic potential drops in more complex multilayer systems.[19] The low

frequency polarization, however, is not well described by a pure double-layer charging capacitance. It is observed in Fig-2.5 that the value of ϵ'_{app} keeps increasing slowly as the frequency decreases. This dispersive feature at low frequency has also been observed in other ion-conducting systems with blocking electrodes,[56, 57, 58, 59, 60] and it has been attributed to factors such as electrode surface morphology,[58, 60] image charge effect,[59] and charge injection at the electrode surface.[57, 60] In our system, it is also possible that the ions covalently bound to the polymer backbone are not completely immobile thereby contributing to the low frequency polarization, and likely increasingly so at elevated temperature.

Up until know, we have assumed that the DC conductivity measured is an ionic conductivity. As polyacetylene is an organic semiconductor, electronic conductivity can also contribute to the observed response. Several observations, however, argue against the observed conductivity response being due to electronic as opposed to ionic charge carriers. The first is that the activation energy for transport is large consistent with the motion of the massive ions. Separate studies on PA_A and PA_C into which electronic charges have been intentionally injected at higher applied biases show a much lower activation energy for carrier transport. The second is that the σ_{DC} is observed to increase substantially upon solvent swelling. Such an increase is consistent with an increase in free volume and softening of the polymer matrix lowering the activation energy for ion transport. Such swelling would be expected to disrupt the chain-to-chain transfer of electronic charges needed for the three dimensional transport of electronic carriers. Finally, measurements on a non-ionically functionalized poly(trimethylsilylcyclooctatetraene) analogue fabricated in the same way shows substantially lower $\sigma'_{app}(\omega_L)$ at 335K.

It is perhaps surprising that there is such a small contribution from electronic conductivity given the semiconducting nature of polyacetylene. The band gaps of PA_A and PA_C are in the vicinity of 1.4 eV so if the material was truly intrinsic the carrier density would be very low. The conductivity of near intrinsic materials,

however, is often determined by their defect concentration, and polyacetylene is no different. For instance, values for nominally undoped polyacetylene have ranged from 10^{-8} S/cm or less to 10^{-5} S/cm depending on the method of synthesis.[1, 55, 61]. The assignment of $\sigma'_{app}(\omega_L)$ to ionic conductivity implies that the intrinsic electronic conductivities of PA_A and PA_C are less than $10^{-11} - 10^{-12}$ S/cm near room temperature.

2.5 Analysis through electrode polarization

The analysis in previous section through equivalent circuit modeling primarily focused on the response in a frequency range that is not substantially affected by electrode polarization of the mobile ions. The modeling made it possible to estimate the DC ionic conductivity σ_{DC} and the dispersive hopping rate ω_h of ion conduction, as well as the high frequency limiting dielectric constant ϵ_D of the two ionomers. The value of interfacial capacitance C_{dl} was also obtained through fitting, and the effective mobile density n_{eff} can in principle be estimated from the magnitude of C_{dl} using a ionic double layer model.

Alternatively, data in the frequency range corresponding to electrode polarization (EP) process can also be modeled to extract the value of σ_{DC}, C_{dl}, and n_{eff}.

2.5.1 Theory of electrode polarization

In a system consisting of an ionic conductor sandwiched between blocking or partially blocking electrodes, electrode polarization (space charge polarization) occurs when mobile ions driven by low frequency electric field build up at each electrode surface. The modern theoretical treatment of EP was first developed by Chang and Jaffé[62] and later generalized and expanded by Macdonald[63, 57] and others[64, 65]. In this section, we will use the simplified model for systems with only one sign of mobile charge carriers proposed by Beaumont and Jacobs[65] to further analyze

our experimental data, based on the similarities between this model and our actual system. The electronic conductivity in our system can be accounted for, if necessary, by introducing a discharging parameter to the electrodes involved.

According to Beaumont and Jacobs[65], the apparent (measured) complex admittance per unit area of the system can be expressed as:

$$
\begin{aligned}
Y_{app}^* &= \frac{\sigma_0}{L} + i\omega\frac{\epsilon_\infty\epsilon_0}{L} + G_P + i\omega C_P \\
&= (G_0 + i\omega C_0) + (G_P + i\omega C_P)
\end{aligned}
\tag{2.6}
$$

where L is the separation between the two electrodes, σ_0 is the bulk conductivity of the system in the absence of electrode polarization, ϵ_∞ is the relative permittivity of the material in the absence of mobile charge carriers, ϵ_0 is the permittivity of vacuum, G_P and C_P are the per unit area conductance and capacitance contribution from electrode polarization of the mobile charge carriers. Assuming complete dissociation and neglecting recombination, the contribution from EP can be approximated by:

$$
G_P = \left(\frac{-2}{2+\rho}\right)\frac{1}{1+\omega^2\tau_{ep}^2}G_0 = \frac{\gamma}{1+\omega^2\tau_{ep}^2}G_0
\tag{2.7}
$$

$$
C_P = \left(\frac{2}{2+\rho}\right)^2\frac{M}{1+\omega^2\tau_{ep}^2}C_0 = \frac{\gamma^2 M}{1+\omega^2\tau_{ep}^2}C_0
\tag{2.8}
$$

where the characteristic relaxation time τ_{ep} of electrode polarization is determined by

$$
\tau_{ep} = \frac{1}{\omega_{ep}} = \gamma M\frac{\epsilon_0\epsilon_\infty}{\sigma_0}
\tag{2.9}
$$

and ρ is the discharging parameter of the two symmetric electrodes. The case when electrodes are completely blocking corresponds to $\rho = 0$, while $\rho = \infty$ represents an "Ohmic" contact. For convenience, one can also define $\gamma = 2/(2+\rho)$ as the blocking factor of the electrode. The bulk-to-interface ratio M is defined as $M = L/(2L_D)$, where L_D is the Debye length

$$
L_D = \sqrt{\frac{\epsilon_0\epsilon_\infty k_B T}{n_0 e^2}} = \frac{L}{2M}
\tag{2.10}
$$

with k_B the Boltzmann constant, T the absolute temperature, n_0 the mobile charge carrier density, and e the charge of a proton.

In an actual experiment, the response of the whole system is measured, and the apparent conductance as well as capacitance per unit area can be expressed as:

$$G_{app} = \frac{\sigma_{app}}{L} = \left(1 - \frac{\gamma}{1 + \omega^2\tau_{ep}^2}\right) G_0 \tag{2.11}$$

$$C_{app} = \frac{\epsilon_{app}}{L} = \left(1 + \frac{\gamma^2 M}{1 + \omega^2\tau_{ep}^2}\right) C_0 \tag{2.12}$$

It can be shown that the loss tangent ($\tan\delta = G_{app}/\omega C_{app}$) of the system has a peak at

$$\omega_L = \omega_{ep}\sqrt{\frac{1}{2}\left[A + \sqrt{A^2 - 4(1-\gamma)(1+\gamma^2 M)}\right]} \tag{2.13}$$

$$A = (\gamma^2 M + 3\gamma - 2)$$

given that $A^2 - 4(1-\gamma)(1+\gamma^2 M) \geq 0$.

In the case of $M \gg 1$ and $\gamma \approx 1$, the loss tangent peak frequency can be well approximated by

$$\omega_L = \gamma\sqrt{M}\, \omega_{ep} \tag{2.14}$$

Based on this EP model, the set of basic parameters that one needs for analyzing experimental data are: γ, ω_L, ω_{ep}, L, and ϵ_∞. In our analysis, ω_L and ω_{ep} (see Fig-2.5) were obtained by fitting the peaks in $\tan\delta(\omega)$ and $\epsilon_{app}''(\omega)$, ϵ_∞ was approximated by the high frequency limiting value ϵ_{hf} right before the onset of RC relaxation, and the sample thickness L was approximated with its measured value at room temperature, assuming negligible change within the temperature range. The value of γ can be estimated from $\sigma_{app}(\omega)$ through Eq. (2.11) by comparing the low frequency limiting value of σ_{app} to its value at the high frequency plateau. It was found that the value of γ for PA$_C$ can be well approximated by 1 within the temperature range, while the value of γ for PA$_A$ various from 0.92 at 348K to 0.97 at 398K.

Once the set of basic parameters are determined, the bulk conductivity σ_0 due to mobile charges can be calculated through Eq. (2.9), and mobile charge concentration n_0 can be calculated through Eq. (2.10).

2.5.2 High frequency limiting relative permittivity

The values of high frequency limiting dielectric constant ϵ_{hf} estimated from ϵ'_{app} spectrum are plotted in Fig-2.13 as a function of temperature. These values were taken at a frequency right before the onset of RC relaxation, typically at $\omega = 10^4 \omega_{ep}$. It is found that ϵ_{hf} of both ionomers increase slowly with the increase of temperature.
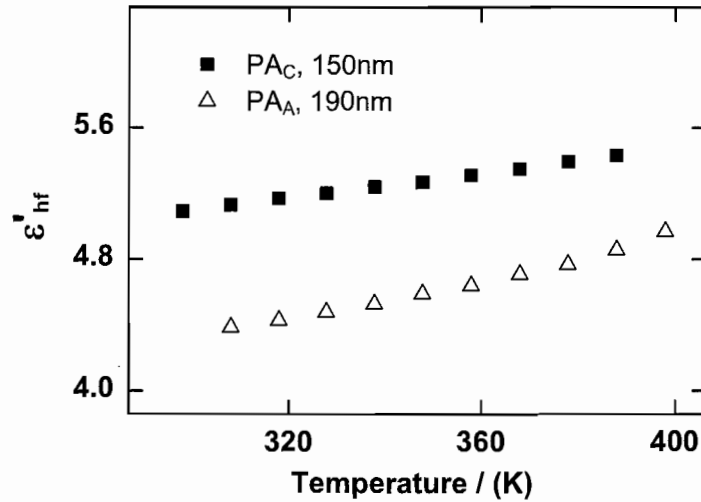
FIGURE 2.13: The high frequency limiting dielectric constant of a PA_C (solid squares) and PA_A (open triangles) as a function of temperature.

2.5.3 DC ionic conductivity

The value of σ_0 at different temperatures calculated based on the EP model are shown in Fig-2.14 together with the result obtained through the alternative methods described in Section-2.3.3. In general the two sets of results agree rather well with

each other, although one will notice that the calculated σ_0 is slightly lower than $\sigma_{app}(\omega_L)$. This small discrepancy is insignificant compared to the orders-of-magnitude variation throughout the temperature range.
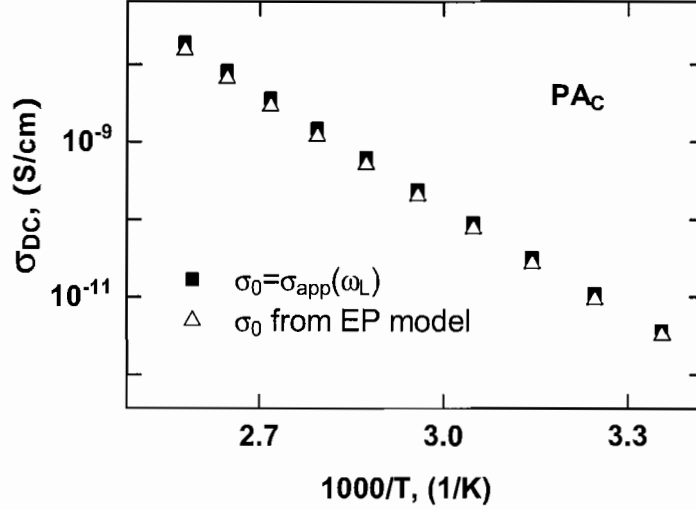
FIGURE 2.14: DC conductivity values of a 260nm thick PA_C sample estimated through different methods. Solid squares: the AC conductivity values at loss tangent peak frequency ω_L; open triangles: results obtained through electrode polarization modeling.

The good agreement among the σ_0 values obtained through different methods in Fig-2.14 and Fig-2.11 again demonstrates that the simple method of using $\sigma_{app}(\omega_L)$ as an estimate of σ_0 is indeed viable.

2.5.4 Debye length and effective mobile ion density

One important quantity of interest is the Debye length of each ionomer due to mobile ions, upon which the ionic double layer capacitance and effective mobile ion density can be estimated.

The temperature dependent Debye lengths estimated through Eq. (2.10) and Eq. (2.14) are shown in Fig-2.15 for both PA_A and PA_C. Note that the estimate of M according to Eq. (2.14) relies on the identification of both ω_{ep} and ω_L. Due

to the dispersion of the ϵ''_{app} spectrum at low frequency (see Fig-2.5), the values of ω_{ep} at temperatures lower than 338K for PA_A become hard to determine, hence only values at higher temperatures are shown in Fig-2.15.
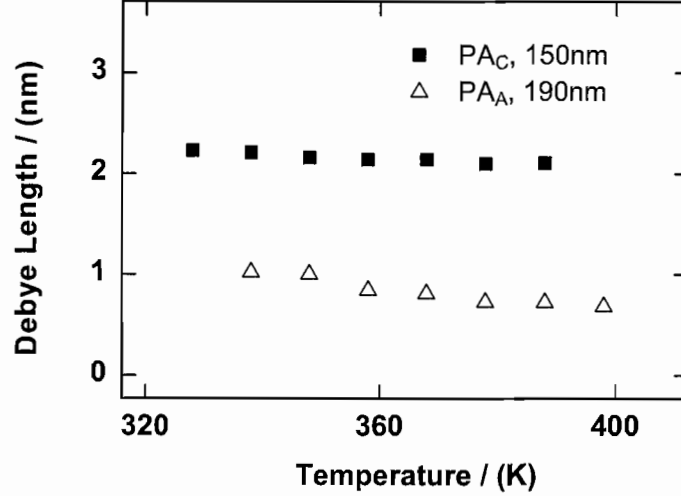
FIGURE 2.15: The estimated Debye length of a PA_C sample (solid squares) and a PA_A sample (open triangles) as a function of temperature.

As can be seen from Fig-2.15, the Debye length decreases slightly with the increase of temperature for both PA_A and PA_C, with that of the PA_A changing faster. As expected, the Debye length thus calculated does not change substantially with sample thickness, as evidenced by the result in Fig-2.16 of several PA_C samples of different thickness at 378K.

Now that the Debye length is known, with the additional knowledge of ϵ_{hf} one can easily calculate the equivalent interfacial capacitance C_{dl}, and effective mobile ion density n_{eff} via Eq. (2.10). The C_{dl} thus calculated is $\sim 4.5 \times 10^{-6}$ Fcm^{-2} for PA_A and $\sim 2.3 \times 10^{-6}$ Fcm^{-2} for PA_C, at T=358K. These capacitance values are comparable to the results obtained from equivalent circuit modeling in the previous section.

Fig-2.17 shows the effective mobile ion density n_{eff} at different temperatures obtained through Eq. 2.10 for one PA_A and one PA_C sample. One could notice
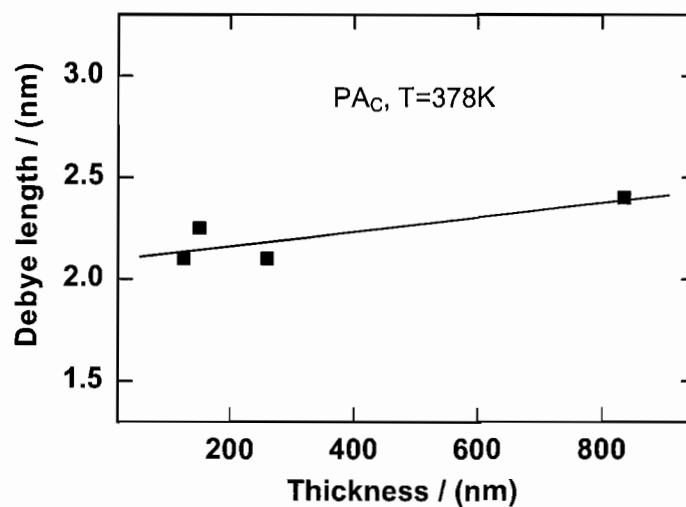
FIGURE 2.16: Debye length of several PA_C samples of various thickness at 378K. The linear fit is added to guide the eye.
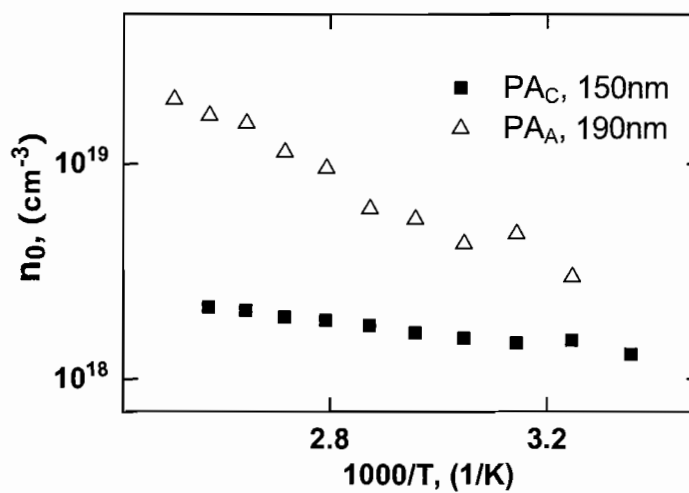
FIGURE 2.17: The effective mobile ion density of PA_A (filled triangles) and PA_C (open triangles) as a function of temperature.

that the effective ion density of PA_A changes more rapidly with temperature than that of PA_C. A linear fit of data points in Fig-2.17 gives an activation energy of $E_a \simeq 0.08$ eV for PA_C and $E_a \simeq 0.22$ eV for PA_A. It is worth pointing out that the use of Eq. (2.10) will likely result in an underestimate of the true effective mobile ion density due to the implicit assumption that ions can be treated as point charges, while in reality there could be a limit to how close the ions can approach the electrode surface as well as a limit to the packing density of the ions.

2.5.5 Discussion

The analysis in section 2.5 is largely independent of the equivalent circuit modeling in the previous section, therefore a comparison of results obtained from these two separate methods gives us an additional measure of confidence on each method.

The high frequency limiting dielectric constant values ϵ_{hf} estimated in this section are typically 10% higher than the ϵ_D values obtained through equivalent circuit fitting. The higher values of ϵ_{hf} can be explained by the existence of an additional contribution from mobile ions that persist well into higher frequencies than where ϵ_{hf} was determined, while ϵ_D represent only the dielectric constant of the mobile ion free polymer matrix.

Due to the fact that EP modeling deals with mostly the low frequency data where the Debye length plays a dominant part in the impedance response of the device, the value of C_{dl} estimated in this section should be treated with greater confidence than the results obtained through equivalent circuit modeling. Although some uncertainty arises from whether the value of ϵ_{hf} or ϵ_D should be used in Eq. (2.10), the difference between the values of C_{dl} estimated through EP modeling and equivalent circuit modeling is within a factor of two. Both results showed that the anionic ionomer PA_A has a higher interfacial capacitance, although its ionic conductivity is lower than that of PA_C. It is worth pointing out that both estimates of C_{dl} in this section and the previous section are not reflecting the true value of the capacitance at the lowest

frequency, which could have a complex origin and could be many times higher than 3×10^{-6} Fcm^{-2} as evidenced by Fig-2.7.

Within the temperature range of experiment, the effective mobile ion density of both ionomers fall into the range between 1×10^{18} cm^{-3} and 2×10^{19} cm^{-3}, which represents less than 1% of the stoichiometric ion density of $\sim 2 \times 10^{21}$ cm^{-3}. These ion density values represent only a lower limit of the true effective mobile ion density. The use of a more accurate double layer model which takes into account the finite volume of mobile ions will result in higher effective mobile ions densities. This result also argues against the possibility that electronic charges carriers are responsible for the observed relaxation process since such a concentration far exceeds the realistic value of an intrinsic semiconductor with a band gap of $E_G \simeq 1.4$ eV. Meanwhile, the coexistence of ionic and electronic charge carriers will likely result in more complex impedance response than what was observed, due to the expected difference in both carrier mobility and their temperature dependance.

To the extent that Eq. (2.10) represents a valid description of the ionic double layer in reality, the low effective mobile ion density estimated through the express of Debye length according to Eq. (2.10) is seemingly in contradiction with the results obtained through equivalent circuit modeling in the previous section, which suggest that ions in both ionomers are fully dissociated. However, the apparent contradiction can be resolve if ions are indeed moving in a crowded environment through hopping, where the DC ionic conductivity can be expressed by a modified version of Eqn. (2.5):

$$\sigma_{DC} = \frac{ge^2a^2}{k_BT}\omega_h N_s(1-c)c \tag{2.15}$$

where c is the fraction of N_s equivalent lattice sites per unit volume that are occupied by a mobile ion ($N = cN_s$). As c approaches 1, the effective mobile ion density $N_s(1-c)c$ is reduced to $N_s(1-c)$ which is only a small fraction of the true mobile ion density $N = cN_s$. One situation where Eq. (2.10) could be inadequate is when mobile ions cannot move closer to the electrode surface than a certain distance, say 5Å. In such case the effective ion density would be underestimated.

2.6 Results from Au|PA$_A$|PA$_C$|Au samples

After the ion transport in single-layer ionomers are characterized, a comparison of their results with the result from bi-layer junction could be informative. As mentioned in Chapter-I, a key question regarding the bi-layer junction is how does it's capacitance spectrum differ from the single-layers? Since we have learned that the interfacial capacitance of both single-layer ionomers are comparable and does not change significantly with thickness, the capacitance spectrum will tell us whether the PA$_A$|PA$_C$ interface plays a role in the overall response of the device.
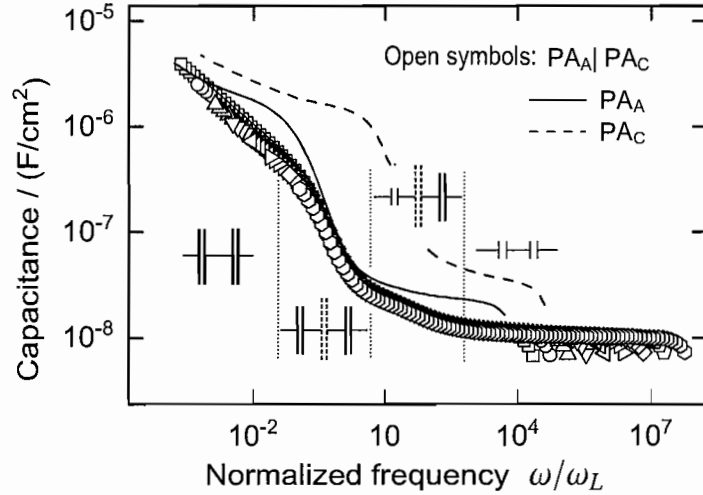
FIGURE 2.18: The capacitance spectra of a 220|200 nm bi-layer sample from 308K to 388K (open symbols), a 190nm single-layer PA$_A$ sample at 388K (solid line), and a 150nm single-layer PA$_C$ sample at 388K (dash line). The frequency axis was normalized to the ω_L of PA$_A$ sample at corresponding thickness. The simplified equivalent circuits illustrate the transitions between different polarization processes as the frequency changes.

For the convenience of comparison, the capacitance spectrum all three sample structures, Au|PA$_A$|Au, Au|PA$_C$|Au, and Au|PA$_A$|PA$_C$|Au, are shown in Fig-2.18. Note that the frequency axis was normalized by the ω_L of PA$_A$ sample at equivalent thickness, so that the difference in onset frequency of electrode polarization between PA$_A$ and PA$_C$ is correctly reflected.

The spectrum in Fig-2.18 can be separated into four regions, the low frequency region (LF) up to the left vertical line, the PA_A electrode polarization region (EP-A) between the left vertical line and the center vertical line, the PA_C electrode polarization region (EP-C) between the center vertical line and the right vertical line, and the high frequency region (HF) beyond the right vertical line. In the HF region the bi-layer sample behaves much like a single-layer sample with similar thickness. Since no space charge polarization of ions occurs, the capacitance value is reflective of the geometric capacitance.
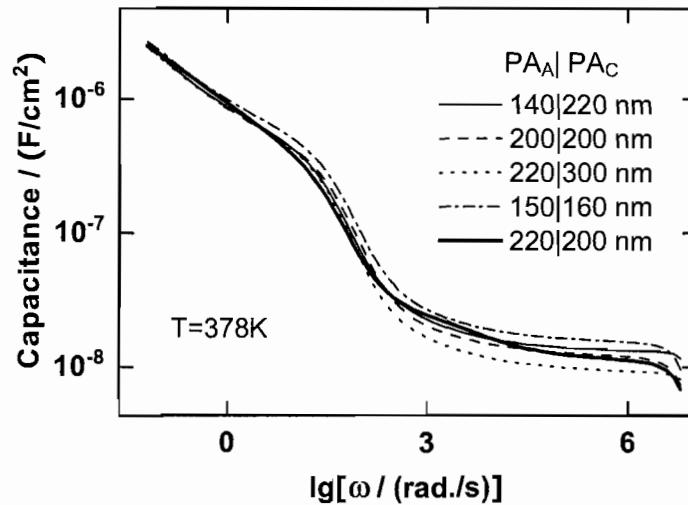
FIGURE 2.19: The capacitance spectra of five bi-layer samples of different thickness at T=378K.

When we lower the frequency to the EP-C region, however, the faster-moving anions in PA_C begins to polarize against the electrode so that the effective capacitance of the PA_C layer becomes much larger than that of the PA_A layer. At this point the capacitance value begins to approach the capacitance of the PA_A layer. In the EP-A region, the electrode polarization of the cations in PA_A begins so that the capacitance value of the PA_A layer catches up with that of the PA_C layer quickly. Whether the transition between these two regions can be clearly seen depends on how far the ω_{ep} of the two constituent layers are separated, which is determined by the ratio of

$(\sigma L_D)/(\epsilon_0 L)$ between the two layers. For the 5 bi-layer samples shown in Fig-2.19, only one sample shows a clear transition between EP-A and EP-B.

If the capacitance of the $PA_A|PA_C$ interface is much larger than both $Au|PA_A$ and $Au|PA_C$ interfaces, then the capacitance value of the sample in the LF region will approach the value of single-layer PA_C. From Fig-2.18 it is clear that the change of bi-layer capacitance value in this region is different from either the single-layer PA_A or PA_C. It starts from a value much lower than that of single-layer PA_C at the low frequency edge of EP-A to a value comparable to that of single-layer PA_A as frequency decreases. This observation suggests that in most part of the low frequency region, the effect of the $PA_A|PA_C$ interface is not negligible.

2.7 Summary

Impedance spectroscopy was used to determine the ionic conductivity, high frequency dielectric constant, ion hopping rate, activation energy of ion transport, interfacial capacitance, and effective mobile ion concentration of the conjugated ionomers PA_A and PA_C. The impedance response of the complete $Au|PA_A|PA_C|Au$ structure was also measured and compared to that of the single-layer $Au|PA_A|Au$ and $Au|PA_C|Au$ samples. Major results from this chapter are summarized as following.

The ion transport in both PA_A and PA_C are strongly activated, with similar activation energy of ~ 1 eV. The ionic conductivity of PA_A is about an order of magnitude lower than that of PA_C at same temperature, which leads to a longer characteristic response time τ_{ep} for PA_A during electrode polarization. However, at frequencies below ω_{ep} the interfacial capacitance of PA_A is higher than that of PA_C, as dictated by their similar high frequency limiting dielectric constant and the shorter Debye length of PA_A.

Equivalent circuit modeling of impedance data shows that the ion hopping rates of both ionomers exhibit similar temperature dependence with their ionic conductivity, (i.e. similar activation energy) while the hoping rate of mobile cations in PA_A is lower

than that of the mobile anions in PA_C at same temperature. This result suggests that the ions in both ionomers are fully dissociated. However, as a consequence of complete ion dissociation, the hopping distances estimated through a simple hopping model are close to 0.5Å for both ionomers, which is much shorter than the average inter-ion distances of $\sim$8Å. An additional assumption that the ions are hopping in a nearly filled environment could lead to longer hopping distances that are comparable to the ion to ion distance in the material, and effective mobile ion densities that are much lower than the stoichiometric ion density.

Analysis of impedance data through an electrode polarization model gives a Debye length of $\sim$0.8 nm for PA_A and $\sim$2.0 nm for PA_C around room temperature, which corresponds to interfacial capacitances of $\sim$4.5 F/cm^2 for PA_A and $\sim$2.3 F/cm^2 for PA_C. These interfacial capacitance values are comparable to the values of $\sim$3.5 F/cm^2 (PA_A) and $\sim$2.5 F/cm^2 (PA_C) obtained from equivalent circuit modeling. Base on the Debye length, effective mobile ion densities of the two ionomers were estimated to be within the range of $1\times10^{18}\sim2\times10^{19}$ cm^{-3}, which amounts to less than 1% of each ionomer's stoichiometric ion density of $\sim$2$\times10^{21}$ cm^{-3}.

The discrepancy between the low effective ion densities estimated through electrode polarization analysis and the full dissociation of ions suggested by the results of equivalent circuit modeling could be resolved, if one assumes that ions are fully dissociated in both ionomers but they move in a nearly filled environment. The implied room temperature electronic conductivities of both ionomers were exceedingly low ($<10^{-11}\sim10^{-12}$ S/cm), indicating a very low concentration of extrinsic electronic carriers.

The impedance response of the Au|PA_A|PA_C|Au structure is more complicated than individual single-layer structures, with the electrode polarization having a closer resemblance to that of Au|PA_A|Au. The capacitance spectrum of the Au|PA_A|PA_C|Au suggest that the PA_A|PA_C interface plays a role in the overall response of the complete sample.

CHAPTER III

ELECTROCHEMICAL CHARGE INJECTION INTO POLYACETYLENE IONOMERS

In this chapter, the process of electronic charge injection into both PA_A and PA_C will be investigated. The goal is to find out the applied voltage needed for the injection of holes and electrons into PA_A and PA_C, and show that the injected charge carriers can be balanced either by charging an electric double layer at the opposite electrode, which is a non-Faradaic process, or by the injection of charge carriers at the opposite electrode, which is a Faradaic process. It will also be shown that in the non-Faradaic process, the amount of injected charge can be controlled by both the counter electrode area and the applied potential.

3.1 Introduction

Charge injection from electrodes into MIECs plays an important role in determining the current-voltage response of MIECs as well as that of MIEC junctions. Due to the presence of mobile ions in MIECs, the charge injection process in MIECs is fundamentally different from that of pure electronically conducting materials. Charge injection into MIECs bears more resemblance to the process of doping electrochemically active materials in an electrochemical cell, where mobile ions in the electrolyte permeate into the active material. But unlike the electrochemical doping process where no current can be sustained in steady-state, a persisting electronic current can exist in MIECs under bias at steady-state due to the availability of continuous electronic pathways through the device. The steady state current, however, makes the direct measurement of the amount of injected charge and

the potential drop at each electrode|material interface in a MIECs device more complicated than in electrochemical doping experiments.

One method of isolating the charge injection process from the effect of steady-state current in Au|Ionomer|Au systems, is to break the continuous pathway for electronic charge carrier transport through the device. This can be done theoretically by cutting the sandwich structure into halves and bridge the resulting halves with an ion-conducting/electron-blocking layer. This configuration is equivalent to a typical electrochemical experiment where the counter electrode is identical to the working electrode, i.e. a symmetric cell. By monitoring the change of potential drop at each electrode as a function of total applied bias across the two electrodes, we will be able to learn when charge injection at each electrode begins, and how the charge injection processes at both electrodes affect each other. Furthermore, by implementing additional electrodes the electronic conductivity of the material can be simultaneously monitored as electronic charge carriers are being injected. Since the amount of injected charge carriers can in principle be calculated from the charge transfer current between the working and counter electrodes, it is also possible to establish the relationship between electronic charge carrier density and conductivity or charge carrier mobility through this experiment.

One could argue that the symmetric electrochemical cell is now a different system, since the continuity of the material is broken. The addition of electrolyte also changes the ionic polarization process from that of a single type of mobile ion to one that contains mobile ions of both signs. These drawbacks are inherent to the method used and can not be conveniently avoided. Nevertheless, provided that the intrinsic mobile ion concentration of the ionomers are comparable or higher that that of the electrolyte used, and the applied bias between the working electrode and counter electrode falls within the overlapping region between the stability window of the electrolyte used and the stability window of the ionomers, the onset of charge injection process that

we are interested in should occur at similar applied potential for both the symmetric electrochemical cell and the complete Au|Ionomer|Au structure.

3.1.1 Physics of electrochemical charge injection

The physics of electrochemical charge injection into materials can be illustrated by the schematic in Fig-3.1. The experiment is typically done in a liquid electrolyte, so that the injected charge can be balanced by mobile ions in the solution and charge neutrality in the bulk of the electrolyte solution is maintained. Note that in Fig-3.1, however, the ions in the electrolyte are not shown.
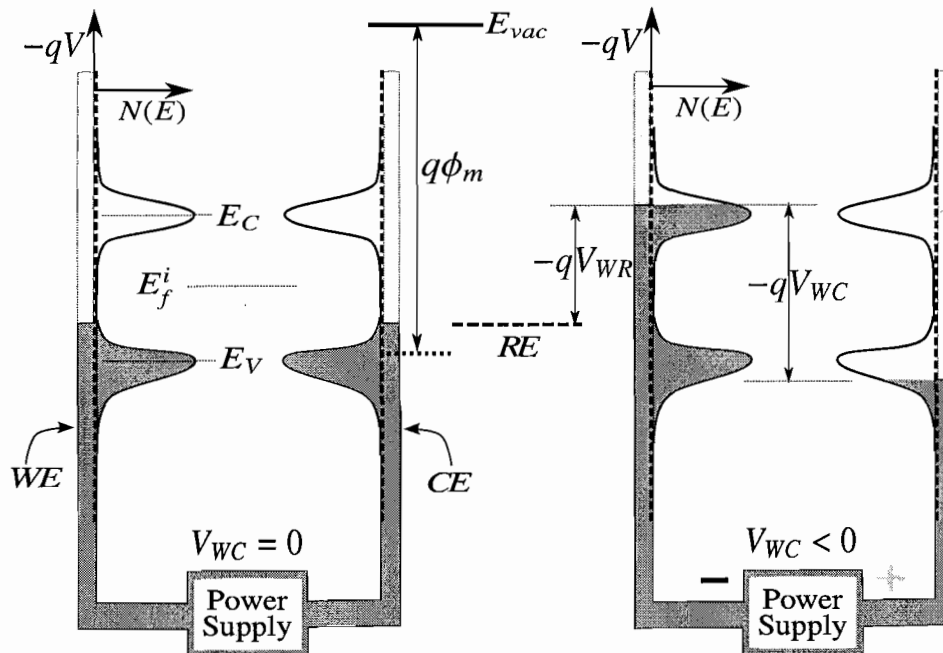
FIGURE 3.1: Schematic of an electrochemical charge injection experiment. The vertical dash lines represent the interfaces between electrode (the lightly shaded area) and its contacting active material. The heavily shaded area represents states occupied by electrons, and $N(E)$ is the density of states for electrons in the active material. ϕ_m is the electrode work function, and E_f^i is the intrinsic Fermi level of the active material. The potential of the reference electrode (RE) is considered fixed, while a voltage is applied between the working electrode (WE) and the counter electrode (CE). Charge compensating ions in the electrolyte are not shown.

Fig-3.1 schematizes the case of transferring electronic charge between two identical materials on identical electrodes. The interface between each electrode and its contacting material is represented by a vertical dashed line, where a kinetic barrier for charge transfer may exist. The lightly shaded area represents available states at the surface of electrode, and $N(E)$ is the density of state in the material, while the heavily shaded area represents states occupied by electrons at a particular bias. The electrode work function is ϕ_m, and E_f^i is the intrinsic Fermi level of the active material. The potential of the reference electrode (RE) is considered fixed, while the power supply maintains a potential difference between the working electrode (WE) and the counter electrode (CE).

Electrochemical charge injection is essentially using a power supply to shift the Fermi level of one electrode (WE) versus another electrode (CE) so that electrons are transferred between the two half cells each including the electrode and its contacting material. The presence of mobile ions in the system facilitates the equilibration of electronic charge between the electrode and its contacting material, and they provide compensating charge to the transferred electrons so that charge neutrality is maintained everywhere except in electric double layer near the electrode surfaces.

When the potential difference between WE and CE is changed electrons will be transferred from one electrode to the other, resulting in a charge transfer current. The total amount of charge being transferred for each unit of change in bias depends on the volume and DOS of both materials in contact with the electrode, therefore it's not very informative to simply monitor the change of current as a function of change in bias unless the DOS of one material is already known.

3.1.2 Cyclic voltammetry

One way to simplify the situation is the three-electrode cyclic voltammetry that is commonly used in electrochemistry, where an additional reference electrode is introduced and the potential difference between the working electrode and the

reference electrode, V_{WR}, is monitored together with the total charge transfer current, I_S, passing through the circuit. The power supply is specifically designed so that a feedback control loop senses V_{WR} and supplies whatever bias between WE and CE that is necessary to change V_{WR} at a constant rate $s = dV/dt$. The advantage of this method becomes apparent when we try to calculate I_S as a function of V_{WR}.

From Fig-3.1 the total amount of charge transferred dQ corresponding to a differential increment of the working electrode versus reference electrode dV_{WR} is:

$$dQ = -qN(E)v_m dE + C_{dl}A_{WE}dV_{WR} \tag{3.1}$$

where $dE = -qdV_{WR}$, v_m is the volume of active material, and C_{dl} is the double layer capacitance of the working electrode, and A_{WE} is the area of the WE. Therefore the total charge transfer current is:

$$\begin{aligned} I_S = \frac{dQ}{dt} &= \frac{d(-qN(E)v_m dE + C_{dl}A_{WE}dV_{WR})}{dt} \\ &= (q^2 N(E)v_m + A_{WE}C_{dl}) \times s \end{aligned} \tag{3.2}$$

Since s, v_m, C_{dl}, A_{WE} are constants, the shape of the total current as a function of V_{WR} can be directly related to the density of state function $N(E)$. Thus cyclic voltammetry provides a convenient way to determine the $N(E)$ function of an electrochemically active material. The charge injection process at the counter electrode in this type of experiments is considered unimportant and usually not a subject of interest.

3.1.3 The symmetric electrochemical cells experiment

The above cyclic voltammetry in its usual configuration, however, is not ideal for our purpose since the potential change at the CE is unknown and the effect of the electrode work function is not apparent. To mimic the charge injection process in an Au|Ionomer|Au device via the symmetric configuration as schematized in Fig-3.1, we actually want to see how the charge injection process at both the counter

electrode and the working electrode affect each other. One way to do that is to scan the potential between WE and CE, V_{WC}, at a constant rate, while monitoring both the charge transfer current I_S and the potential of WE versus RE, V_{WR}. By examining how I_S and V_{WR} changes with V_{WC}, we can learn what fraction of the applied potential is dropping at each electrode, which reflects their capacitance ratio, and infer the onset of charge injection at each electrode from the change of the capacitance ratio. Dual working electrodes or dual counter electrodes can also be implemented to monitor the conductivity change of the active material as a function of V_{WC} during the experiment.

Since the two half cells of in Fig-3.1 can be treated as two identical capacitors that have a voltage dependent capacitance reflective of the DOS of the ionomer used, the symmetric cell is in effect two capacitors in series. Therefore when voltage is scanned at a constant rate, the resulting current is proportional to the equivalent capacitance of the series combination at different voltages, while the fractional potential drop at each electrode is governed by the ratio of differential capacitance between to two half cells.

Given a suitable choice of electrode work function, e.g. the electrode Fermi level is close to but below E_f^i, one could expect to see the I_S and V_{WR} change according to the illustration in Fig-3.2 as a function of the constantly changing V_{WC}. When V_{WC} is less than V_p, only a very small amount of charge can be injected into either side of the active material, thus the I_s will resemble that for charging the electric double layers in series, which is $I_S = A \cdot s \cdot C_{dl}/2$, and the value of V_{WR} is roughly $V_{WC}/2$, given that V_{WR} starts from 0. As the applied voltage passes V_p, substantial hole injection becomes possible at the WE, making its effective capacitance much larger than the non-injecting counter electrode. At this point V_{WR} will increase much slower and most of the additional applied bias will drop at the counter electrode to charge up the double layer. The series capacitance of the two half cells is now approximately C_{dl}, so the current is now $I_S = A \cdot s \cdot C_{dl}$. When V_{WC} increases to V_{pn},
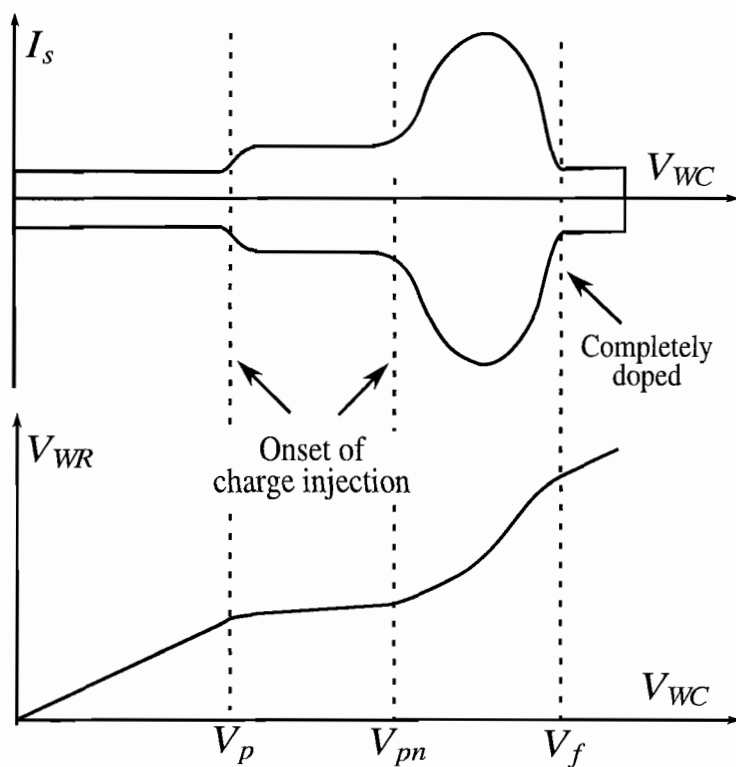
FIGURE 3.2: An illustration of the expected change in I_s and V_{WR} as a function of V_{WC} changing at a constant rate of s, for a particular choice of electrode work function.

enough potential drop has accumulated at the counter electrode to drive substantial electron injection into the material, so that the overall current I_S increases rapidly, while V_{WR} also increases faster due to the higher achievable carrier concentration (doping level). As the applied bias further increases to V_f, the material on both sides will be fully doped, and therefore both half cells will behave just like double layer capacitors in series again.

Since the cell is symmetric, the behavior at the opposite sign of bias can be easily inferred from Fig-3.2. Note that the schematic in Fig-3.2 is an idealized result, in a real experiment the transitional points may not be so clear, and the electrochemistry of the electrolyte as well as the complex real DOS of the ionomer could result in a much more complicated $I_S(V_{WC})$ and $V_{WR}(V_{WC})$.

3.1.4 The electrochemical transistor experiment

In the previous subsection, It was shown in theory that charge injection into a material at one electrode can be coupled to either the charging of an electric double layer, which is a non-Faradaic process, or the injection of the opposite charge carrier, which is a Faradaic process, at the counter electrode. By scanning V_{WC} at a constant rate and monitoring the change of V_{WR} and I_S, it is possible to identify the onset voltage of hole and electron injection from a given electrode into the material.

Now if we modify this experiment setup by replacing one of the two half cells with a sandwich Au|Ionomer|Au structure, and apply a bias between the two electrodes of Au|Ionomer|Au in addition to the bias between one of the two electrodes of Au|Ionomer|Au and the counter electrode, the setup is essentially a typical transistor. The voltage between WE and CE controls the amount of charge carriers being injected into the ionomer in the Au|Ionomer|Au structure, and the charge carrier density in turn determines the current (conductivity) between the two Au electrodes of the Au|Ionomer|Au. This type of transistor is termed "electrochemical transistor", or

"electrolyte gated transistors",[66, 67, 68] and they are notable for supporting high carrier densities at relatively low gate voltages and for slow switching times.

As we have shown theoretically in the symmetric electrochemical cell experiment, the coupling of charge between the working electrodes (source and drain) and the counter electrode (gate) in an electrochemical transistors can be either non-Faradaic or Faradaic, depending on gate voltage and materials used. Based on the analysis of the previous subsection, one would expect very different transfer characteristics when different gate electrode processes are involved. For instance, when the gate voltage is within the Faradaic regime, one would expect that the conduction current (I_{SD}) to be very strongly modulated by the gate voltage, due to its ability to support large amount of charge carrier injection. On the other hand, when the gate voltage operates within the non-Faradaic regime, the conduction current would be less sensitive to the change of gate voltage, but it could be modulated more precisely due to the near-linear relationship between charge and applied voltage for double layer charging.

So far most of the studies on electrolyte-gated transistors have used a plain gate electrode, and most of the attention has been focused on the transfer characteristics of devices based on a variety of materials, while little attention has been paid to the electrochemical aspects of the device operation. An experimental demonstration of the impact of different gate electrode processes on the device transfer characteristics can provide a new principle for electrochemical transistor design.

3.2 Experimental details

3.2.1 Sample preparation

All Au|Ionomer|Au samples were prepared by the same method as described in section-2.2 of Chapter-II. For the symmetric electrochemical cell experiment, up to four closely spaced samples on separate electrodes of the same working area

are prepared on the same glass slide, with one or two of them having a complete Au|Ionomer|Au structure and the rest without the top Au electrode. For the electrochemical transistor experiment, only one Au|Ionomer|Au sample is prepared on each glass slide. All samples used in this chapter are vacuum dried for at least 4 hours before use, but not annealed at elevated temperature.
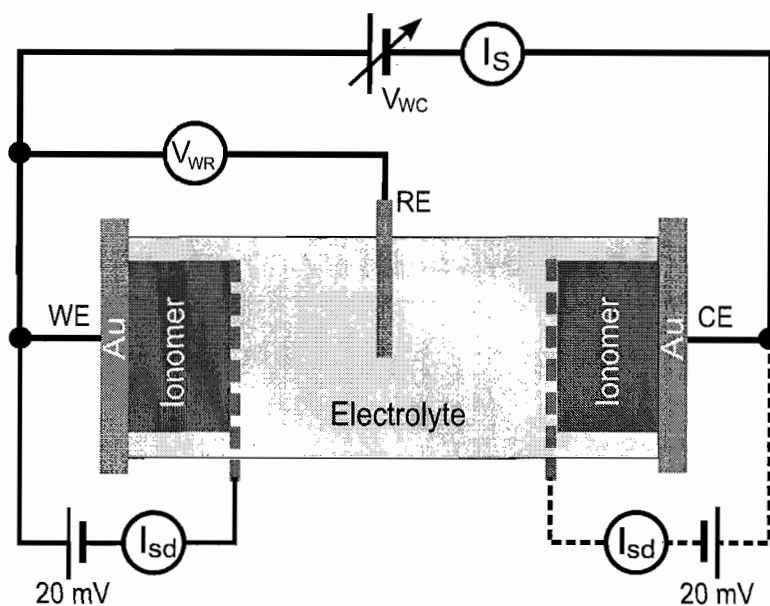
FIGURE 3.3: Schematic of the instrumental setup of an electrochemical charge injection experiment using a symmetric cell configuration.

3.2.2 Instrument setup

A schematic of the experimental setup for symmetric electrochemical cell experiments is shown in Fig-3.3. The setup for electrochemical transistor experiment is similar, except the counter electrode (gate electrode) in Fig-3.3 is replaced by platinum wires of various lengths. During the symmetric electrochemical cell experiment, 0.075 M tetramethylammonium tetrafluoroborate (TMABF$_4$) in acetonitrile (CH$_3$CN) was used as the electrolyte, and a bare Au electrode in the electrolyte solution was used as the reference electrode. While in the electrochemical

transistor experiment, 0.1 M tetrabutylammonium tetrafluoroborate (Bu_4NBF_4) in CH_3CN was used as electrolyte, and a Ag/Ag^+ reference electrode was used.

In the schematic shown in Fig-3.3, a Solartron 1287 electrochemical interface was used to supply V_{WC} and measure I_S, a Philips PM2534 digital multimeter was used to measure V_{WR}, and a Keithley 2400 SMU was used to maintain a small potential difference V_{SD} between the two working electrodes and measure I_{SD}.

3.3 Results and discussion

3.3.1 Electrochemical charge injection into PA_C

The result of a symmetric cells experiment on PA_C sample is shown in Fig-3.4 for a moderate range of V_{WC} ($\pm1.1V$), together with a baseline scan between two bare electrodes to check the quality of electrolyte. Both scans in the figure were at 50mV/s. As can be seen from Fig-3.4, the scan of the electrolyte (top, dash line) shows a typical charging current of the electric double layer up to about $\pm1.5V$. Although beyond $\pm1.5V$ the current deviates from that of double layer charging, the current at $\pm2.0V$ is less than 4 μA.

The solid line in the top half of Fig-3.4 shows the I_S versus V_{WC} for a scan between a $Au|PA_C$ (WE) and a $Au|PA_C|Au$(CE) in the range of $\pm1.1V$, while the corresponding change in V_{WR} is shown by the solid line in the bottom half of the figure. When V_{WC} is positive, from 0V to about $+0.8V$, the current I_S started from the baseline value and increased to about 3 times larger at about $+0.4V$, but remains typical of charging an electric double layer. I_S started to increase rapidly after about $+0.8V$. The working electrode potential, however, increased only slowly from $\approx0V$ at $V_G=0V$ to $\approx0.17V$ at $V_G = +1.1V$, which indicates that most of the applied potential V_{WC} is dropping at the counter electrode interface during the positive half cycle of the scan. The conductivity of the ionomer film at the counter electrode as indicated
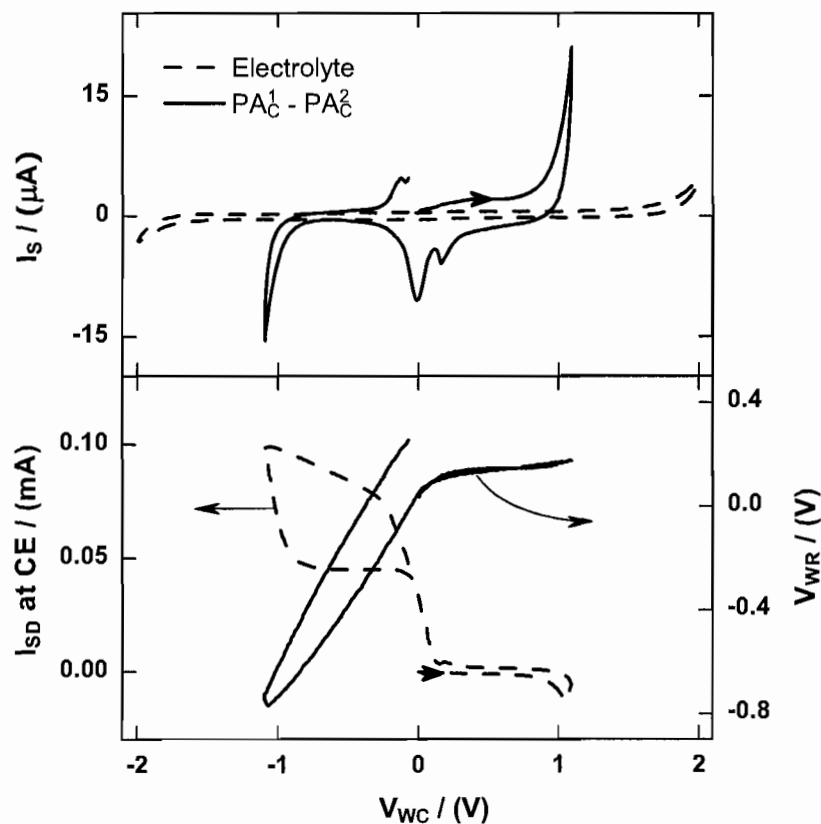
FIGURE 3.4: The stability window of electrolyte and the charge injection into PA_C in the moderate bias range. The same scan rate of 50mV/s was used for both scans. Top: the dash line shows I_S as a function of V_{WC} when the applied potential was scanned between a pair of bare Au electrodes in electrolyte, and the solid line shows the change of I_S when the voltage is scanned between a $Au|PA_C(WE)$ half cell and a $Au|PA_C|Au(CE)$ half cell. Bottom: the solid line shows the change of working electrode potential V_{WR} with V_{WC}, and the dash line shows the change of I_{SD} between the two Au electrodes of the $Au|Ionomer|Au$ used as the CE, with V_{SD}=10mV. The direction of scan is indicated by thick arrowheads.

by I_{SD} did not seem to increase visibly during the positive half cycle. Note that the seemingly negative value of I_{SD} around $V_{WC}=+1.1$V is an artifact of the circuit since both Au electrodes of the Au|Ionomer|Au function as part of the counter electrode during the scan. This artifact can be minimized by scanning slower, or averaging over two scans where the sign of V_{SD} is switched.

Reversing the sign of V_{WC} is in effect switching the role between WE and CE, therefore, in a perfectly symmetric cell, one would expect to see just the same behavior of I_S except a change in the sign of current, while the change in working electrode potential would now reflect the change of potential drop at the counter electrode during the positive half cycle. However, as can be seen in Fig-3.4, the magnitude of I_S is smaller at -1.1V than at +1.1V. This slight asymmetry can be explained by the difference in effective electrode area between Au|Ionomer|Au and Au|PA$_C$, since the two electrodes in Au|PA$_C$|Au are connected through the SMU during the scan. The conductivity of the ionomer at the counter electrode increased substantially during the negative half cycle as shown in Fig-3.4. The change of I_{Sd} suggest that hole injection at the CE has lead to a substantial increase of conductivity. The close to linear relationship between V_{WR} and V_{WC} during the negative half cycle is typical of double-layer charging.

One could also notice in Fig-3.4 that at the end of the scan, both the charge transfer current I_S and the working electrode potential V_{WR} did not return to their starting values. This seems to indicate that during the negative half cycle, some charge were trapped at the working electrode. Meanwhile, the potential of the Au reference electrode might also have drifted slightly during the cycle.

According to the illustration in Fig-3.2, the behavior of I_S and V_{WR} in Fig-3.4 suggest that within the bias range of ± 1.1V, the electrochemical cell was operating primarily in the second region where the injection of holes at the working electrode was balanced predominantly by the non-Faradaic process of electric double layer charging at the counter electrode. This result indicates that the system at equilibrium

can be described by the left half of Fig-3.1, and it is consistent with the fact that the work function of gold is very close to the valence band of PA_C. The first region in Fig-3.2 can not be clearly identified in Fig-3.4 since the onset of hole injection at WE begins at close to zero bias. To observe the onset of electron injection at the counter electrode, it will be necessary to increase the range of V_{WC} further.
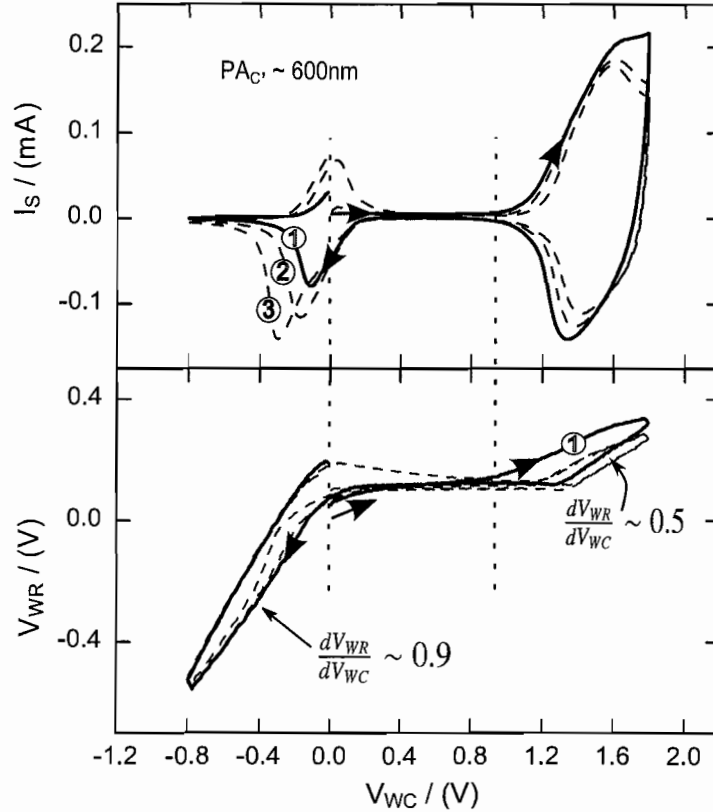
FIGURE 3.5: The change of charge transfer current I_S(top) and working electrode potential V_{WR}(bottom) of PA_C samples in a symmetric cell configuration during three scans of V_{WC} in the range of -0.8V~+1.8V. The solid line is the result of the first scan. The order of scans are indicated by the numbers, and direction of the scan indicated by the arrowheads. The scan rate used was 50mV/s.

Fig-3.5 shows the change of charge transfer current I_S and the working electrode potential V_{WR} of PA_C during three successive cycles of V_{WC} between -0.8V and +1.8V. The number on each curve indicates the order of that scan. One could have

used a symmetric V_{WC} range like ± 1.8V, but the ionomer was observed to degrade substantially between scans if such extended bias range is used, and theoretically, scanning in one direction is sufficient since the system is symmetric.

Based on the changes in V_{WR}, three bias regions can be identified in Fig-3.5 as indicated by the two vertical dotted lines. In the first(left) region where V_{WC} is negative, the value of dV_{WR}/dV_{WC} was observed to be close to 0.9 and a peak in the charge transfer current I_S that shifts to more negative potentials on successive out-going scans can be identified. In the second region between the two vertical dotted lines where V_{WR} changes slowly, the I_S was close to the double-layer charging baseline during the first scan. In the third region where V_{WC} was higher than about $+0.9$V, V_{WR} changes more rapidly than in the second region with dV_{WR}/dV_{WC} close to 0.5, while the charge transfer current I_S changes by several orders of magnitude. The large negative charge transfer current during the backward scan from $+1.8$V to 0V indicates that most of the charge transferred during the out-going positive scan were returned. A previous study has shown that the injection of electrons into PA_C leads to improvement ionomer conductivity, although less significant than when holes are injected.[24]

The behavior of V_{WR} and I_S at $V_{WC}<0.9$V is similar to what's been observed in the lower bias range, while the changes in V_{WR} and I_S at $V_{WC}>0.9$V qualitatively match what was illustrated in the third region of Fig-3.2. This suggests that the injection of holes at the WE is now Faradaically coupled to the injection of electrons at CE, and the applied potential needed for this bipolar injection is about 0.9V. Given the good reversibility of the charge injection process at $V_{WC}>0.9$V, it is unlikely that significant electrolyte reaction was involved. The difference between the first and second scans seem to indicate that some irreversible changes in the ionomer or at the Au|PA_C interface might have occurred due to the large amount of injected charge.

3.3.2 Electrochemical charge injection into PA_A

The result of electrochemical charge injection experiment on PA_A is shown in Fig-3.6 for V_{WC} between -0.6V and +1.5V, and in Fig-3.7 for V_{WC} between -1.5V and +0.6V. The source-drain current I_{SD} was also shown in both figures to compare the change of ionomer conductivity during the cycles. In general three distinct regions of V_{WR} can be identified in a similar way to the PA_C results (see Fig-3.5). In the first region where $V_{WC}<0$, the potential of the working electrode changes with V_{WC} linearly with a slope of ≈ 0.8. In the second region between the two vertical dash lines, the value of V_{WR} changes only slightly. In the third region where V_{WC} is higher than about 1.0V, the value of V_{WR} increase faster and reaches a linear slope of ≈ 0.5 after $V_{WC}>+1.2V$ on the out-going scan. However, for PA_A the transition from the second to the third region is more gradual than in PA_C, a transitional region between +0.8V and +1.2V as indicated by a shoulder in I_S can also be identified.

The behavior of I_S in Fig-3.6 is quite different from that of the PA_C in that, most of the charge transferred during the out-going positive scan were not reversed on the way back to 0V. This can be seen clearly in both the lack of a negative current from +1.5V back to 0V, and the preserving of high conduction current I_{Sd} during the backward scan. Those charge are reversed almost completely when V_{WC} was scanned to more negative than -0.4V, as indicated by the decrease of I_{Sd}. The close to complete return of all injected charge at -0.4V suggest that a barrier exists for the Faradaically coupled charge injection process of PA_A. The involvement of electrolyte reaction, however, is unlikely given the low magnitude of negative potential that is needed for the charge reversal.

The faster increase of V_{WR}, and rapid increase of both I_S and I_{Sd} at around $V_{WC}=1.0V$ seem to suggest that the onset of Faradaic charge transfer process at CE enables substantial increase of hole injection at the working electrode after V_{WC} was increased to more positive than 1.0V. As an attempt to verify the potential change at the counter elector and to find out whether the Faradaic charge transfer process at
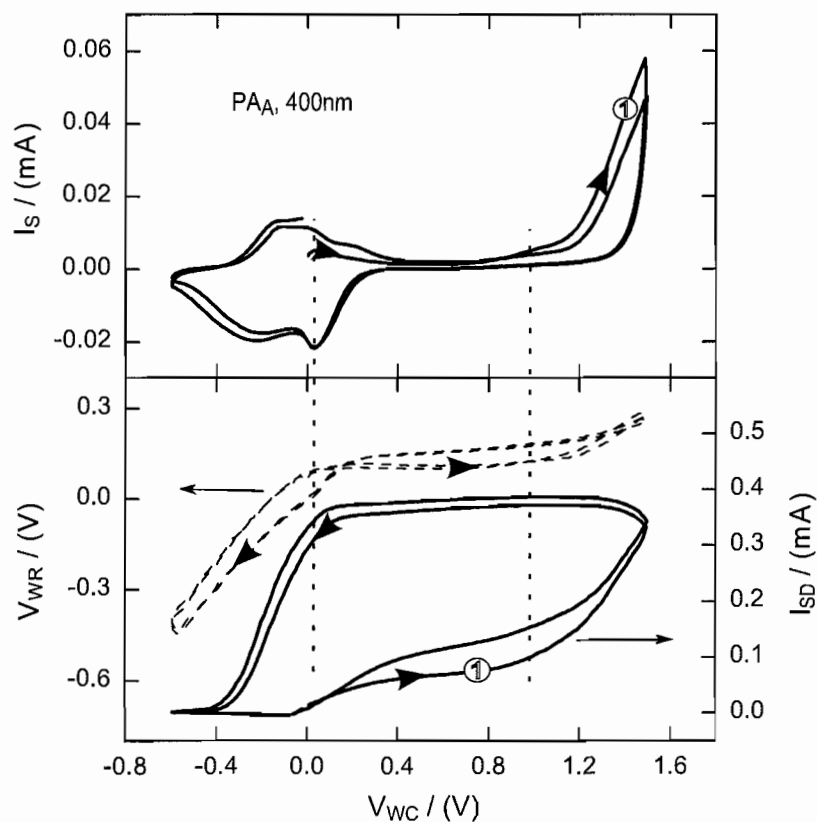
FIGURE 3.6: The change of charge transfer current I_S (top), working electrode potential V_{WR}(bottom, dash line), and conductivity current I_{SD} (bottom, solid line) of PA_A samples in symmetric cell configuration during two consecutive scans of V_{WC} in the range of -0.6V~+1.5V. The direction of a scan is indicated by the arrowheads, and the scan rate used was 50mV/s. The bias between the two electrodes of $Au|PA_A|Au(V_{SD})$ was 20mV.

the counter electrode changes the ionomer's conductivity, the direction of scan and the range of V_{WC} was changed to switch the roles between WE and CE.
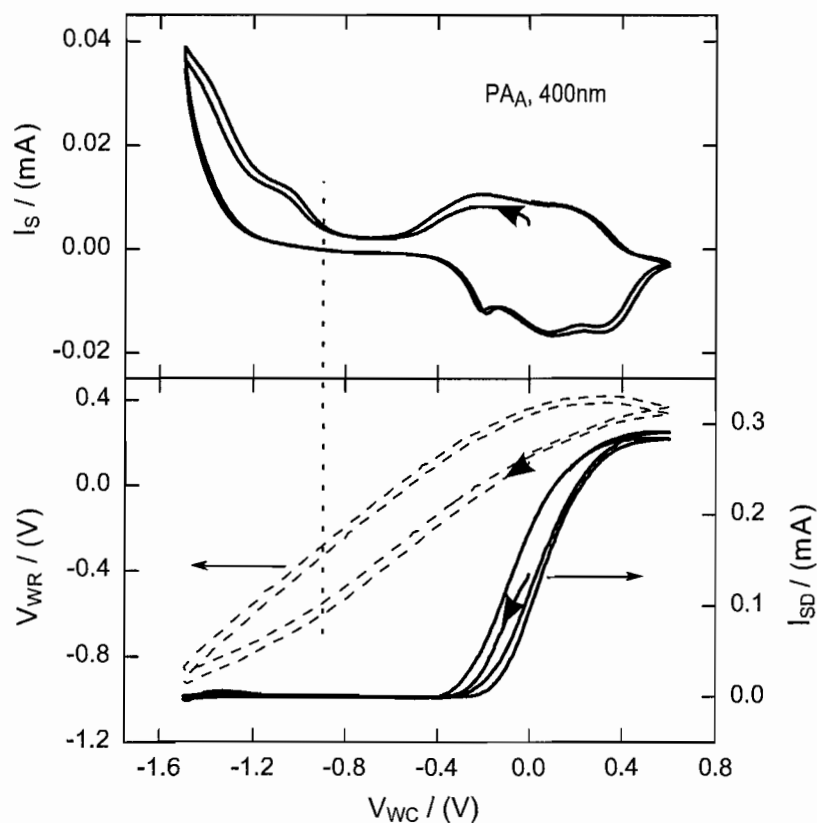
FIGURE 3.7: The change of charge transfer current I_S(top), working electrode potential V_{WR}(bottom, dashline), and conductivity current I_{SD}(bottom, solid line) of PA$_A$ samples in symmetric cell configuration during two consecutive scans of V_{WC} in the range of -1.5V~+0.6V. The beginning of the scan is indicated by arrowheads, and the scan rate used was 25mV/s. The bias between the two electrodes of Au|PA$_A$|Au(V_{SD}) was 20mV.

The result of such a scan is shown in Fig-3.7. As can be seen from Fig-3.7, the shape of the charge transfer current I_S is almost the mirror image of the I_S shown in Fig-3.6, which is not surprising given the approximate symmetry of the system. Note the scan rate was different so the magnitude of the current differs.

The potential of CE (V_{WR}) changes almost linearly with V_{WC} during the negative out-going scan, but the slope changes from $\approx$0.8 to $\approx$0.5 at the point indicated by

the vertical line ($V_{WC} \approx$-0.9V) in Fig-3.7. This change of slope suggest that at bias potentials more negative than about -0.9V, most of the potential drop occurs at the counter electrode, but when V_{WC} goes to more negative than -0.9V the additional bias drops about equally on both the WE and CE. The linear change of V_{WC} during the scan from -1.5V to -0.5V at a constant slope of 0.8 is typical of discharging the double layer and consistent with the observation that most of the charge transferred during the scan between -0.9V and -1.5V(where $dV_{WR}/dV_{WC} \approx$0.5) were not returned during the backward scan from -1.5V to 0V.

As shown in Fig-3.7, there seem to be no clear increase of ionomer conductivity at the counter electrode between -1.5V and -0.4V, while the change of conductivity between -0.4V and 0.6V is consistent with what was observed in Fig-3.6. The absence of ionomer conductivity increase at the counter electrode in the Faradaic region suggest that the injected electrons might have very low mobility. This observation is in agreement with the results of an earlier study on the electrochemical doping of PA_A, where a large charge transfer current was observed when the ionomer was scan to sufficiently negative potentials, but improvement of ionomer conductivity was not observed.[24]

3.3.3 Gate electrode processes in electrochemical transistors

The symmetric cell configuration employed in the previous subsection was useful in simulating the charge injection process in a Au|Ionomer|Au structure. It is not ideal, however, for demonstration of Faradaic and non-Faradaic charge transfer processes at the gate electrode of an electrochemical transistor because of the unnecessary complication from additional materials at the gate electrode. Therefore in the electrochemical transistor experiment, an inert platinum wire electrode was used as the gate electrode (or counter electrode). In this experiment, PA_C was used as the active material at the working electrode and 0.1 M Bu_4NBF_4 in CH_3CN was used as electrolyte.

In an electrochemical transistor with an ion permeable active material, the output characteristics are determined by the relation of the ionomer's conductivity to it's doping level. Due to the presence of mobile ions in the ionomer, the conduction of electronic charge could be dominated by diffusion. Therefore the conductivity of the ionomer is presented in terms of the source-drain current I_{SD} in response to a small source-drain voltage V_{SD} versus the potential of the working electrode V_{WR}. A typical I_{SD}–V_{WR} relation for PA_C is shown in Fig-3.8. The amount of hysteresis observed in Fig-3.8 primarily depended on the scan rate relative to the time scale for the doping process, although a component of the hysteresis can also come from history effects.[24]
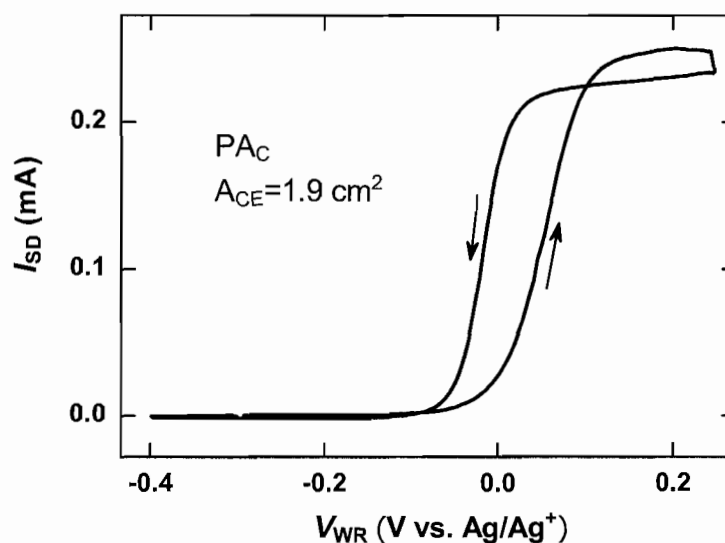
FIGURE 3.8: The sour-drain current I_{SD} as a function of working electrode potential V_{WR} during a scan of V_G on a PA_C sample at 20mV/s. The gate electrode area was 1.9 cm^2

To demonstrate the differences in transfer characteristics of the transistor between Faradaic and non-Faradaic regime, the gate voltage was scanned within the range of -1.5V $\sim$ +3.0V (WE vs. CE) at 20mV/s. The change in gate current, I_G, and

working electrode potential versus Ag/Ag$^+$ reference electrode,V_{WR}, during the scan is shown in Fig-3.9.
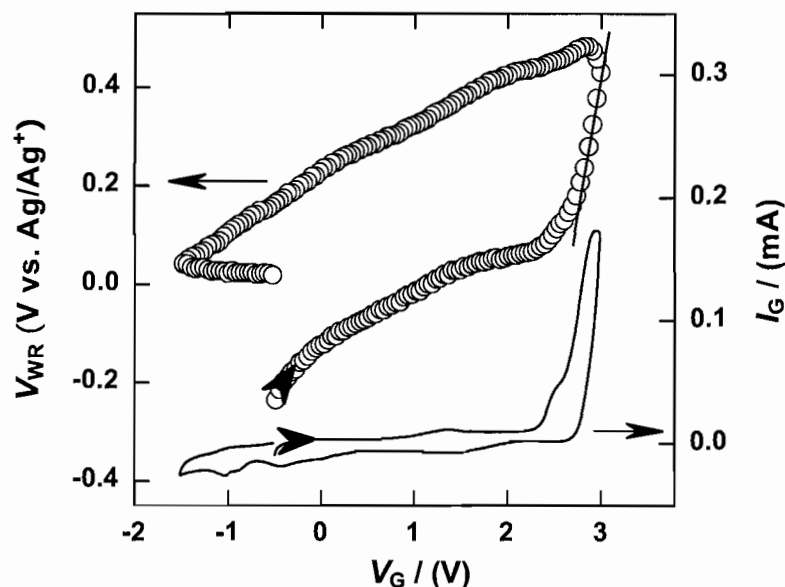
FIGURE 3.9: Working electrode potential V_{WR}(open circles) and gate electrode current I_G (solid line) as a function of gate voltage V_G for a gate electrode of 1.3 cm^2. The scan rate was 20mV/s. The beginning of the scan and its direction are indicated by the arrowheads. A linear fit to the V_{WR} versus V_G data in the Faradiac regime is shown and corresponds to dV_{WR}/dV_G=1.0 .

During the out-going positive scan from -0.5V to +3.0V in Fig-3.9, two regions of change in I_G and V_{WR} can be identified. In the first region between -0.5V and +2.4V, the gate current I_G stays relatively low and near constant, while the working electrode potential V_{WR} increases slowly from -0.3V to 0V. In the second region between +2.4V and +3.0V, the gate current increases drastically by orders of magnitude while the potential of WE also increases rapidly from 0V to about 0.5V. As the gate voltage was scanned from +3.0V down to -1.5V, the magnitude of negative gate current I_G is higher than the gate current between -0.5V and +2.4V but remains relatively flat, while the working electrode potential decreases steadily from about +0.5V to slightly above 0V. During the scan from -1.5V back to -0.5V, the gate current remains low,

and the working electrode decreases only slightly. Thus at the end of the whole cycle, the working electrode potential is about 0.3V higher than where it started.

The slow change of V_{WR} in the first region indicates that during this gate voltage range, almost all of the applied potential is dropping at the gate electrode. The small and near constant gate current in this region and the large fraction of potential drop at gate electrode can be explained if holes were injected into the PA_C film and the injected charge were balanced by charging an electric double layer at the gate electrode, since the non-Faradaic double layer charging process has a much smaller capacitance compare to the Faradaic process of injecting charge into the ionomer.

In the second region where $V_G > 2.4V$, the rapid increase of the working electrode potential and I_G indicates that the equivalent capacitance of the WE is now much smaller than that of the counter electrode, which can happen only if the charge transfer process at the gate electrode also become Faradaic, i.e. the reduction of electrolyte at the CE. The observation that at the end of the scan, the WE potential is about 0.3V higher than the starting value is consistent with reduction of electrolyte. Since a portion of the reaction product may diffuse away from the counter electrode during the scan, those charge cannot be recovered at the end of the scan, leading to net p-doping of the ionomer as reflected by higher potential of the working electrode.

According to the difference in gate electrode process, the first region described above is defined as the no-Faradaic regime, and the second region is defined as the Faradaic regime.

As can be seen from Fig-3.9, the greatest possible sensitivity of I_{SD} to V_G is observed when the transistor is operating in the Faradaic regime. Any incremental increase in V_G appears almost entirely as a shift in V_{WR} as evidenced by $dV_{WR}/dV_G \approx 1$. This implies that I_{SD} versus V_G will be identical to that of Fig-3.8 in the Faradaic regime with V_{WR} replaced by V_G and a simple shift across the voltage axis. For the PA_C transistor, a maximum sensitivity of $dV_G/dI_{SD}=75$ mV/decade was observed. This is near the 60 mV/decade expected at room temperature for

a carrier concentration that is linearly proportional to the source-drain current and governed by the Nernst equation for a one electron oxidation/reduction in the low doping level limit. At higher doping levels, the conductivity of many conjugated polymers peaks and then decreases due to the hopping nature of the transport.

In the Faradaic regime the transistor operates with the irreversible reduction – a Faradaic process – of the electrolyte used. Sufficient V_G has been applied to move V_{GR} to the limit of the stability window of the electrolyte. A near constant value of $V_{GR} = V_G - V_{WR}$=2.5 V versus Ag/Ag+ was observed in the Faradaic regime, consistent with the accepted stability window of CH_3CN/Bu_4NBF_4. The constancy of V_{GR} results from the large capacitance of the electrolyte for irreversible redox chemistry, depending of course on its quantity. This large capacitance results in incremental increases in V_G appearing entirely at the active material leading to $dV_{WR}/dV_G \approx 1$. The irreversible nature of the Faradaic mode of operation is illustrated by the fact that V_{WR} does not return to its initial value in the return sweep of Fig-3.9. There is some return due to the discharge of the ionic double layer, but the component of the doping that was coupled to irreversible reduction of the electrolyte is not recovered. Removal of this additional charge requires driving V_G sufficiently negative to drive the irreversible oxidation of the electrolyte. The fact that the Faradaic mode of operation relies on the irreversible oxidation/reduction of the electrolyte also means that the transfer characteristics will decay with time and be particularly sensitive to the nature of the electrolyte including any impurities such as those generated on irreversible electrochemical degradation.

The limitations imposed by the irreversible nature of the Faradaic regime can be overcome by the intentional introduction of a reversible redox couple at the gate electrode,[69] such as the symmetric cell configuration that was used in the electrochemical charge injection experiment. This approach can potentially lower the operating voltage of the device, but does increase device complexity and introduces another possible bottleneck in achievable switching times. It is noted that certain

common electrolytes themselves provide a reversible redox couple such as those based on alkali metal salts where metal plating and stripping are possible.

The non-Faradaic mode of operation is an interesting alternative to the Faradaic mode discussed above. In this mode, V_{GR} remains within the stability window of the electrolyte, and polymer doping is coupled to the reversible charging of an ionic double layer – a non-Faradaic process – at the gate electrode. This mechanism is similar to that implemented in the so-called asymmetric capacitor devices.[70] When the transistor is operating in the non-Faradaic regime, the sensitivity of I_{SD} to V_G is determined by the quantity (or equivalent capacitance) of active material and the capacitance of the gate electrode. To demonstrate the effect of this capacitance ratio, three Pt electrodes of different surface areas were used as the gate electrode against the same working electrode. The resulting I_{SD} versus V_G is shown in Fig-3.10. An alternative presentation of the result in terms of I_{SD} versus V_{WR} is shown in Fig-3.11.
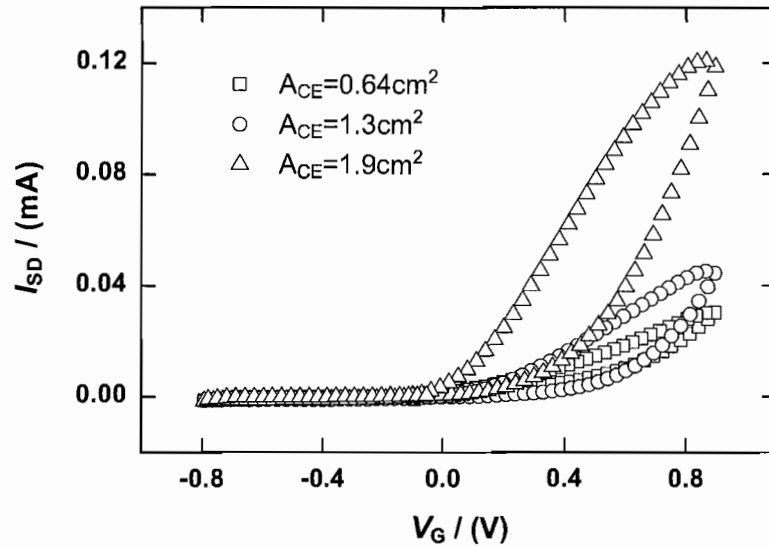
FIGURE 3.10: The source-drain current I_{SD} as a function of gate voltage V_G scanned at 10mV/s within the non-Faradaic regime, with tree different gate electrode areas – 0.64 cm^2 (open squares), 1.3 cm^2 (open circles), and 1.9 cm^2 (open triangles). V_{SD}=20mV.
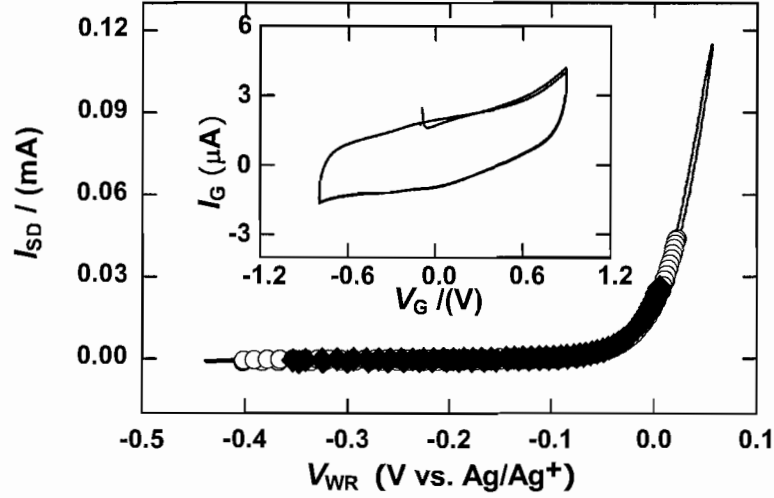
FIGURE 3.11: The source-drain current I_{SD} (at V_{SD}=20mV) as a function of working electrode potential V_{WR} of a PA$_C$ sample during scans of V_G between -0.8V$\sim$+0.9V at 10mV/s, with tree different gate electrode areas – 0.64 cm^2 (solid diamonds), 1.3 cm^2 (open circles), and 1.9 cm^2 (solid line). The inset shows the gate electrode current I_G versus gate voltage V_G for A_{CE}=1.9 cm^2.

A plot of I_G versus V_G (see the inset in Fig-3.11) for A_{CE}=1.9 cm^2 confirms that the doping process is limited by the charge-voltage relation for ionic double layer formation. The slightly distorted charging box observed is as expected for the charging of an inert electrode in an inert electrolyte solution. The impact of the capacitance ratio between WE and CE can be seen in Fig-3.11, which shows I_{SD} versus V_{WR} for three different gate electrodes each with a different surface area A_{CE} and hence total capacitance. Each trace follows the same functional form because the I_{SD} versus V_{WR} relation is an intrinsic property of the polymer. The level of doping achieved, however, depends on A_{CE}, as evidenced by the increase in the maximum values of both I_{SD} and V_{WR} reached at positive V_G with increasing A_{CE}. Note that although the time constant for charging will be affected, the absolute level of charging does not depend on the geometrical arrangement of the gate electrode relative to the active material, a situation that is much different than in field effect transistors. As the capacitance of the gate electrode increases, the sensitivity of I_{SD}

to V_G also increases. The minimum values of dV_G/dI_{SD} range from 0.55 V/decade for A_{CE}=0.64 cm^2 to 0.40 V/decade for A_{CE}=1.9 cm^2. These gate electrodes are 5 and 15 times, respectively, the active area of the PA$_C$ film.

As demonstrated above, the transfer characteristics of an electrochemical transistor operating in the non-Faradaic regime depends strongly on the ratio between the equivalent capacitance of the active material and the capacitance of the gate electrode. In Fig-3.11 it is illustrated that by changing the electrode capacitance one can control the sensitivity of I_{SD} to V_G. Alternatively, the sensitivity can also be controlled by changing the capacitance of the active material, e.g. by changing the thickness of the ionomer layer.
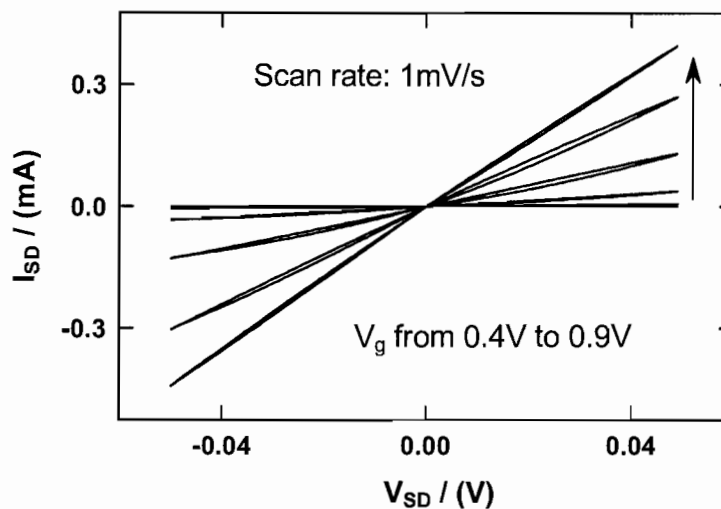
FIGURE 3.12: The source-drain current I_{SD} versus applied source-drain voltage V_{SD} for static gate voltages V_G from 0.4V to 0.9V in 0.1V increment. The arrow indicates the increase of V_G.

Instead of measuring the source-drain current I_{SD} under constant V_{SD} during a scan of V_G to monitor the doping of the ionomer film, a different method mimicking a FET can also be used. Fig-3.12 shows the result of an experiment where the gate voltage V_G was hold constant while the source-drain current I_{SD} is measured as a function of source-drain voltage V_{SD}. The change in the conductivity of the ionomer

was clearly demonstrated by the change of slope in I_{SD} as the gate voltage V_G was changed from $+0.4$ V to $+0.9$ V in 0.1 V increment.

3.4 Summary

In this chapter, the electronic charge carrier injection into individual PA_A and PA_C ionomer from Au electrodes in the presence of electrolyte was investigated using a symmetric electrochemical cell configuration, where the active material – PA_A or PA_C – were coated onto both the working electrode and the counter electrode. The charge transfer current and working electrode potential versus a reference electrode, as well as the conductivity of the active material, were monitored as a function of applied bias between the working electrode and the counter electrode. The results were analyzed to identifying the onset voltages of hole and electron injection into both ionomers from Au electrodes. The experimental setup was then modified into an electrochemical transistor to investigate the distinctions between two different operating regimes of electrolyte gated transistors and their impact on the transfer characteristics of the transistors.

In the charge injection experiment, it is found that for both PA_A and PA_C, hole injection begins at close to zero bias, but the amount of charge injected is limited by the non-Faradaic charging of electric double layer at the counter electrode until the bias is sufficiently high to enable the Faradaic transfer of electrons at the counter electrode. For PA_C, reversible electron injection into the ionomer at the counter electrode occurs when the potential difference between working electrode and counter electrode exceeds 0.9V. For PA_A, the onset of substantial electron injection at the counter electrode begins at around 1.2V, but less significant injection of electrons starts as early as 0.8V. Unlike the PA_C, the Faradaic electron transfer process of PA_A at the counter electrode was much less reversible.

In the electrochemical transistor experiment, two different operating regimes of electrolyte gated transistors that involve different gate electrode processes were

demonstrated, and the output characteristics of the two operating modes were compared. Greatest sensitivity of source-drain current to gate voltage can be achieved when the transistor was operating in the Faradaic regime, where the doping of active material is coupled to the electrochemical reaction of electrolyte at the gate electrode. When the transistor operates in the non-Faradaic regime, where the doping of active material is coupled to the charging of electric double layer at the gate electrode, it was demonstrated that the sensitivity of source-drain current to gate voltage depends on the capacitance ratio between the active material and the gate electrode. Guiding principles for electrochemical transistor design were proposed according to different modes of operation.

CHAPTER IV

ELECTRICAL CHARACTERIZATION OF INDIVIDUAL IONOMER IN AU|IONOMER|AU CONFIGURATION

In this chapter, current-voltage measurements on single-layer Au|Ionomer|Au structures are carried out to investigate the effect of ionic conductivity and ion density on the injection and transport of electronic charge carriers for each ionomer. The amount of electronic charge carriers injected at different bias levels and their effect on overall conductivity are also estimated.

4.1 Introduction

The electronic charge carrier injection processes at the Au|Ionomer interfaces of both PA_A and PA_C were investigated in Chapter-III through the symmetric electrochemical cell experiment. It was found that the onset voltages of bipolar injection for both PA_A and PA_C are similar, while the reversibility of the electron injection process differs between PA_A and PA_C. It was also found that for both ionomers, the injection of holes leads to a more significant increase of ionomer conductivity than the injection of electrons. These results suggest that the complete Au|Ionomer|Au structure of PA_A and PA_C would likely show similar I-V response at steady state, unless the charge injection process is drastically affected by the presence of electrolyte and/or the electronic conduction current.

In the electrochemical charge injection experiment, the electrolyte provides effectively unlimited mobile ions for compensating the charge being injected into the ionomer, therefore the amount of charge that can be injected is only limited by the capacitance (volume) of the ionomer on each electrode. In a dry Au|Ionomer|Au

sample, however, the injected charge carriers are compensated by the depletion and accumulation of the limited amount of mobile ions in each ionomer. Furthermore, the impedance study in Chapter-II indicates that both ionomers's effective mobile ion concentrations could be much lower than their corresponding stoichiometric ion concentrations, and the ionic conductivity of PA_A is about an order of magnitude lower than that of the PA_C at same temperature. The lower availability of charge-compensating ions in the dry Au|Ionomer|Au structure will likely limit the amount of injected charge achievable at a given bias, but at what bias level this happens and to what extend the amount of injected charge will be affected is not clear.

On the other hand, the interplay between the ionic transport and the electronic transport in mixed conducting systems with ion blocking electrodes like the Au|Ionomer|Au has been a subject of intense investigation due to their potential application in solid-state lighting,[2, 3, 71, 4] photovoltaics,[6, 7, 10] thin-film and electrochemical transistors,[68, 72, 73, 69, 74] and memory devices.[14] The redistribution of mobile ions in these Mixed Ionic/Electronic Conductor (MIEC) systems under bias makes in-situ doping of the active material possible, thus changing the electrical and optical characteristics of these systems in ways that are more complex and feature-rich than their pure electronic counterparts. A thorough understanding of the interaction between ionic and electronic charge carriers in these MIEC systems is essential to the design and optimization of devices based on these materials. One important question to the understanding of MIEC systems is how does mobile ion concentration in these materials affect the nature of electronic transport as a function of applied bias. More specifically, we want to know when does the transport of electronic charge carriers becomes migratory, and whether both electrons and holes are involved in the conduction.

In this chapter, several current-voltage experiments will be carried out on single-layer PA_A and PA_C in Au|Ionomer|Au sandwich configuration, with the focus

on answering the following questions that are closely related to the goals of this dissertation:

1. How does current evolve under different bias for each ionomer? Will the two ionomers behave differently?

2. How does the steady-state currents of the two materials change with bias?

3. How does the amount of electronic charge carriers injected into each ionomer changes with applied bias? Will the onset voltages of bipolar injection differ substantially from the results of electrochemical charge injection experiments?

4. What fraction of the applied potential is dropping near the electrode interfaces versus the bulk of the material? And how doses the potential distribution changes with bias?

To answer the first two questions, the current as a function of time under a step bias will be monitored until the system reaches steady-state or near steady-state for both ionomers. The result of this experiment will tell us wether the two materials are indeed similar in their electronic properties despite their apparent difference in ionic conductivity. The amount of injected charge at each applied bias can be estimated by discharging the system from steady-state and integrating the short circuit current. By examining the dependance of the short circuit charge on applied bias, it is possible to infer whether the charge injection is unipolar or bipolar. The steady-state potential distribution of MIEC systems has been investigated by several groups using different methods,[75, 76, 77, 78] but quantitative results are still controversial.[2, 79, 80, 77, 81] The goal of the work in this chapter will be limited to a qualitative estimate of the steady-state potential distribution, and hopefully this goal will be achieved by combining the results from all experiments conducted, including the relaxation of open-circuit potential from steady state.

4.2 Experimental details

4.2.1 Sample preparation

Single layer Au|Ionomer|Au samples were prepared and annealed in the same way as described in the experimental details section in Chapter-II.

4.2.2 Electrical measurements

Three types of electrical measurements – current under bias, short-circuit current, and open-circuit potential, are involved in this chapter. A Keithley 236 Source-Measure Unit in combination with a Keithley 7001 switching matrix was used for all three types of measurements. A custom labview program was used for controlling the instruments and recording data. All measurements were done in actively pumped vacuum (20 mTorr) except the experiment that involves acetonitrile vapor.

A typical experiment starts from applying a bias to the Au|Ionomer|Au sample and measuring the current as a function of time, $I_B(t)$, until the system reaches or nears steady-state, then the instrument is switched to either measuring the short-circuit current as a function of time, $I_{SC}(t)$, or measuring the open-circuit potential as a function of time, $V_{OC}(t)$, during the relaxation of the system from steady-state. During the transition between different measurements, the system is switched into open circuit for a brief moment (<1 ms) as needed for switching the function of Keithley 236. After each open-circuit measurement, the system is left at short-circuit until the sample is fully relaxed as indicated by the leveling off of the short-circuit current.

4.3 Results and discussion

In presenting the experimental results throughout this chapter,"steady-state" refers to the state of the device at the end of a typical 90 minute (unless indicated

otherwise) bias at various applied voltages. It was found that after applying a bias for 90 minutes, PA_C samples are sufficiently close to steady-state while slow changes in PA_A samples still persist as will be shown later. However, the results of longer bias times (up to 4 hours) for PA_A indicates that the small changes after 90 minutes are not significant, and therefore not recorded for most measurements.

4.3.1 The change of current under stepping bias

The change in the overall current of the Au|Ionomer|Au structure in response to constant applied biases in the range of 0.1V to 1.5V are plotted as a function of time in log-long scale in Fig-4.1, for a PA_A sample (top graph) of 560 nm and a PA_C sample (bottom graph) of 210nm. The result of a repeated measurement on the PA_C sample is also shown to highlight the consistency between measurements after the sample was stabilized.

From Fig-4.1, it can be seen that for the PA_A sample, current evolves much slower than that of the PA_C sample. The slower response of the PA_A sample is not surprising since the redistribution of ions in PA_A is much slower than in PA_C, due to the lower ion conductivity and larger thickness of the PA_A sample, according to the results from the impedance measurements in Chapter-II. Other than the apparent difference in response time, the overall $I_B(t)$ of the two materials are quite similar.

Throughout the entire range of applied bias, two regions of applied bias can be identified by the way $I_B(t)$ changes with time. The first bias region is characterized by an initial current that is higher than the near steady-state current, while the second bias region is characterized by a near steady-state current that is higher than the initial current. The transition between the two bias regions, as can be identified from Fig-4.1, is around $V_B=0.5V$ for PA_A and $V_B=0.7V$ for PA_C.

A common feature for all $I_B(t)$ curves in Fig-4.1 is that there is an initial decay of current immediately after a bias is applied. After the initial decay, the change in $I_B(t)$ is voltage dependent. At the transitional voltage of each sample, the current
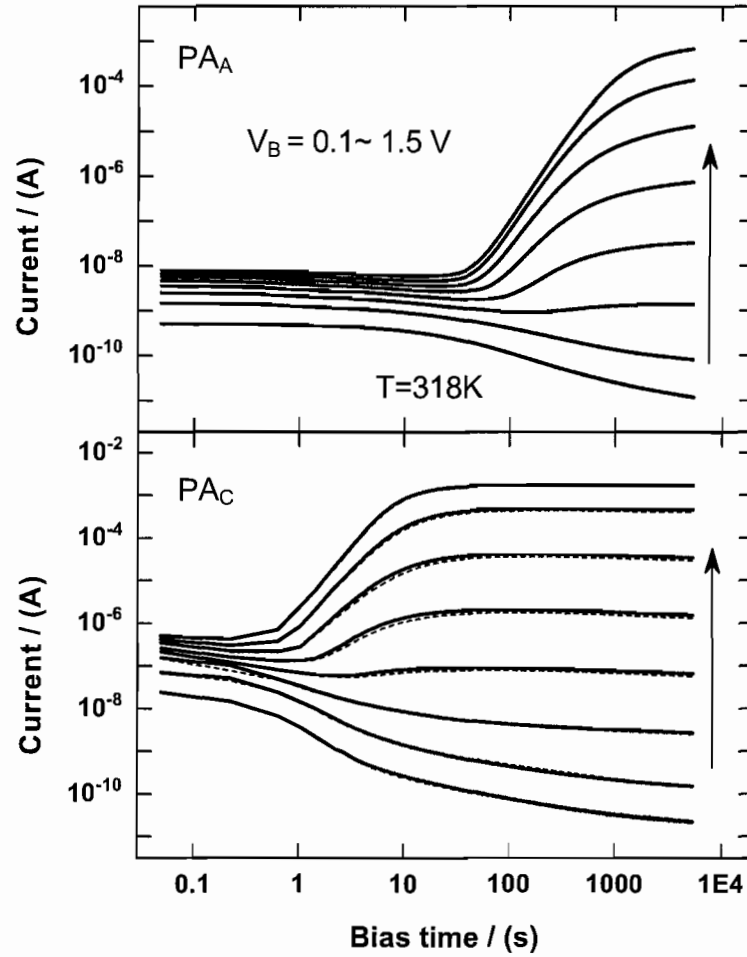
FIGURE 4.1: The response of device current to constant applied biases, recorded as a function of time over 1.5 hours, for PA_A (Top) and PA_C (Bottom). The range of applied voltage is from 0.1 V to 1.5 V, in 0.2V increments. The dashed lines in the bottom graph are results of a repeated measurement on the same PA_C sample.

rises slightly before leveling off, while at biases lower than the transitional voltage, the current decays monotonically. For biases higher than the transitional voltage, the current keeping rising until leveling off at a higher value.

The common feature and bias dependent features in $I_B(t)$ can be understood in terms of two sequential stages of the device response. During the first stage, the current is dominated by ions moving in response to the applied electric field, and the ion-blocking electrodes result in an initial decay of current as ionic double layers are formed near the electrode surfaces while few electronic charge carriers are present. The difference in the duration of this initial decay and in the initial value of $I_B(t)$ between PA_A and PA_C is consistent with the fact that PA_A has a much lower ion conductivity than PA_C at the same temperature. Furthermore, the initial values of $I_B(t)$ for both ionomers show a close to linear dependence on the applied bias, as can be seen from Fig-4.2. The conductivities extracted through a linear fit of $I_B(0)$ versus V_B yielded $\sigma \approx 5.7 \times 10^{-11}$ S/cm for the PA_C sample, and $\sigma \approx 2.5 \times 10^{-12}$ S/cm for the PA_A sample. Both conductivity values are reasonably close to the ionic conductivity results obtained from impedance experiments – 3×10^{-11} S/cm for PA_C and 3×10^{-12} S/cm for PA_A at 318 K.

The second stage of device response is dependent on applied voltage. At low bias voltages, the injected electronic charge were limited by the unipolar nature of the injection, as suggested by the results of the electrochemical injection experiment in Chapter-III. Therefore, the current keeps decaying monotonically until steady-state. At biases higher than the transitional voltage, however, an increased amount of injected electronic charge carriers resulted in a substantial increase in the electronic current that eventually surpassed the initial ionic current. As the amount of injected electronic charge increased, the redistribution of compensating ions also contributed to the overall current. The overall current leveled off only when the maximum amount of electronic charge possible at each bias were injected and the corresponding redistribution of ions was completed.
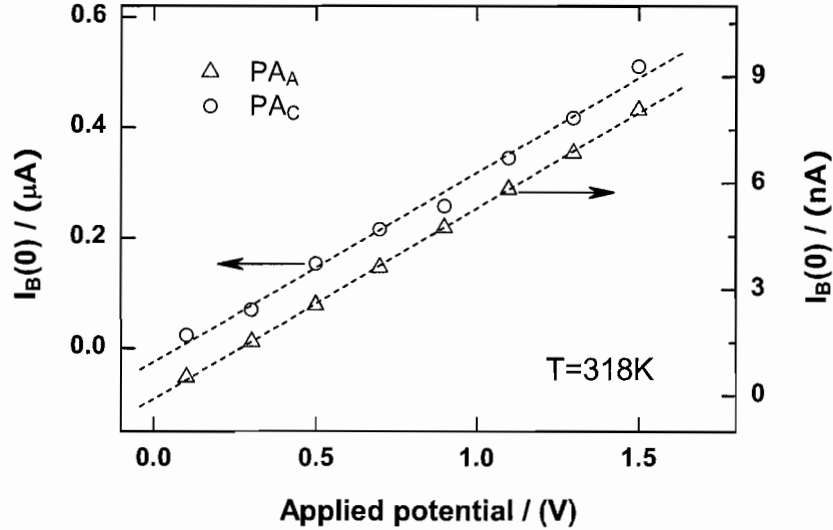
FIGURE 4.2: The initial current of a PA_A sample (open triangles, right ordinate) and a PA_C sample (open circles, left ordinate) as a function of applied bias. The dashed lines are linear fits to their corresponding set of data points.

4.3.2 The effect of bias time

It is seen in Fig-4.1 that the $I_B(t)$ of the PA_A sample took longer to reach steady-state. In an effort to determine whether the PA_A sample is close to steady-state at the end of a 90 minute bias, another quantity of interest, the initial value of the open-circuit potential $V_{OC}(0)$, was measured for V_B=1.5V as a function of the duration of applied bias (see Fig-4.3). The $V_{OC}(0)$ data points are represented by solid squares in Fig-4.3, and their corresponding bias times are indicated by open squares on a 90 minute $I_B(t)$ curve.

As can be seen from Fig-4.3, the value of $V_{OC}(0)$ increases to about 0.46 V during the ionic double layer charging stage, then decreases to about 0.4 V when $I_B(t)$ begins to rise and increases slightly before leveling off at around 0.44 V when the current also begin to level off. Biasing the PA_A sample for longer durations (up to 4 hours) resulted in a $I_B(t)$ curve much like that of the PA_C shown in Fig-4.1 and insignificantly small changes in both current and $V_{OC}(0)$.
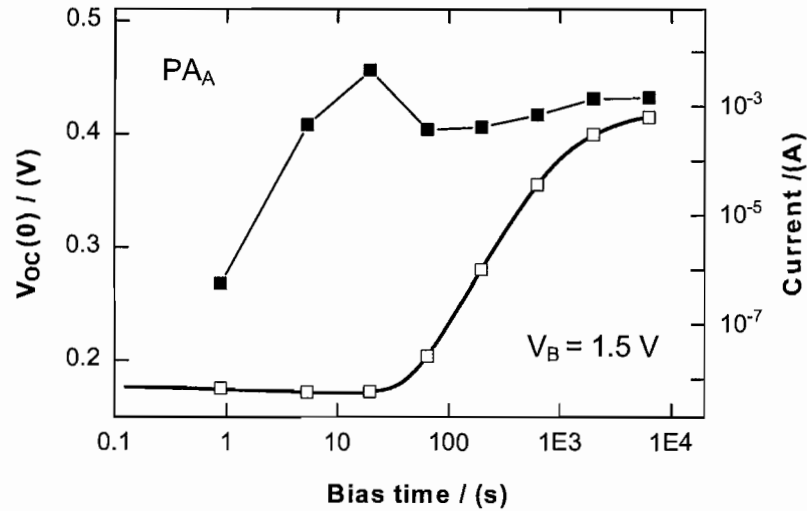
FIGURE 4.3: The change in the initial open-circuit voltage $V_{OC}(0)$ as a function of bias time at V_B=1.5 V, for a PA_A sample at T=318K. The solid squares are data points of $V_{OC}(0)$ recorded after different bias time, and their position on a continuous $I_B(t)$ curve (solid line with open squares) are indicated by open squares. The sample was adequately relaxed through short-circuit after each measurement of $V_{OC}(0)$.

4.3.3 Stabilization of the sample

Repeated measurements on the same sample reveals a reproducible difference between the I-V response of the first set of complete bias range measurements and the subsequent sets of measurements, as evidenced by the difference in steady-state currents shown in Fig-4.4. After the first set of measurements, the results became very consistent among subsequent measurements. The difference between first and second set of measurements is more apparent in the low bias regime. The origin of this change is not yet fully understood. It is possible that both the bulk of the ionomer and their interfaces with electrodes undergo some changes during the first set of measurement, then stabilize afterwards.

4.3.4 Steady-state current

The steady-state currents measured by the final value of $I_B(t)$ at the end of a 90-minute bias as a function of applied potential are shown in Fig-4.5 for a PA_A
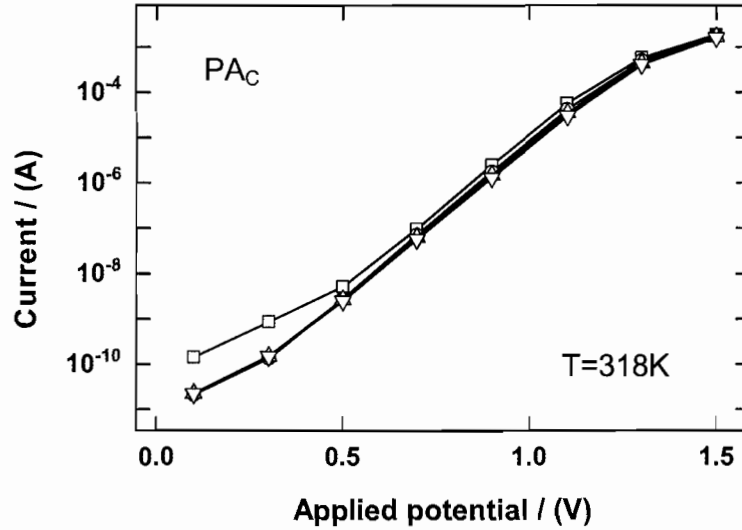
FIGURE 4.4: The history effect of a typical PA_C sample. Open squares represent the near steady-state currents of the first measurement from $V_B=0.1V$ to $V_B=1.5V$, the data points of three subsequent measurements on the same sample are represented by open circles, and open triangles. A 90 minutes bias time was used for all measurements.

sample and a PA_C sample. It can be seen that, aside from a normalization factor likely due to difference in thickness, the bias dependence of the steady-state current is essentially the same for both ionomers. An exponential increase of I_{SS} with bias can be seen within the bias range of 0.5 V to 1.1 V. Outside of this exponential region the steady-state current appears to change slower with the applied bias.

The similarity of the bias dependance of I_{SS} between the two ionomers is consistent with the findings from Chapter-III, which indicates that both ionomers have similar onset voltages of unipolar and bipolar injection, and that holes are the dominant electronic charge carriers for both materials.

The temperature dependance of the steady-state current was not pursued extensively due to the concern that passing a current in the mA range for hours when the sample is at elevated temperature would cause irreversible damage to the sample, while lowering the temperature increases the experiment time substantially.
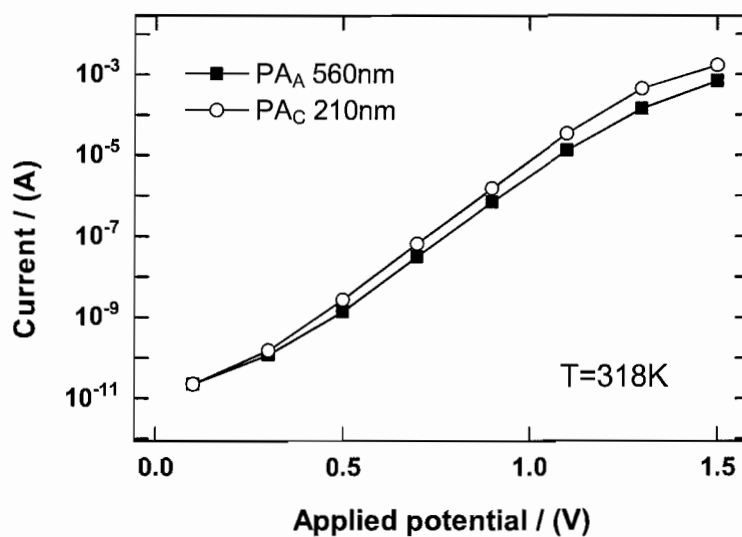
FIGURE 4.5: The steady-state current as a function of applied bias for a PA_A sample of 560 nm (solid squares), and a PA_C sample of 210 nm (open squares).
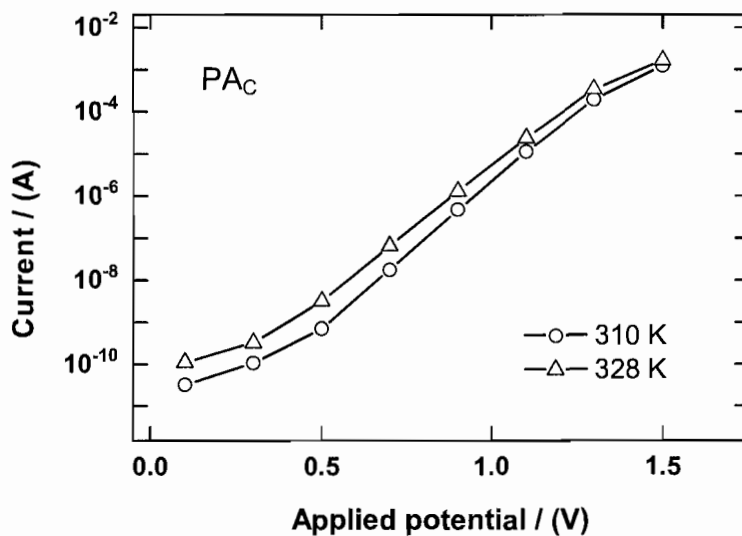
FIGURE 4.6: The steady-state current as a function of applied bias for a PA_C sample of 280 nm at T=310 K (open circles), and at T=328 K (open triangles). Lines are added to guide the eye.

Nevertheless, a PA_C sample was tested at both 328 K and 310 K to demonstrate the effect of varying temperature, and the results are shown in Fig-4.6. It was found that the steady-state current increases with the increase of temperature, and the steady-state current at lower biases appears to increase more significantly than the steady-state current at higher biases while the bias dependance seemed unchanged.

4.3.5 Discharging through internal pathway

Since both ionomers' electronic conductivity increase substantially with applied bias, a portion of the injected charge will inevitably recombine internally through the material, therefore the amount of charge collected through the external short-circuit will represent only part of the total amount of charge accumulated throughout the device.

An estimate of how much electronic charge recombines through the internal pathway can be obtained by comparing the total charge collected through two different methods of discharging the device. In the first method, the device is discharged through short-circuiting immediately after the applied bias is removed, while in the the second method the device is left in open-circuit for a certain amount of time after the applied bias is removed, then discharged through short-circuiting. The difference between the total charge collected via the second method and that collected via the first method provides an estimate of the amount of charge that are forced to recombined internally during the time of open-circuiting.

Based on the observation from Fig-4.8 that, during a typical short-circuit measurement most of the charge were collected during the first couple of minutes, a 10-minute open-circuit time was used for such an experiments on a PA_A sample. The results are plotted out in Fig-4.7 as the ratio between the amount of charge collected with and without a 10-minute open-circuiting. It can be seen that as the applied bias increases, more charge recombine internally during the 10 minutes in open-circuit state. Due to the fact that electronic charge carriers are forced to recombine
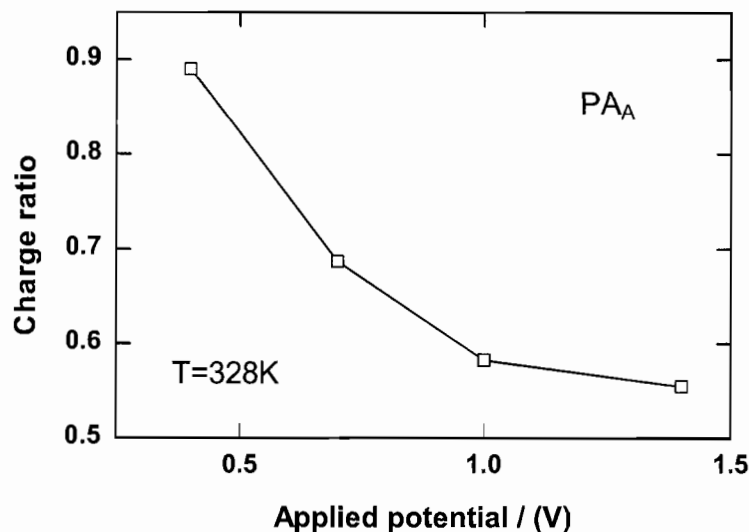
FIGURE 4.7: The ratio between the short-circuit charge collected after open-circuiting a PA_A sample for 10 minutes from steady-state to chat collected immediately after the bias is removed, as a function of applied bias.

internally while the device is in open-circuit, it is expected that in an immediate short-circuit experiment, the amount of charge carriers that recombine internally would be substantially less than what's indicated by the results in Fig-4.7, due to the much lower impedance of the external circuit. Therefore the charge collected through immediate short-circuiting is likely to be more than 60% of total the accumulated charge for $V_B > 1.0V$, and close to 100% for lower biases.

4.3.6 Short-circuit discharging from steady-state

To estimate the amount of electronic charge carriers that are injected into the ionomer at each applied bias, short-circuit discharging experiments were carried out on samples of both ionomers. Typical discharging curves are shown in Fig-4.8 for samples of both ionomers. It can be seen that, other than a difference in the time scale, the discharging curves of the two ionomers are very similar in appearance at comparable bias. For both materials, the discharging current increases with

increasing bias. In the log-log scale, a relatively flat region during the initial phase of discharging seemed to persist longer as the bias was increased, and this relative flat region then give way to a more rapid decrease as the discharging process continues. The transition between these two regions happened at an earlier time for PA_C.
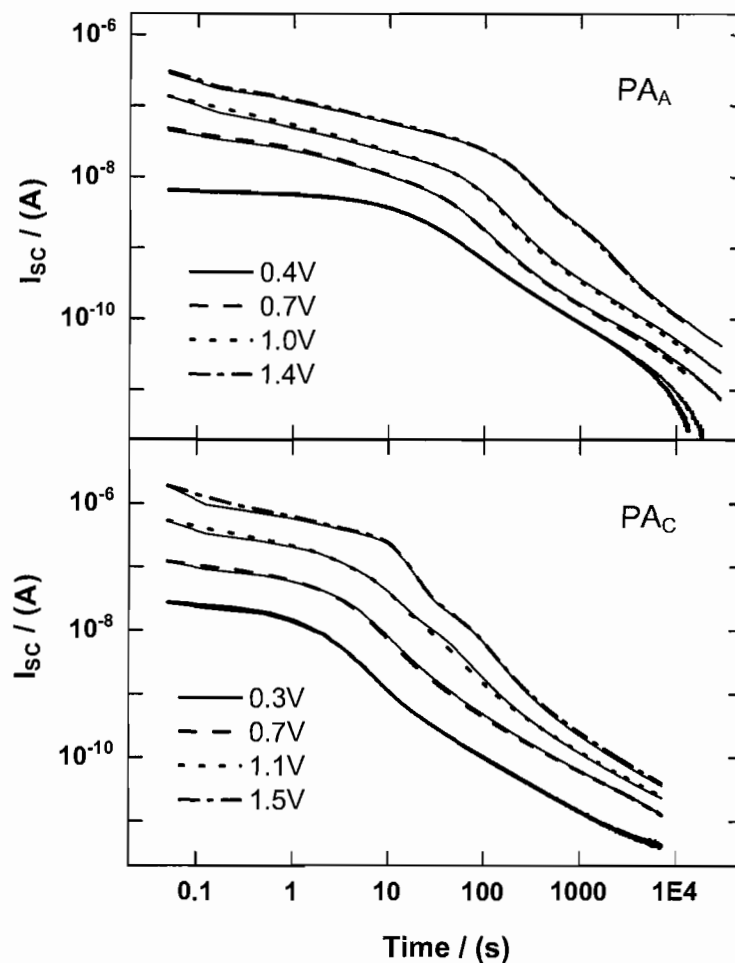
FIGURE 4.8: The change of short-circuit current after various biases, as a function of time for a PA_A sample (Top) at T=328K, and a PA_C sample (Bottom) at T=318K. Results of two repeated measurements are shown together for each sample.

The similarity in appearance and the difference in time scale of the discharging curves between PA_A samples and PA_C samples indicates that the discharging processes for both ionomers are reflective of the motion of ions, as would be predicted

by the coupling between the electronic and ionic charge carriers in mix-conducting materials and the lower mobility of ions compared to holes. The increase in length of the initial slow decaying region with the increase of bias could be explained by assuming that, at higher biases more electronic charge carriers are injected into the ionomer resulting in a more significant redistribution of ions in the material, therefore during the discharging, the reversal of this ion redistribution takes longer to complete.

The amount of charge collected through immediate short-circuiting experiments at each bias are shown in Fig-4.9 for a PA_A sample (solid circles) at T=328K, and a PA_C sample at T=328 K (open circles) and T=310 K (open triangles). The PA_C data in Fig-4.9 have been corrected for a persisting baseline current of $\sim 4 \times 10^{-12}$ Ampere for T=310 K and $\sim 1 \times 10^{-11}$ Ampere at T=328K. The correction has a significant effect on only the first data point of V_B=0.1 V. The theoretical values of charging a 4 $\mu F/cm^2$ double layer of the same area as the sample was shown by the dashed line for comparison.

One may first notice from Fig-4.9 that, for V_B>0.4V, the collected short-circuit charge for both ionomers and at both temperatures are substantially higher than that of charging an ionic double layer, and the difference increases quickly as the bias increases. It can seen that more charge were collected from the 560 nm PA_A sample than the 280 nm PA_C sample at T=328 K except for the less trustworthy lowest bias due to baseline correction. For the PA_C sample, the total charge collected through short-circuit appears to increase with temperature for biases lower than 1.1 V, then the difference disappears at higher biases. For biases higher than 1.1 V, the increase in short-circuit charge for all tree sets of data appears to be exponential.

The fact that the total short circuit charge for both ionomers at V_B>1.1 V are substantially higher than (>4 times) the value of ionic double layer charging, and that more charge was collected from the thicker 560 nm PA_A sample than the 280 nm PA_C sample indicates that electronic charge injection at biases higher than 1.1 V was bipolar. A transition from unipolar to bipolar injection would also be consistent
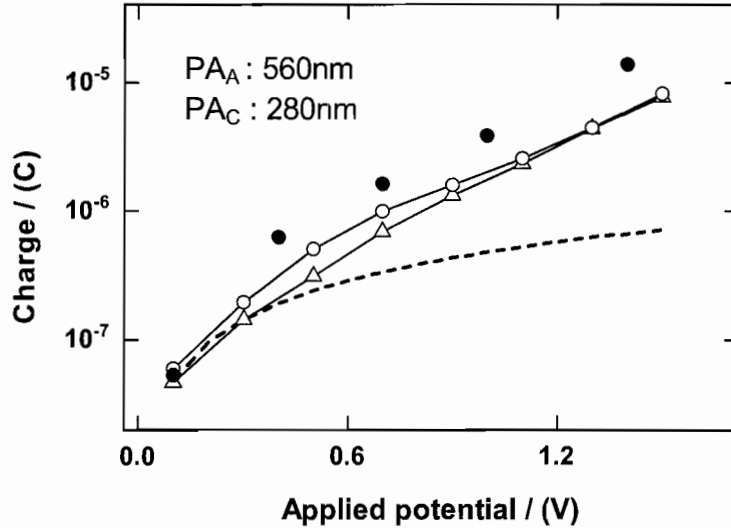
FIGURE 4.9: Charge collected through short-circuit relaxation of a PA_A sample (solid circles) at T=328K, and a PA_C sample at T=328 K (open circles) and T=310 K (open triangles), as a function of applied bias. The data points for PA_C are connected with lines to guide the eye. The dashed line represents the theoretical values of charging a 4 $\mu F/cm^2$ double layer of the same area as the sample.

with the observation that the difference in short-circuit charge between T=310 K and T=328 K for the PA_A sample diminishes at biases higher than 1.1 V, since in the regime of bipolar injection, the amount of charge that the material can accept is largely determined by the volume of the material and the availability of charge compensating ions at a given bias. In contrast, for biases lower than 1.1 V the amount of injected charge depends on the low frequency ionic double layer capacitance of the material, which can change more significantly with temperature as shown by the results from temperature dependent impedance study in Chapter-II. At 328 K, the increased amount of injected charge in the low bias regime could have contributed to the more significant increase of steady-state current in the low bias regime than in the higher bias regime that was observed in Fig-4.6.

Notably, the transitional voltage of 1.1 V as indicated by the PA_C data in Fig-4.9 is not far from the onset voltage of 0.9 V for bipolar injection that was found in

Chapter-III through the electrochemical charge injection experiment. In solid state, it is not surprising that a higher voltage is necessary to drive bipolar injection than in an electrolyte due to the difference in ionic environment. The short-circuit charge collected at $V_B=1.5$ V for either Au|Ionomer|Au sample is substantially less than the injected charge estimated from the charge transfer current during the symmetric electrochemical cell experiment in Chapter-III, at same applied voltage. Part of the difference might be accounted by the fact that not all injected charge are recovered through short-circuit. This differnece could also suggest that the charge injection in the solid state is limited by the availability of compensating ions.
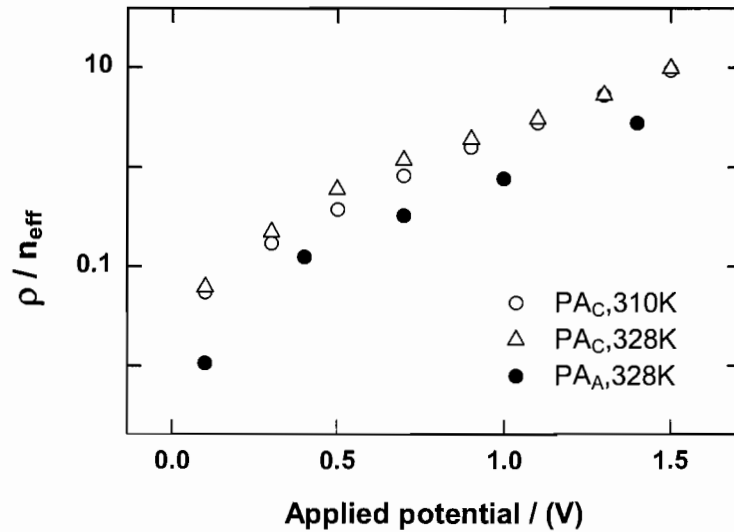
FIGURE 4.10: The ratio between injected electronic charge density and effective mobile ion density, as a function of applied bias, for a PA$_A$ sample with $n_{eff} = 4.5\times10^{18}$ /cm^3 and a PA$_C$ sample with $n_{eff} = 1.5\times10^{18}$ /cm^3.

As a measure of how much electronic charge carriers was injected at each bias, the amount of short-circuit charge are compared to the effective ion densities that were estimated through impedance experiments in Chapter-II. The results are shown in Fig-4.10 in terms of the ratio between the apparent electronic carrier density $\rho_{app} = Q_{SC}/v$ and the effective mobile ion density n_{eff}, where v is the volume of the ionomer film. The fact that this ratio exceeds 1 for biases higher than 1 Volt for both

ionomers and reaches 10 at $V_B=1.5V$ for PA_C suggests that the effective mobile ion densities were likely underestimated, and/or part of the short-circuit charge are not compensated by ions.
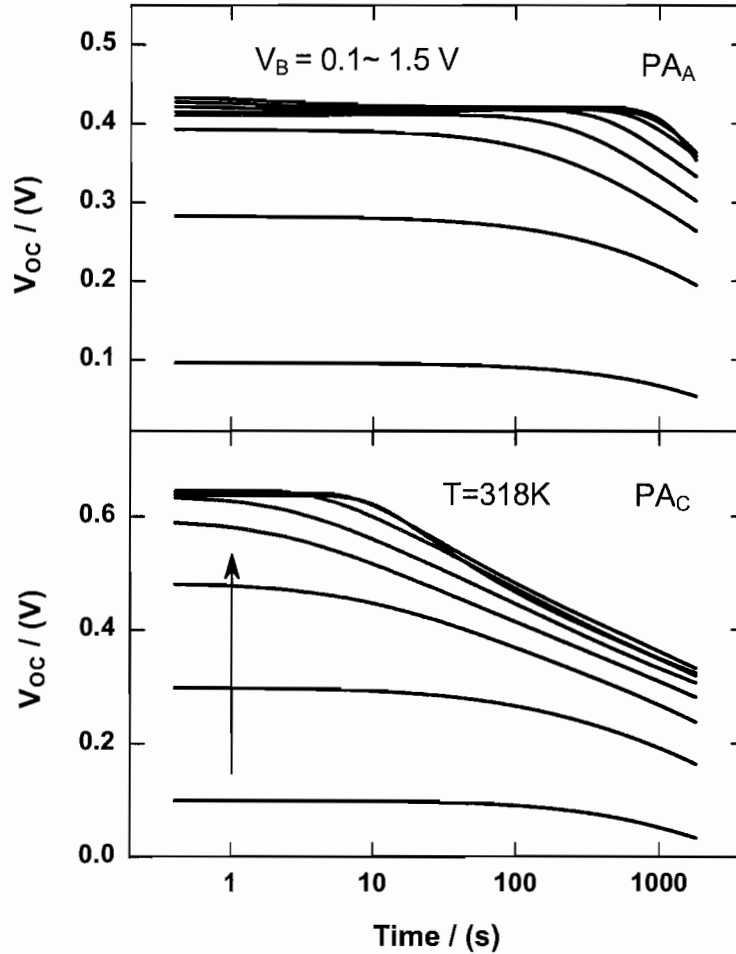
FIGURE 4.11: The change of open-circuit potential as a function of time for a PA_A sample and a PA_C sample during the open-circuit relaxation from steady-state of various biases.

4.3.7 Open-circuit relaxation from steady-state

The change of open-circuit potential with time, $V_{OC}(t)$, while the sample relaxes from steady-state at each bias is shown in Fig-4.11 for a PA_A sample (top) and a

PA$_C$ sample (bottom) within the bias range of 0.1 V to 1.5 V in 0.2 V increments. Again, apart from a difference in time and magnitude scale in the higher bias regime, the V_{OC}(t) of the two ionomers show similar features. The longer time scale needed for the relaxation of PA$_A$ is a reflection of its lower ionic conductivity as compared to PA$_C$. The initial value of the open-circuit potential, $V_{OC}(0)$, first increases with bias for both ionomers, then approaches a limiting value of around 0.43 V for PA$_A$ and 0.65 V for PA$_C$ as bias further increases. The applied voltage at which this leveling off of $V_{OC}(0)$ occurs is V_B=0.5 V for PA$_A$ and V_B=0.7 V for PA$_C$. The change in $V_{OC}(0)$ as a function of bias can be better seen in Fig-4.12.
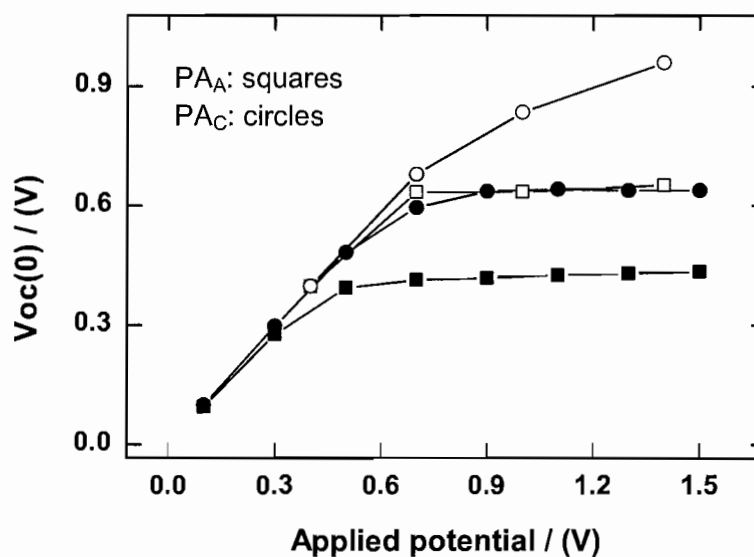
FIGURE 4.12: The initial value of open-circuit potential as a function of applied bias for a PA$_A$ sample (squares) and a PA$_C$ sample (circles), in vacuum after annealing (solid symbols) and at the presence of acetonitrile vapor (open symbols).

Interestingly, the applied voltage of 0.5 V for PA$_A$ and 0.7 V for PA$_C$ at which $V_{OC}(0)$ starts to level off coincides with the transitional voltages that were described earlier to separate the change of I_B(t) (in Fig-4.1) into two bias regimes. This coincidence suggests that as soon as the electronic conductivity surpasses the ionic conductivity, the value of $V_{OC}(0)$ starts to level off as bias further increases.

The $V_{OC}(0)$ data in Fig-4.12 shows that for applied biases higher than 0.7 V, there is a substantial difference between the applied bias and the initial value of V_{OC}. The origin of this difference and its implications will be discussed later.

4.3.8 The effect of acetonitrile vapor

In Chapter-II, it was shown that exposing the Au|Ionomer|Au sample to acetonitrile vapor could increase the ionic conductivity of the sample by several orders of magnitude. To investigate the effect of ion mobility on the current-voltage response of the Au|Ionomer|Au system, several experiments in this chapter were also carried out in the presence of acetonitrile vapor at T=310 K to be compared with the results obtained after the samples have been dried in vacuum.
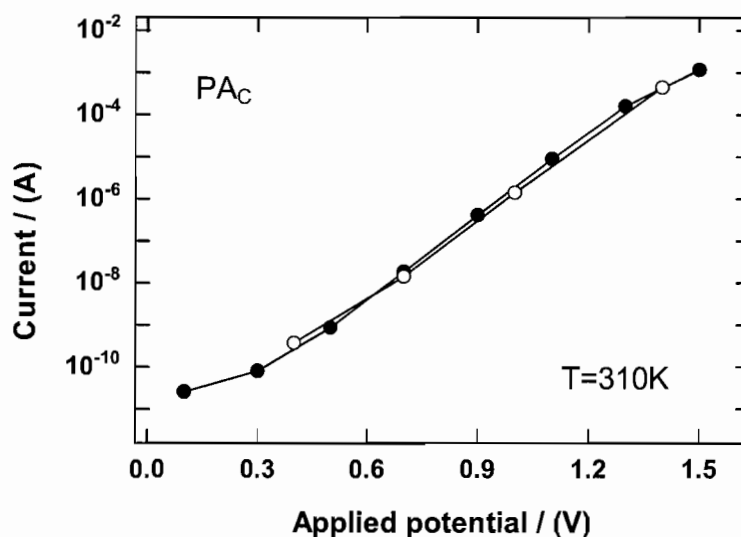
FIGURE 4.13: The steady-state current at various biases of a PA_C sample in vacuum after annealing (solid circles) and in the presence of acetonitrile vapor (open circles).

The effect of acetonitrile vapor on the steady-state current of a PA_C sample is shown in Fig-4.13. Other than increasing the ionic conductivity of the material, and hence the speed of the sample's response to bias, acetonitrile vapor seemed to have no significant effect on the electronic current at steady-state.
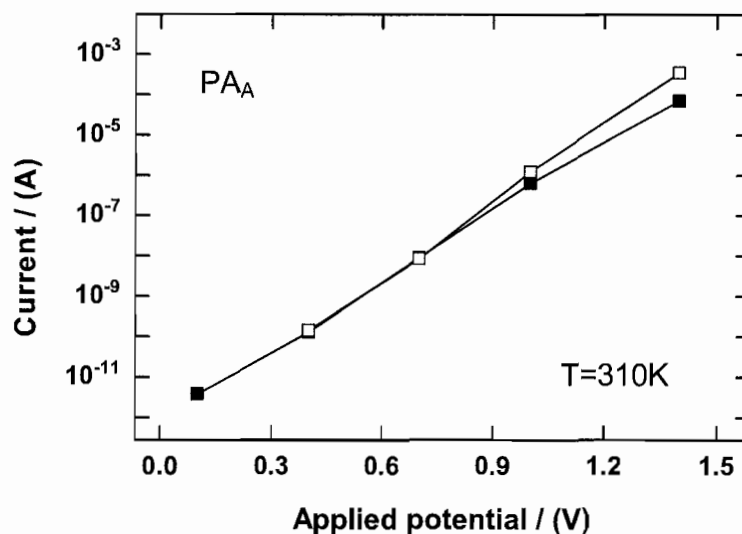
FIGURE 4.14: The steady-state current at four different biases of a PA_A sample in vacuum after annealing (solid squares) and in the presence of acetonitrile vapor (open squares).

From Fig-4.14, the presence of acetonitrile vapor seemed to increase the steady-state current of the PA_A sample more significantly at $V_B=1.4$ V, but a comparison of $I_B(t)$ in Fig-4.15 reveals that the difference was largely due to the fact that, for the data collected when the sample was in vacuum, steady-state was not yet achieved at the end of the measurement.

The effect of acetonitrile vapor on the bias dependence of $V_{OC}(0)$ is more dramatic as can be seen in Fig-4.12. Exposure to acetonitrile vapor increases the limiting $V_{OC}(0)$ of the PA_A sample from ≈ 0.43 V to ≈ 0.65 V, while the limiting $V_{OC}(0)$ of the PA_C sample was increased from ≈ 0.63 V to higher than 0.95 V.

The absence of significant change in steady-state current in the presence of acetonitrile vapor suggest that the solvent vapor has little effect on the electronic conductivity of both ionomers. The change in $V_{OC}(0)$ due to acetonitrile vapor indicates that the measured open-circuit potential and the ionic conductivity are closely related. The effect of solvent vapor on $V_{OC}(0)$ will be further discussed later.
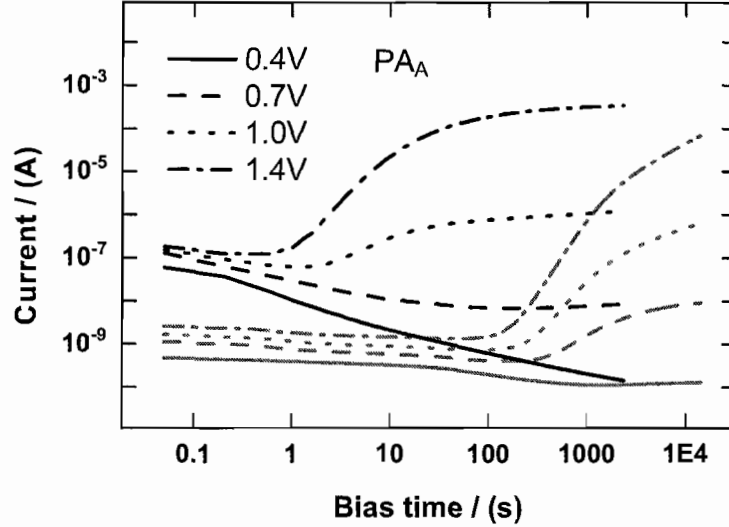
FIGURE 4.15: The change of current under four different applied biases of a PA$_A$ sample in vacuum after annealing (gray lines) and in the presence of acetonitrile vapor (black lines).

4.3.9 The measured V_{OC} value during relaxation

Ideally the open-circuit potential measured by a voltmeter is a reflection of the electromotive force, $\mathscr{E}$, of a power source. In a real experiment, however, the measurement of open-circuit potential always relies on the discharging of the system and therefore the internal resistance of the power source R_{PS} have to be considered. When the internal resistance of the power source is comparable to the external measuring circuit, the measured terminal voltage V_M will be lower than the true $\mathscr{E}$. If the voltmeter's resistance is R_M, then the measured voltage can be related to the electromotive force by:

$$V_M = \mathscr{E} \frac{R_M}{R_M + R_{PS}} \tag{4.1}$$

During the open-circuit potential measurement of the Au|Ionomer|Au system, the electromotive force is provided by the electrical energy stored in the sample through the accumulation of separated electronic charge carriers. Depending on the bias range and mobile ion concentration, these separated electronic charge carriers may

be completely or partially coupled to the polarization of mobile ions. An open-circuit voltage can be measured when these separated electronic charge carriers recombine through internal or external pathways. In the absence of electronic conductivity within the ionomer, the Au|Ionomer|Au system is in effect an electrolytic capacitor (or battery), and the accumulated electronic charge carriers have to recombine through the external pathway, i.e. the voltmeter. Therefore the internal resistance of the sample is determined by the relaxation of the ionic polarization within the material, which usually has a much lower impedance than that of a high quality voltmeter $(R_M > 10^{14}\Omega)$. Hence $V_M \approx \mathscr{E}_i^o = \mathscr{E}$.

However, in cases such as polyacetylene ionomers the electronic conductivity of the material is non-zero, therefore the separated electronic charge carriers can recombine internally, and usually the internal electronic resistance R_{el} is less than R_M, then the resistance of the measuring circuit is in effect the parallel combination of R_{el} and R_M, which may become comparable or smaller than the resistance of ionic relaxation in the material. In such cases, if $R_{el} \ll R_M$ and the electromotive force is supplied by those electronic charge carriers that are coupled to mobile ions, then the R_{PS} in Eq. (4.1) is determined by the ionic resistance R_{ion} and Eq. (4.1) becomes:

$$V_M = \mathscr{E}_i^o / \left(1 + \frac{R_{ion}}{R_{el}} \right) \tag{4.2}$$

The corresponding equivalent circuit of Eq. (4.2) is shown in Fig-4.16.
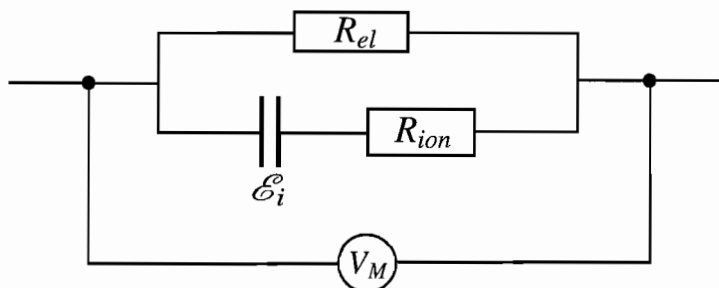
FIGURE 4.16: The equivalent circuit of an open-circuit potential measurement on a mix-conducting system according to Eq. (4.2).

The time constant for the relaxation of the ionically coupled electromotive force, $\mathscr{E}_i$, is determined by the differential (Faradaic or interfacial) capacitance and the ionic or electronic resistance, whichever is larger. Since the lower limit of Faradaic or interfacial capacitance is usually on the order of 10^{-6} F, and the typical ionic resistance for a 300nm PA_C sample is on the order of 10^6 Ω, the relaxation time is usually on the order of seconds.

When sufficiently high bias is applied to the Au|Ionomer|Au system such that the mobile ionic charge carriers are not able to completely screen the electric field in the bulk of the material. Then part of the electromotive force during the open-circuit relaxation will be provided by those accumulated electronic charge carriers that are not coupled to mobile ions, i.e. $\mathscr{E} = V_B = \mathscr{E}_i + \mathscr{E}_e$. The recombination of these charge carriers during the open-circuit relaxation will be much faster than those ionically coupled charge carriers, since their corresponding internal resistance as well as their differential capacitance are much lower. Assuming that the internal resistance is on the order of 10^3 Ω and the differential capacitance is on the order of geometric capacitance $\sim 10^{-8}$ F, the relaxation time for $\mathscr{E}_e$ is on the order of 10^{-5} seconds.

The difference in relaxation times between $\mathscr{E}_e$ and $\mathscr{E}_i$ can in principle be used to identify the bias level above which an electric field exists in the bulk of the material, through the deviation of the initial value of $\mathscr{E}_i$ from the applied bias V_B. When the Au|Ionomer|Au system is relaxed in open-circuit from steady-state, the initial value of V_{OC} is reflective of only the $\mathscr{E}_i$ due to the $\sim ms$ range response time of the instrument setup. However, an accurate calculation of the true initial value of $\mathscr{E}_i$ is difficult since the internal electronic resistance is changing with time, thus its value at the moment when $V_{OC}(0)$ is measured is difficult to determined. Nevertheless, the V_{OC} data for both ionomers can still be qualitatively explained through Eq. (4.2).

In the low bias regime the Au|Ionomer|Au system is in effect a double layer capacitor, all accumulated electronic charge carriers are coupled to ions and the electronic conductivity is lower than the ionic conductivity as indicated by $I_{SS} < I_B(0)$.

For $V_B \leq 0.3$ V, the steady-state (electronic) current I_{SS} of both ionomers are much lower than the corresponding ionic current $I_B(0)$, therefore $V_{OC}(0) \approx \mathscr{E}_i^o = V_B$ as can be seen from Fig-4.12. The relaxation time of $V_{OC}(t)$ is then determined by the ionic double layer capacitance and the electronic conductivity of the ionomer. Since the two ionomers have comparable ionic double layer capacitance as well as electronic conductivity at the same bias, the $V_{OC}(t)$ curves at $V_B \leq 0.3$ V in Fig-4.11 are very similar for both ionomer samples. The higher ionic conductivity of PA_C makes it's electronic conductivity at $V_B = 0.5$ V also relatively small, thus for the PA_C sample at $V_B = 0.5$ V the initial value of the open-circuit potential was also very close to the applied bias.

As the applied bias further increases, the electronic conductivity approaches and then surpasses the ionic conductivity when $V_B \geq 0.7$ V for PA_C and $V_B \geq 0.5$ V for PA_A. Consequently the $V_{OC}(0)$ for higher biases deviates substantially from the applied bias according to Eq. (4.2). Since the ionic conductivity is now the limiting factor of the system's relaxation, the time constant for the relaxation of V_{OC} is determined by the ionic conductivity and the sample's capacitance. The $V_{OC}(t)$ curves in Fig-4.11 for $V_B > 0.7$ V indeed show that the decay of V_{OC} for the PA_C sample is faster than that of the PA_A sample.

Exposing the dried sample to acetonitrile vapor leads to a substantial increase in the ionic conductivity for both ionomers but cause little change to their electronic conductivity. Hence, the relationship of $V_{OC}(0) \approx V_B$ persisted to higher biases for both ionomers.

Although the exact values of $\mathscr{E}_i(0)$ for biases that resulted in a substantial electronic conductivity increase can not be calculated from the $V_{OC}(0)$ data due to the unknown value of $R_{el}(0)$, and hence the voltage at which the transport of electronic charge carriers become migratory can not be identified. The fact that the maximum $V_{OC}(0)$ for the PA_C samples approached 1 V at $V_B = 1.5$ V and the fact that steady-state electronic conductivity was much higher than ionic conductivity at

V_B=1.5 V strongly suggests that the bulk of the material is free of an electric field within the bias range of 0.1 V to 1.5 V.

4.4 Summary

In this chapter, electrical measurements were carried out on single-layer PA_A and PA_C samples to investigate the bias dependence of each material's electronic conductivity and the amount of injected charge in solid state, as well as to demonstrate the effect of the ionic environment on the electrical response of the mix-conducting ionomer.

It is found that the electronic conductivity of PA_A and PA_C exhibit a similar strong dependance on the applied bias, while the evolution of each Au|Ionomer|Au system's conductivity under bias was strongly affected by the ionic conductivity of the corresponding ionomer. Within the bias range of 0.1 V to 1.5 V, the steady-state electronic current of both ionomers changed by eight orders of magnitude from $\sim$ 10^{-11} Ampere at 0.1 V to $\sim 10^{-3}$ Ampere at 1.5 V. And the response of PA_A samples to applied bias was slower than PA_C samples due to the lower ionic conductivity of PA_A. The electronic conductivity of PA_C was found to increase as temperature increases.

The amount of injected electronic charge carrier for both ionomers are also found to be strongly dependent on applied bias. At biases higher than 0.4 V, the amount of injected charge for both ionomers was found to be greater than what would be predicted by their ionic double layer capacitances obtained through small amplitude impedance spectroscopy. Above 1.0 V, the apparent density of the injected charge for both ionomers became higher than the estimated effective mobile ion density of $\sim 3 \times 10^{18}/\text{cm}^3$.

Exposing dried ionomer samples to acetonitrile vapor greatly increases the ionic conductivity and hence the response speed of both materials, while the steady-state electronic conductivities of both ionomers were not significantly changed. The results

of open-circuit relaxation experiments strongly indicate that within the bias range of 0.1 V to 1.5 V, mobile ions in PA_C were able to completely screen the applied electric field, and therefore the potential drop in the bulk of the sample was negligible. Further experiments with improved design are necessary in order to identify the voltage at which the electronic transport becomes migratory.

The large amount of injected charge for $V_B>1.0$ V compared to the estimated effective mobile ion density and the diffusive electronic charge transport indicated by the result of open-circuit experiment both suggest that the effective ion densities for PA_A and PA_C were most likely underestimated by the simple ionic double layer model in Chapter-II.

CHAPTER V

ELECTRICAL CHARACTERIZATION OF THE POLYACETYLENE HETERO-IONIC JUNCTION

In this chapter, the responses of the $Au|PA_A|PA_C|Au$ junction to stepping bias and to a small amplitude AC voltage signal are investigated to understand the origin of the junction's asymmetric I-V response. A working mechanism of the $Au|PA_A|PA_C|Au$ junction is then proposed base on the experimental results.

5.1 Introduction

The previous chapters have been largely focused on characterizing the ionic and electronic properties of the two ionomers that were used to construct the $Au|PA_A|PA_C|Au$ junction. The results from experiments in these chapters provided important information about each constituent ionomer of the $Au|PA_A|PA_C|Au$ structure. With this information, we can now narrow down the factors that might be responsible for the $Au|PA_A|PA_C|Au$ junction's asymmetric I-V response.

The results from small amplitude impedance measurements in Chapter-II on single-layer $Au|Ionomer|Au$ samples have shown that, although the mobile ions in PA_A move slower than the mobile ions in PA_C, the ionic double layer capacitance of the two ionomers are comparable to each other during the low frequency electrode polarization, with the capacitance value of PA_A slightly higher. The results in Chapter-III and Chapter-IV further showed that the electronic properties of the two ionomers are very similar in that, both ionomers show similar onset voltages for unipolar and bipolar charge injection, and the steady-state electronic current of both ionomers are comparable and exhibit a similar dependence on applied bias. Therefore

in the Au|PA$_A$|PA$_C$|Au junction, the asymmetry in charge injection barrier between forward and reverse bias is negligible at almost all bias levels.

If charge injection can easily occur in both forward and reverse bias, then there must be other factors that are limiting the current at reverse bias. One natural candidate of such limiting factor is the asymmetric response of the PA$_A$|PA$_C$ interface to different signs of bias, as suggested by the "ionic P-N junction" hypothesis. The comparison of the capacitance spectrum between the Au|Ionomer|Au structure and the Au|PA$_A$|PA$_C$|Au structure in Chapter-II indeed suggest that an interfacial capacitance at the PA$_A$|PA$_C$ interface exists. Given the plausibility that the PA$_A$|PA$_C$ interface is responsible for the asymmetric I-V response of the Au|PA$_A$|PA$_C$|Au junction, several experiments will be carried out in this chapter to elucidate how the Au|PA$_A$|PA$_C$|Au junction works differently under forward versus reverse biases, with a focus on understanding the role of the PA$_A$|PA$_C$ interface.

Time dependent current-voltage measurements and impedance spectroscopy will be used to characterize the response of the Au|PA$_A$|PA$_C$|Au junction to constant biases of different magnitude at both bias directions, as well as the relaxation of the junction from the steady-state at different biases. The amount of injected charge at each bias will be estimated through short-circuit discharging of the system from steady-state, and the distribution of the injected charge will be studied through impedance spectroscopy at steady-state. The important role of ion transport across the PA$_A$|PA$_C$ interface will be illustrated by a control experiment where the ion transport across the PA$_A$|PA$_C$ is intentionally impeded.

5.2 Experimental details

5.2.1 Sample preparation

The bi-layer Au|PA$_A$|PA$_C$|Au samples were prepared and annealed following the same procedures as described in the experimental details section in Chapter-II.

Samples in $Au|PA_A|Au|PA_C|Au$ configuration were also fabricated by evaporating an additional 50 Å gold layer on top of the PA_C layer before the PA_A layer is spin-coated and the top Au contact is evaporated.

5.2.2 Current-voltage measurements

All current-voltage measurements were conducted under active vacuum ($<$20 mTorr) except when exposure to acetonitrile vapor is needed. A Keithley 236 Source-Measure Unit in combination with a Keithley 7001 switching matrix was used for all current-voltage measurements. A custom labview program was used for controlling the instruments and recording data. A typical experiment starts from applying a bias to the Au|Ionomer|Au sample and measuring the current as a function of time, $I_B(t)$, until the system reaches or nears steady-state, then the instrument is switched to either measuring the short-circuit current as a function of time, $I_{SC}(t)$, or measuring the open-circuit potential as a function of time, $V_{OC}(t)$, during the relaxation of the system from steady-state. During the transition between different measurements, the system is switched into open circuit for a brief moment ($<$1 ms) as needed for switching the function of Keithley 236. After each open-circuit measurement, the system is left at short-circuit until the sample is fully relaxed as indicated by the leveling off of the short-circuit current.

5.2.3 Impedance measurements

A Solartron SI-1296A dielectric interface in combination with a Solartron SI-1260 impedance analyzer was used for all impedance measurements. The SMART software from Solartron Analytical was used for interfacing both the SI-1296A and the SI-1260, as well as recording data. The amplitude of the AC voltage signal was 50 mV for all impedance measurements throughout this chapter. The range of DC voltages used for biased impedance measurements was -1.5 V to $+$ 1.5 V, PA_A versus PA_C, in 0.2

V increments. All impedance measurements were done while the sample was in an actively evacuated container (P<20 mTorr).

In a typical impedance experiment, the response of the $Au|PA_A|PA_C|Au$ sample to a 50mV AC signal at f=20kHZ, 2kHZ, 200HZ, 100HZ, 10HZ, 1HZ, 0.1HZ as a function of time was continuously monitored for 1 hour as soon as a DC bias was applied. After the bias had been applied for 90 minutes, an AC impedance spectrum in the frequency range of 1MHZ to 0.01HZ was recorded with data density of 10 points per decade while the sample was still under bias. Then, the sample's impedance response at f=20kHZ, 2kHZ, 200HZ, 100HZ, 10HZ, 1HZ, 0.1HZ was continuously monitored as the DC bias was changed to 0 V, until the sample was relaxed at 0 V for 1 hour.

5.3 Results and discussion

In presenting the experimental results throughout this chapter, a voltage applied to the $Au|PA_A|PA_C|Au$ junction will be referred to as "forward" or "positive" when the electrode at the PA_A side is held at a higher potential than the electrode at the PA_C side. "Steady-state" refers to the state of the device at the end of a typical 90 minute (unless indicated otherwise) bias at various applied voltages. It was found that after applying a bias for 90 minutes to a typical $Au|PA_A|PA_C|Au$ sample, the overall current continued to change slowly. Although at the end of a 90-minute bias a true steady-state was not reached, results from experiments of longer bias times have indicated that a longer bias time was not necessary for the purpose of qualitative analysis, therefore the 90-minute bias time was used for most current-voltage measurements.

5.3.1 Response to stepping applied bias

The response of a $Au|PA_A|PA_C|Au$ sample to a constant applied voltage is shown in Fig-5.1 through the change of overall current with time, $I_B(t)$, for various biases

in both forward (top graph) and reverse (bottom graph) direction. Two sets of data
for each bias were shown together to demonstrate the consistency of the response
between repeated measurements on the same sample. The data were plotted in log-
log scale so that fast changes at the early stage of response can be better seen, and
large relative changes within small ranges are not obscured.
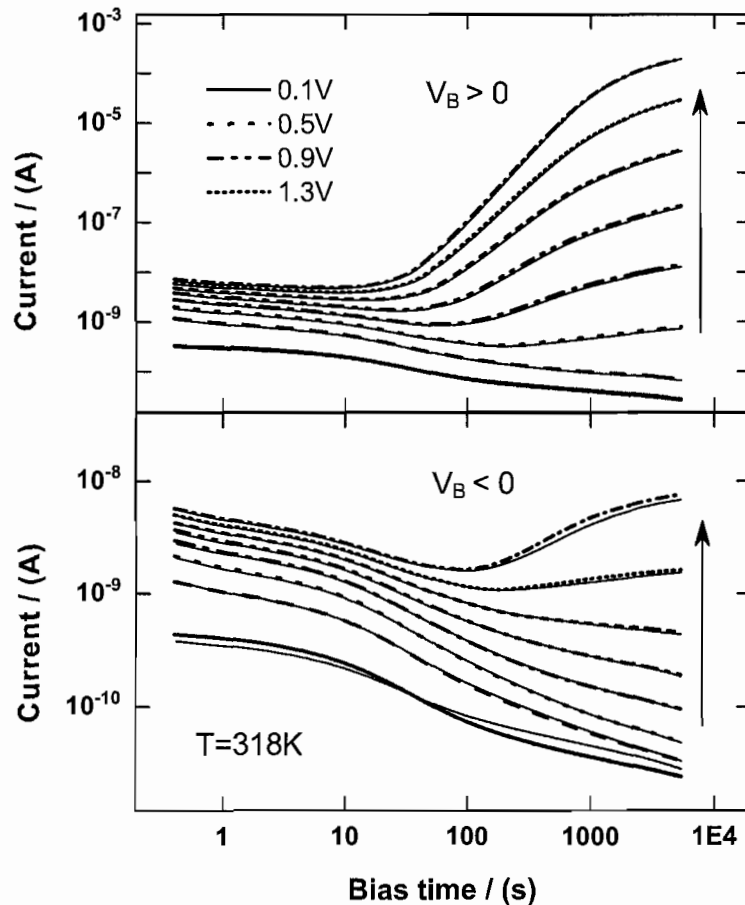
FIGURE 5.1: The time dependent current of a Au|PA$_A$|PA$_C$|Au sample (220|300
nm) under forward (top) and reverse (bottom) stepping biases. The bias voltage
difference between neighboring curves was 0.2 V, and the range of applied bias was
from 0.1 V to 1.5V in both directions. The results of two repeated measurements on
the same sample are shown to demonstrate consistency between measurements.

At positive biases, the change of $I_B(t)$ with time and bias in Fig-5.1 looks very
similar to the response of a single-layer PA$_A$ sample shown in Fig-4.1 of Chapter-

IV. While at negative biases, the time scale of change in $I_B(t)$ is similar to that of the PA_A sample, but with much lower current at the same magnitude of bias. The similarity between the response of $Au|PA_A|PA_C|Au$ and the response of single-layer PA_A at positive biases is reflective of the fact that the lower ionic conductivity of the PA_A layer is limiting the response speed of the $Au|PA_A|PA_C|Au$ structure. The ionic conductivity extracted from the initial value of $I_B(t)$ is about 2×10^{-12} S/cm, which agrees rather well with the value of 3×10^{-12} S/cm obtained from impedance measurements for PA_A at 318 K.
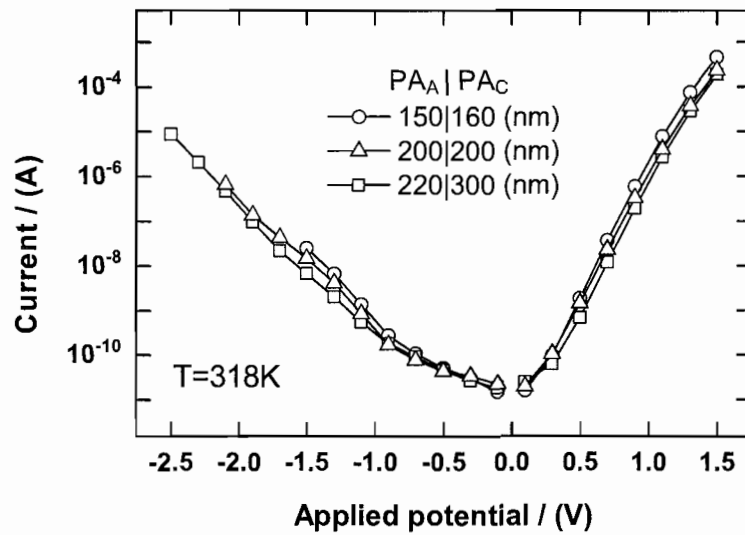
FIGURE 5.2: The steady-state current as a function of bias for three $Au|PA_A|PA_C|Au$ samples of different thickness. Data points are represented by symbols.

The steady-state current (I_{SS}) at the end of a 90-minute bias for three samples of different thicknesses are shown in Fig-5.2 as a function of applied bias. At forward biases, the steady-state current exhibit a close to exponential increase with increasing bias magnitude, and a thickness dependence can be identified for biases higher than 0.3 V with lower currents corresponding to thicker samples. At reverse biases, the change of steady-state current with bias is slower than at forward biases, and the

thickness dependance of I_{SS} can not be clearly seen until the bias magnitude is greater than 0.5 V where I_{SS} also begin to show stronger dependence on bias magnitude.

The current-voltage relation of the Au|PA$_A$|PA$_C$|Au junction as shown in Fig-5.2 is quite different from that of a typical silicon *pn* junction where the reverse current levels off with the increase of reverse bias magnitude until the breakdown voltage is reached. This difference in I-V relation between a mix-conducting Au|PA$_A$|PA$_C$|Au junction and a purely electronic *pn* junction indicates that their operating mechanisms are fundamentally different.
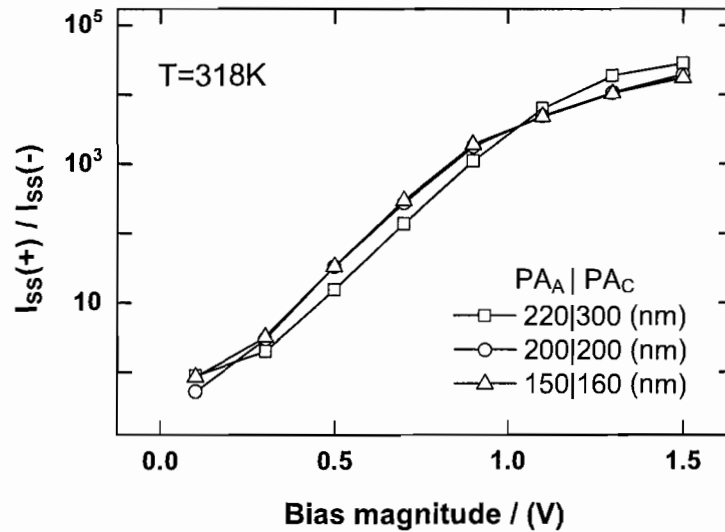
FIGURE 5.3: The ratio between near steady-state current of the forward and reverse bias, as a function of bias magnitude for three Au|PA$_A$|PA$_C$|Au samples of different thickness. Data points are represented by symbols.

Fig-5.3 shows the typical bias magnitude dependance of the steady-state current ratio, or rectification ratio, between forward and reverse bias at the same bias magnitude for three samples of different thickness. It is seen in Fig-5.3 that, the rectification ratio increases with increasing bias magnitude rapidly before $|V_B|$=1.1 V, and reaches around 2×10^4 at $|V_B|$=1.5 V. It can also been seen from Fig-5.3 that the rectification ratio data of the two samples in which the thicknesses of the PA$_A$

layer and the PA_C layer are similar show excellent overlap except the lowest bias, while the other sample in which the PA_C layer was thicker than the PA_A layer shows relatively lower rectification ratio for $|V_B|<1.1$ V and higher rectification ratio for $|V_B|>1.1$ V.

5.3.2 Open-circuit relaxation from bias

The changes of open-circuit potential as a function of time during the relaxation of the $Au|PA_A|PA_C|Au$ junction from steady-state at different forward (top) and reverse (bottom) biases are shown in Fig-5.4, with the time axis in logarithmic scale. It is observed that the time dependent open-circuit potential of both bias directions evolve with bias magnitude in a way that is consistent with Eq. (4.2) in Chapter-IV. At biases that resulted in a steady-state electronic conductivity that is substantially lower than the ionic conductivity, which is the case for -1.3 V$\leq V_B \leq +0.3$ V, the initial values of V_{OC} are close to the magnitudes of applied bias. At other biases, the initial values of V_{OC} differ from $|V_B|$ to various degrees depending on the corresponding steady-state current at each bias, and the relaxation of V_{OC} over time is reflective of the redistribution of mobile cations in PA_A as indicated by the time scale of the initial slow decay of $V_{OC}(t)$ for $V_B>0.5$ V and $V_B=-1.5$ V.

Exposing the $Au|PA_A|PA_C|Au$ junction to acetonitrile vapor increases the limiting initial value of $V_{OC}(0)$ for both forward and reverse biases, as can be seen in Fig-5.5 where the $V_{OC}(0)$ values of three different samples in their dried state are also shown. The change in the limiting value of $V_{OC}(0)$ upon exposing the sample to solvent vapor is similar to the observations on the single-layer $Au|Ionomer|Au$ structure, and consistent with the prediction of Eq. (4.2) upon changing the ratio between electronic conductivity and ionic conductivity. A limiting $V_{OC}(0)$ value of around 1.2 V at $V_B=-1.5$ V indicates that for reverse biases in the range of -0.1 V to -1.5 V, all the injected electronic charge carriers are compensated by mobile ions.
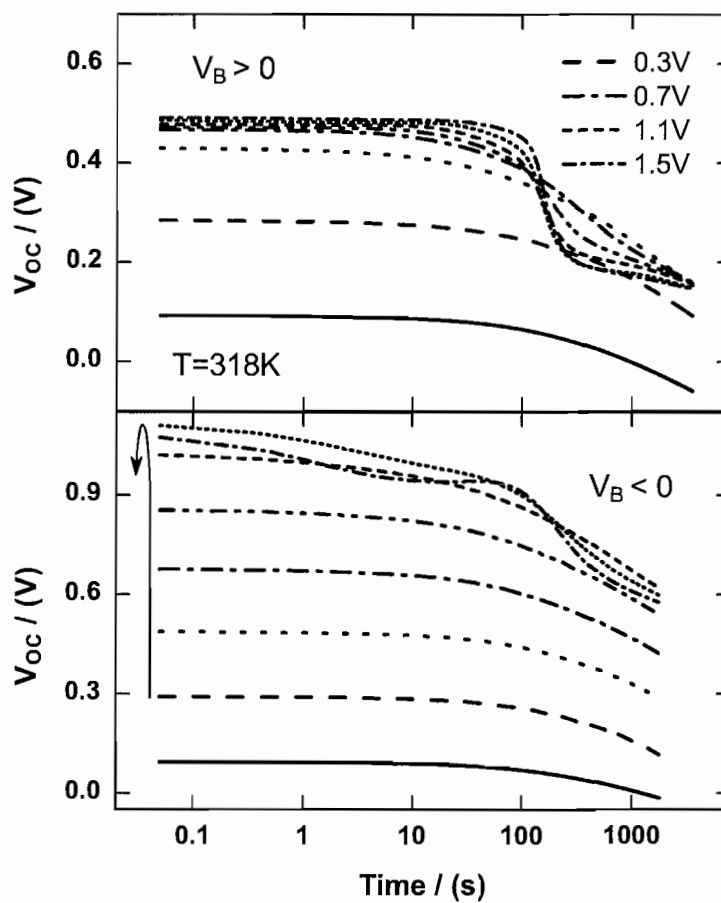
FIGURE 5.4: Change of the open-circuit potential of a 220|300 nm Au|PA$_A$|PA$_C$|Au sample during the relaxation from the steady-states of different forward (top) and reverse (bottom) biases. The difference between the magnitude of two adjacent biases was 0.2 v.
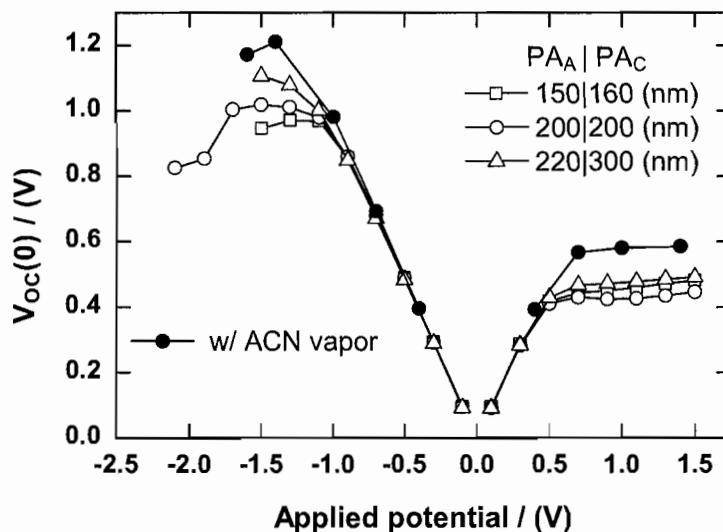
FIGURE 5.5: The initial open-circuit potential as a function of applied bias for three $Au|PA_A|PA_C|Au$ samples of different thickness. The data represented by solid symbols were collected from the 200|200 nm sample at the presence of acetonitrile vapor.

5.3.3 Internal discharging during open-circuit

A quantity of key importance is the total amount of electronic charge carriers that were injected at the steady-state of each bias. One way of estimating the amount of injected charge is discharging the sample from steady-state through short-circuiting and integrate the short-circuit current. Similar to the case of single-layer structure, the mix-conducting nature of the ionomers used will inevitably result in a portion of the injected charge recombining internally and hence leading to an underestimate of the total charge by integrating the short-circuit current. The extend of this underestimate, however, can be assessed via the same way that was used in Chapter-IV, where an open-circuit state is maintained for various lengths of time between the removal of applied bias and the beginning of short-circuit measurement. The amount of charge lost to internal recombination as a function of time in open-circuit state can then be used to estimate what percentage of the total injected charge might have been lost during the short-circuit measurement.
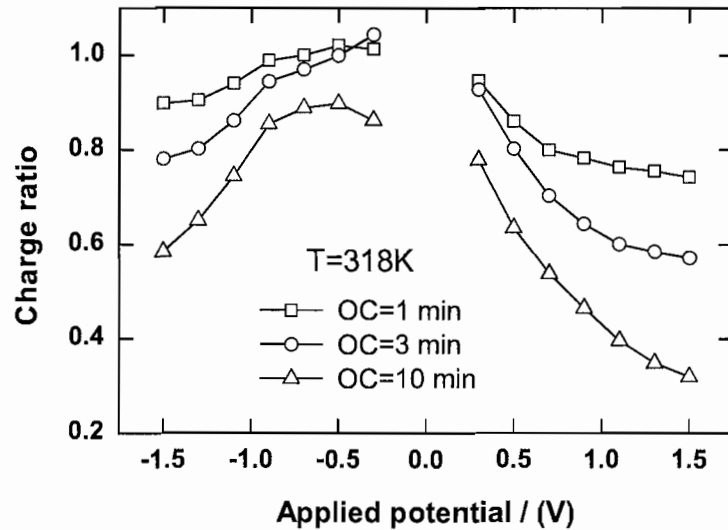
FIGURE 5.6: The ratio of charges recovered through short-circuiting after a short period of open-circuit relaxation following the removal of bias, to the total charge recovered through immediate short-circuiting from steady-state.

Fig-5.6 shows the ratio of the amount of charge recovered after different lengths of open-circuit times (1 minute, 3 minutes, and 10 minutes), to the amount of charge recovered through immediate short-circuiting, for various bias voltages. Note that a ratio greater than 1 that is observed from the data of negative biases of low magnitude for short open-circuit times is a result of negligible internal recombination and small variation of results among repeated measurements. In general, the percentage of total charge lost during the open-circuit period increases with increasing steady-state current (internal electronic conductivity) and increasing open-circuit time. Therefore by short-circuiting, the estimates of injected charge for reverse biases are always closer to the true value than the estimates for forward biases at same bias magnitude. For forward biases less than 1.5 V, the short-circuit charge should account for more than half of the true amount of injected charge, given the fact that the external impedance is much lower than the internal electronic conductivity during short-circuiting.

5.3.4 Short-circuit relaxation from bias

Typical data of time dependent short-circuit currents of both forward (top) and reverse (bottom) biases within the range of ± 1.5 V are shown in Fig-5.7 for a Au|PA$_A$|PA$_C$|Au sample of 220|300 nm. Two sets of data are plotted together in Fig-5.7 to show that variations between repeated measurements on the same sample are not significant.
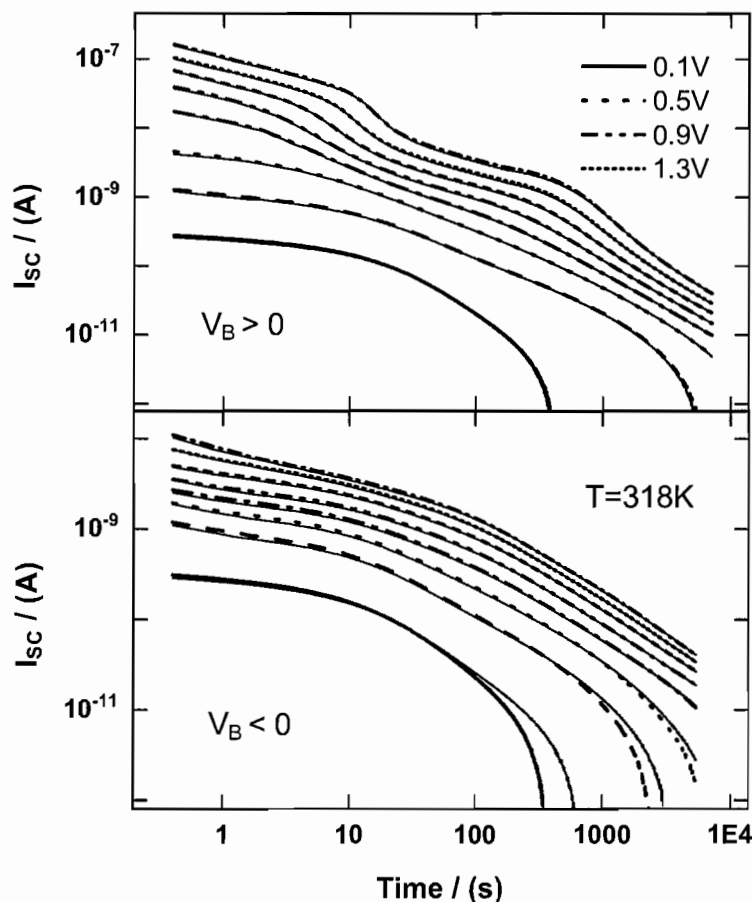
FIGURE 5.7: The change of short-circuit current as a function of time for a 220|300 nm Au|PA$_A$|PA$_C$|Au sample during the short-circuit relaxation from the steady states at different forward (top) and reverse (bottom) biases.

From Fig-5.7, a significant difference in the time dependance of of $I_{SC}(t)$ between forward and reverse biases can be identified. At reverse biases, the time

dependance of $I_{SC}(t)$ for $|V_B|>0.5$ V is very similar to that of $|V_B|<0.5$ V. At forward biases, however, two relatively slow changing region on the $I_{SC}(t)$ curves along the logarithmic time begin to emerge for biases higher than 0.7 V. And at $V_B=+1.5$ V, the $I_{SC}(t)$ curve looks much like the superposition of two discharging processes of different time scales, with the faster process having a time constant similar to the discharging of a single-layer PA_C sample and the slower process having a time constant close to that of discharging a single-layer PA_A sample.

One possible explanation for the particular shape of $I_{SC}(t)$ at $V_B=1.5$ V is that the total amount of injected charge has two components, one component was compensated by the redistribution of mobile anions provided by PA_C, and the other component was compensated by the redistribution of mobile cations provided by PA_A. During the short-circuit discharging, the anion compensated component discharges faster due to the higher mobility of anions, as implied by the result from impedance measurements. This explanation would imply that under forward biases higher than 0.7 V, some anions from the PA_C layer have accumulated in the PA_A layer to provide charge compensation for injected holes, while a certain amount of cations from the PA_A layer have moved into the PA_C layer to compensate the charge of injected electrons.

The total amount of charge integrated from short-circuit current is shown in Fig-5.8 as a function of applied bias for two $Au|PA_A|PA_C|Au$ samples of different thickness. The simulated result of charging a typical ionic double layer that has a equivalent capacitance of 3 $\mu F/cm^2$ is also shown for comparison. It is seen from Fig-5.8 that, for $V_B<-1.3$ V, the voltage dependence of short-circuit charge is very similar to that of charging a capacitor with equivalent capacitance of about 6 $\mu F/cm^2$, while for -0.7 V$<V_B<0.5$ V, the short-circuit charge is close to or less than that of charging a 3 $\mu F/cm^2$ equivalent capacitor. At forward biases higher than 0.5 V the short-circuit charge appears to increase exponentially with increasing bias, although
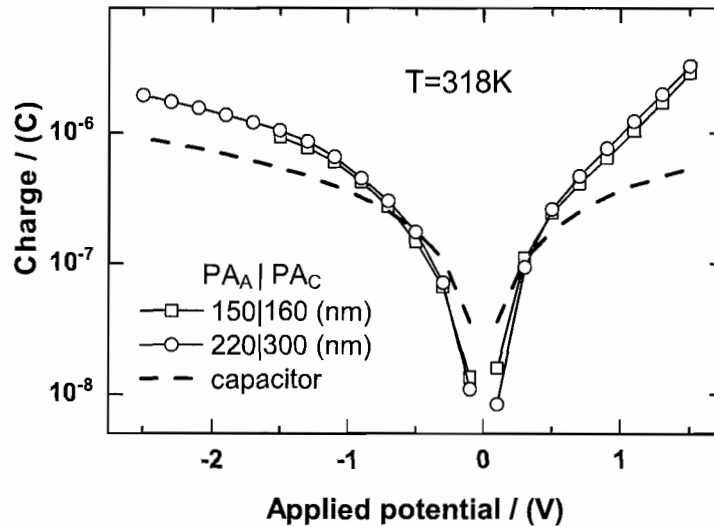
FIGURE 5.8: The total charges obtained from short-circuit experiments as a function of applied bias for two $Au|PA_A|PA_C|Au$ samples. The theoretical values of charging a double layer with 3 $\mu F/cm^2$ capacitance and an area of the sample are represented by dashed lines.

the actual increase could be faster than what is shown in Fig-5.8 if the charges lost to internal recombination, which also increases with bias, are taken into account.

Another way of showing the short-circuit charge differences between forward and reverse bias is calculating the ratio of short-circuit charge between forward and reverse biases of the same magnitude. The result of this charge ratio is shown in Fig-5.9 as a function of bias magnitude for two sets of separate measurements on the same sample. Note that due to the more significant loss of charge to internal recombination for higher forward biases as compare to reverse biases, the actual ratio could be higher for $|V_B|>0.5$ V. The charge ratio starts off at about 1 for the lowest bias, then stays at around 1.6 for $|V_B|=0.3$ V, 0.5 V, 0.7 V, and 0.9 V. After $|V_B|=0.9$ V, the charge ratio begins to increase quickly.

The difference in the amount of short-circuit charge between forward and reverse biases, and their bias magnitude dependence suggest that the charge injection process at reverse biases is likely coupled to a non-Faradic interfacial charging process, while
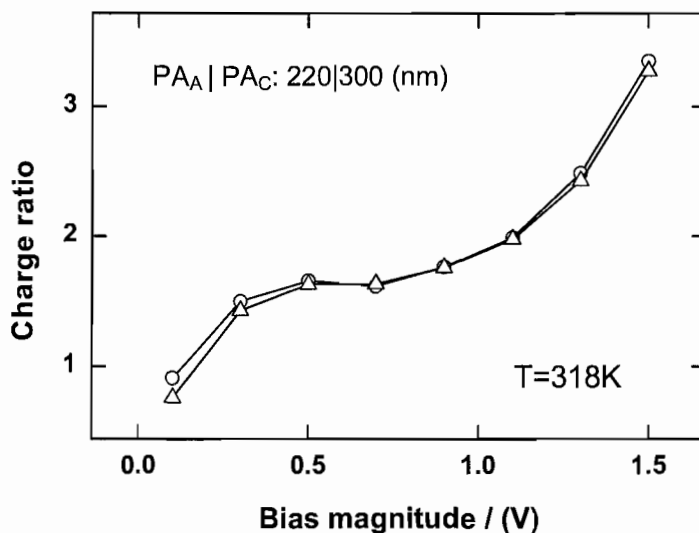
FIGURE 5.9: The ratio of short-circuit charge between forward and reverse bias of the same magnitude, for two separate sets of measurements on a 220|300 nm Au|PA$_A$|PA$_C$|Au sample.

the charge injection process at forward biases higher than 0.9 V is coupled to a Faradaic process involving the bulk of material.

5.3.5 Monitoring the sample with impedance spectroscopy

As an attempt to obtain information about the electronic charge carrier density and spatial distribution at the steady-state of each bias, the small-amplitude (50 mV) AC impedance spectrum of the Au|PA$_A$|PA$_C$|Au junction at steady-state was recorded for all applied biases, in the frequency range of 0.01HZ to 1MHZ. Since the impedance spectrum involving the mobile ions will not change with bias, any change in the overall impedance spectrum can be attributed to the electronic charge carriers.

The steady-state impedance spectra of a Au|PA$_A$|PA$_C$|Au sample for reverse biases between -0.1 V and -1.5 V are shown in Fig-5.10, in terms of phase angle (top), apparent capacitance (bottom,left ordinate), and apparent conductivity (bottom, right ordinate). It can be seen that for $|V_B|<1.1$ V, the conductivity

FIGURE 5.10: The phase angle (top), capacitance per unit area (bottom, left ordinate), and conductivity (bottom, right ordinate) of a $Au|PA_A|PA_C|Au$ sample as a function of frequency (in log scale), when the sample is near steady-state under different reverse biases.

spectrum and capacitance spectrum are dominated by that of the mobile cations, and the effect of electronic charge carriers can be better seen from the change of phase angle spectrum as the applied bias changes. For $|V_B|>1.1$ V, the change in impedance response due to electronic charge carriers can be clearly seen in all three spectra. Interestingly, at $V_B=-1.5$ V, the capacitance value in the low frequency region becomes negative as the corresponding phase angle becomes positive. The origin of the negative capacitance will be discussed later.

FIGURE 5.11: The phase angle (top), capacitance per unit area(bottom, left ordinate), and conductivity (bottom, right ordinate) as a function of frequency (in log scale) for a 200|200 nm Au|PA$_A$|PA$_C$|Au sample , when the sample is near steady-state under different forward biases.

Fig-5.11 shows the steady-state impedance spectra of the same sample as in Fig-5.10 under forward biases between 0.1 V and 1.5 V. In Fig-5.11, the changes in

impedance spectra due to electronic charge carriers can be clearly seen for all but the lowest bias. It is observed that the low frequency (f<0.2 HZ) apparent capacitance of the junction increases by orders of magnitude as bias increases, and for biases close to +1.5 V there is a frequency range within which the apparent capacitance become negative. Interestingly the sign of low frequency apparent capacitance was also found to be inconsistent among samples, as evidenced by the impedance spectra of a different sample shown in Fig-5.12, where the low frequency apparent capacitances are negative although the magnitudes are comparable to that of the other sample shown in Fig-5.11.

The large magnitude of the low frequency apparent capacitance can be explained by the change in the amount of injected charge induced by the 50 mV AC signal. In the low frequency region, mobile ions in the active material will be able to redistribute to compensate for any additional injected electronic charge carriers, therefore the AC signal will in effect modulate the doping density of the material. In the voltage regime of bipolar charge injection the capacitance of the material is determined by its volume, hence a very large apparent capacitance value on the order of 10^{-3} F/cm^2 is achievable.

The origin of the negative apparent capacitance that was observed in the low frequency region for high biases of both directions is unclear. It is possible that when the phase angle is very close to zero, small changes in the overall conductivity due to the AC signal could result in a positive apparent phase angle.

For forward biases higher than 0.3 V, a relaxation process that has an apparent capacitance of about 30 nF/cm^2 can be identified from Fig-5.11, most visibly by a shoulder feature in the capacitance spectrum that moves towards higher frequency as the bias magnitude increases. A zoom in view of this shoulder feature is shown in Fig-5.13 for three samples of different thickness at V_B=1.3 V and V_B=1.5 V. For comparison, the geometric capacitance of the 400 nm thick Au|PA$_A$|PA$_C$|Au structure is about 1.1×10^{-8} F/cm^2. Corresponding to this shoulder feature, a small change
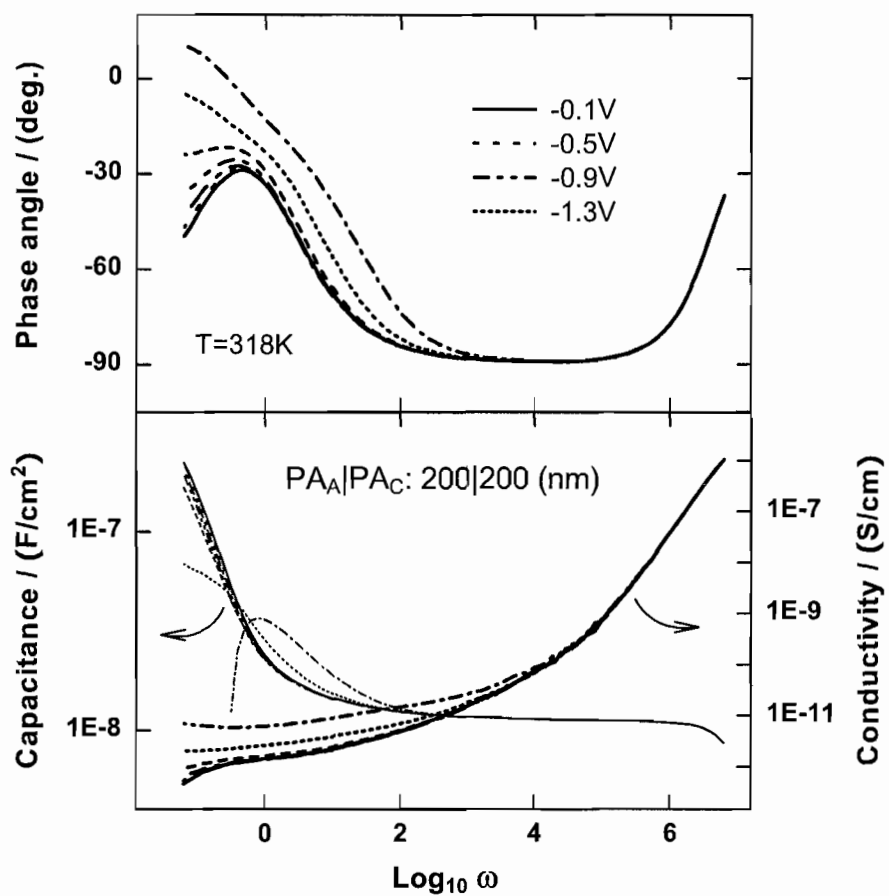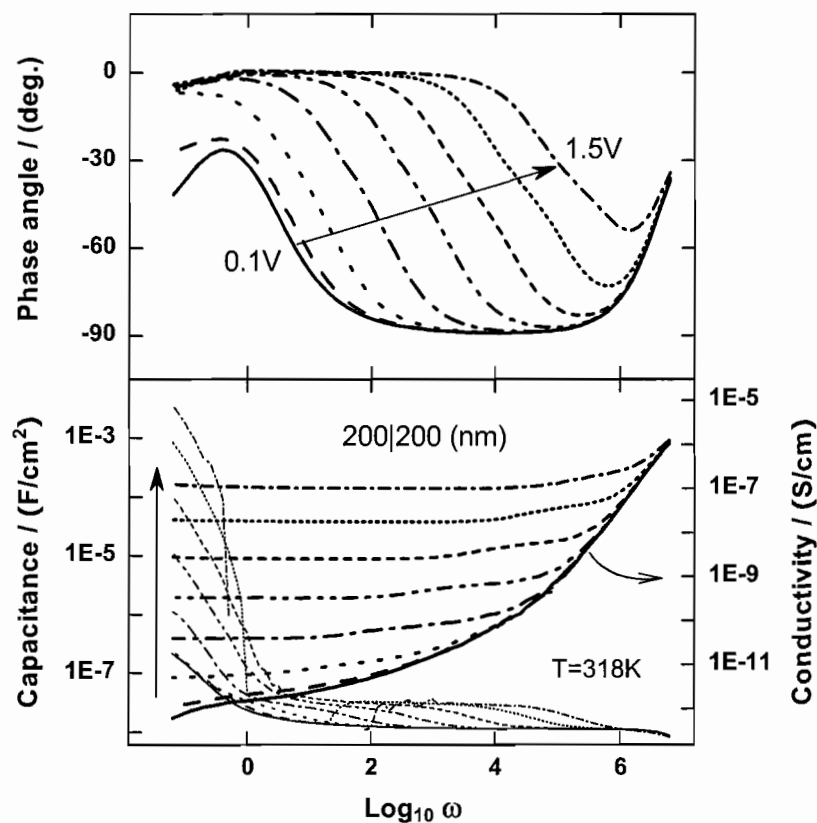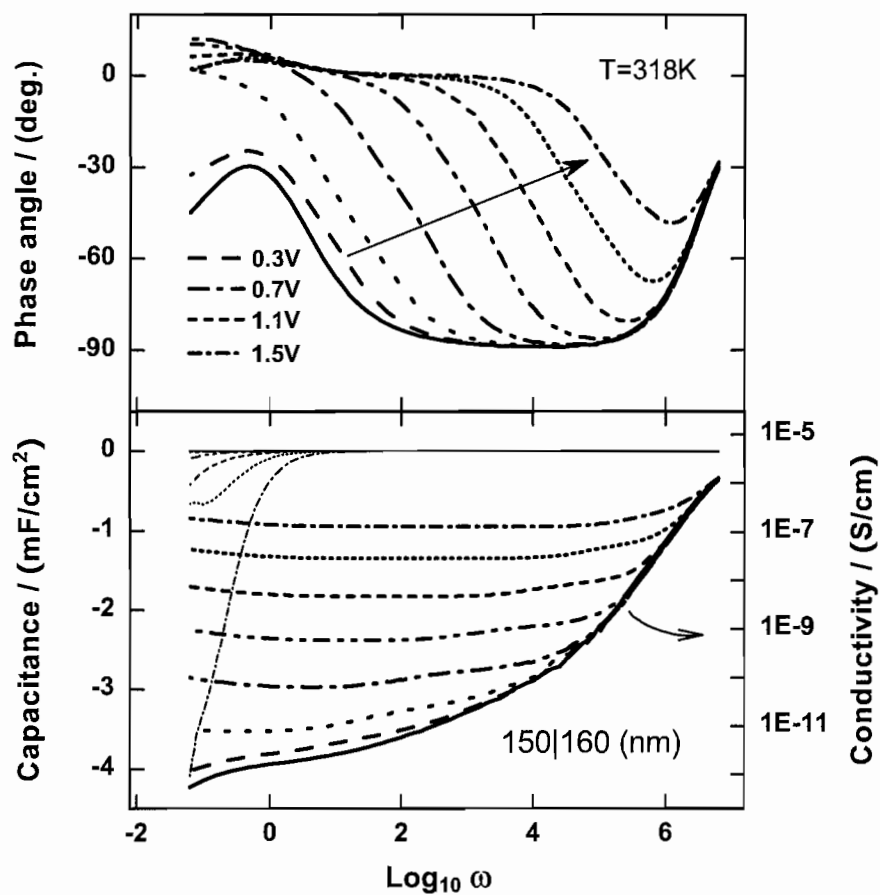
FIGURE 5.12: The phase angle (top), capacitance per unit area(bottom, left ordinate), and conductivity (bottom, right ordinate) as a function of frequency (in log scale) for a 150|160 nm Au|PA$_A$|PA$_C$|Au sample , when the sample is near steady-state under different forward biases.
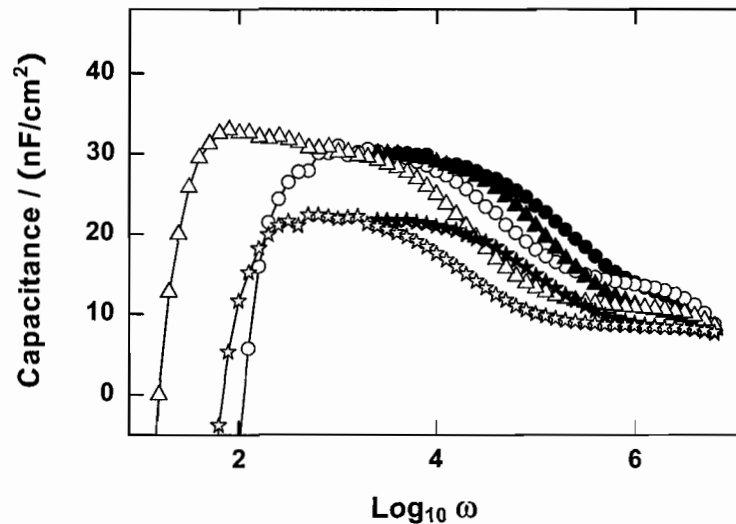
FIGURE 5.13: The partial apparent capacitance spectrum of three $Au|PA_A|PA_C|Au$ samples of different thickness at V_B=+1.3 V (open symbols) and V_B=+1.5 V (solid symbols). Circles—150|160 nm, triangles—200|200 nm, stars—220|300 nm.

can also be identified from the conductivity spectrum. It is observed in Fig-5.13 that the capacitance value ($\approx$30 nF/cm^2) at the low frequency side of this shoulder is almost equal for the sample of 150|160 nm and the sample of 200|200 nm, while the corresponding capacitance value for the 200|300 nm sample is lower by about 10 nF/cm^2. The capacitance values at the high frequency side of the shoulder feature is around the value of the geometric capacitance for each sample, and the values vary according to each sample's total thickness.

The observed relaxation process and its bias dependence could be qualitatively explained if one assumes that the injected electrons in the PA_C layer at forward bias have a much lower mobility than the injected holes in the PA_A layer. In such case, there will be a frequency range within which electrons can not follow the AC signal while holes where able to, hence the PA_A layer and the PA_C layer will behave like a resistor (PA_A) and capacitor (PA_C) in series with the resistance of PA_A changing with the applied bias. The time constant of this RC relaxation is determined by the resistance of the hole-containing region, and the thickness of the electronic-only
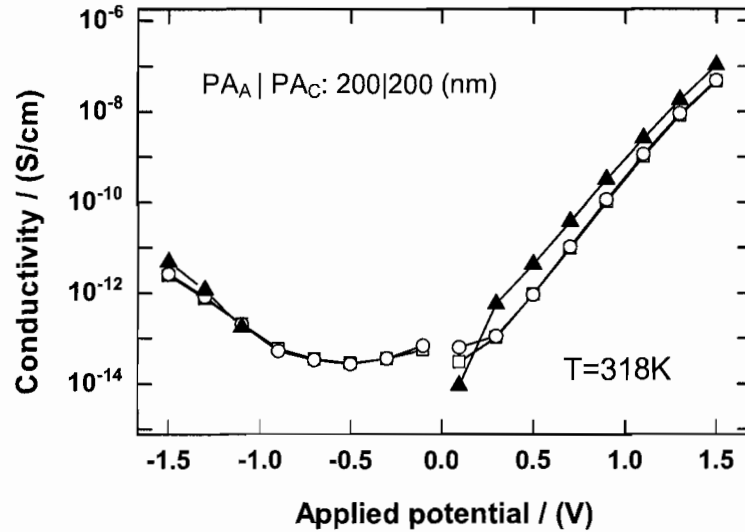
FIGURE 5.14: The apparent .conductivity as a function of applied bias of a 200|200 nm Au|PA$_A$|PA$_C$|Au sample calculated from one set of biased impedance data at f=0.16 HZ (solid triangles) and two sets of steady-state current data (open squares and open circles).

region which could be as large as the thickness of the PA$_C$ layer. A calculation of the thickness d of the electron-only region based on the capacitance values of the RC relaxation gives $d \approx 145$ nm for the 150|160 nm sample , $d \approx 150$ nm for the 200|200 nm sample, and $d \approx 200$ nm for the 220|300 nm sample. An example of similar RC relaxation due to difference in charge carrier mobility is the impedance response of the Au|PA$_A$|PA$_C$|Au without a DC bias (see Fig-2.18 in Chapter-II).

The apparent electronic conductivity of the entire Au|PA$_A$|PA$_C$|Au structure can be estimated either from the steady-state current through $\sigma_{app} = \dfrac{I_{ss}l}{V_B A}$ (where l is the separation between Au electrodes and A is the electrode area), or from the biased conductivity spectra after correcting for ionic conductivity. A comparison of the resulting σ_{app} values from both methods is presented in Fig-5.14. For forward biases, it is seen that the σ_{app} values obtained from AC impedance data (at f=0.16 HZ) are substantially higher than the values calculated from steady-state current except for the lowest bias where the result is less reliable. At high magnitude reverse

biases ($|V_B|>1.1$ V) the σ_{app} values from impedance data are also higher than that calculated from I_{SS}. At low magnitude reverse biases the electronic conductivities are too low to be reliably extracted from impedance data, therefore only the results calculated from steady-state current are shown. It is interesting to see that at low magnitude reverse biases, the apparent conductivity value initially decreases with increasing bias magnitude before reaching the lowest value at $V_B=-0.5$ V and then increases as bias magnitude increased further. This initial decrease of σ_{app} at low reverse biases will be discussed later.

The observation that the σ_{app} values obtained from AC impedance data are higher than that calculated from the I_{SS} for $V_B>0.1$ V and $V_B<-1.1$ V suggest that, in the impedance result, there is an additional contribution to the apparent conductivity from the response of electronic charge carriers within the material to the AC signal, and this contribution increases with the increase of applied bias magnitude. This observation seemed consistent with the earlier assumption of an RC relaxation due to the mobility difference between holes in the PA_A layer and electrons in the PA_C layer at forward bias and vice versus at reverse bias. The difference between the two methods of calculating apparent conductivity is also consistent with a difference in mobility between holes and electrons, since the low mobility of electrons will have a stronger effect on the calculated value of apparent conductivity from steady-state current.

To monitor the in-situ changes of electronic charge carriers in the $Au|PA_A|PA_C|Au$ junction in response to an applied bias as well as during the course of relaxation from steady-state, the response of the junction to a small amplitude AC voltage signal of 50 mV was monitored at $f=20$kHZ, 2kHZ, 200HZ, 100HZ, 10HZ, 1HZ and 0.1HZ during the system's evolution to and relaxation from steady-state. The result of such an impedance measurement is shown in Fig-5.15 for $V_B=+1.5$V and in Fig-5.16 for $V_B=-1.5$V, with an emphasis on the relaxation process. The relaxation process starts at t=60 minute for all graphs.

FIGURE 5.15: The change in conductivity and phase angle of a Au|PA$_A$|PA$_C$|Au sample as a function of time during the evolution to steady-state and relaxation from steady-state at 0.1HZ, 1HZ, 10HZ, 120HZ, 2kHZ, 20kHZ, for a forward bias of 1.5 V. The data at f=120HZ was interpolated from that of f=100HZ and f=200HZ.

A comparison of the relaxation process between Fig-5.15 and Fig-5.16 shows the drastic differences between forward and reverse biases. In the reverse bias, changes in both the conductivity spectrum and the phase angle spectrum during the relaxation process only last for a few minutes, and most of the changes occur in the low frequency region. For the forward bias, the changes in both conductivity spectrum and phase angle spectrum during the relaxation process are more significant and feature-rich. Changes in conductivity at all monitored frequencies can be clearly seen for the first 10 minutes during the relaxation from V_B=1.5 V, and the low frequency phase angle shows an interesting initial dip towards a more capacitive value before rise up again and then approaches the value at zero bias. These changes suggest that significant amount of electronic charge carriers have been injected into the ionomers at V_B=1.5 V, and it took at least several minutes for them to completely disappear during the relaxation from steady-state.

5.3.6 Blocking the ion exchange at the PA$_A$|PA$_C$ interface

For the purpose of illustrating the crucial role of the PA$_A$|PA$_C$ interface and show that the ability for mobile ions to move across the PA$_A$|PA$_C$ interface is essential to
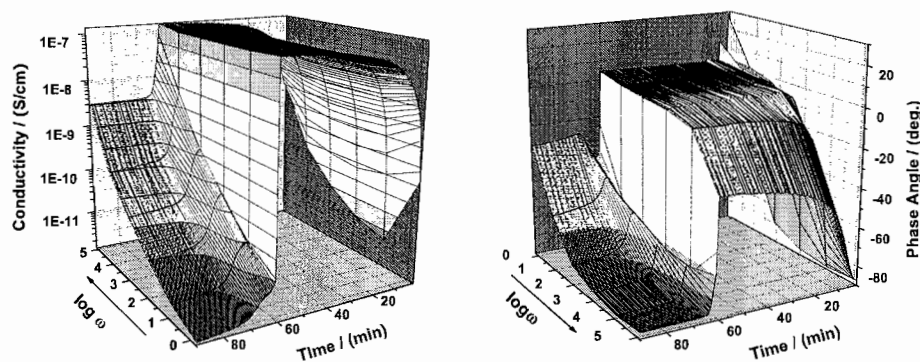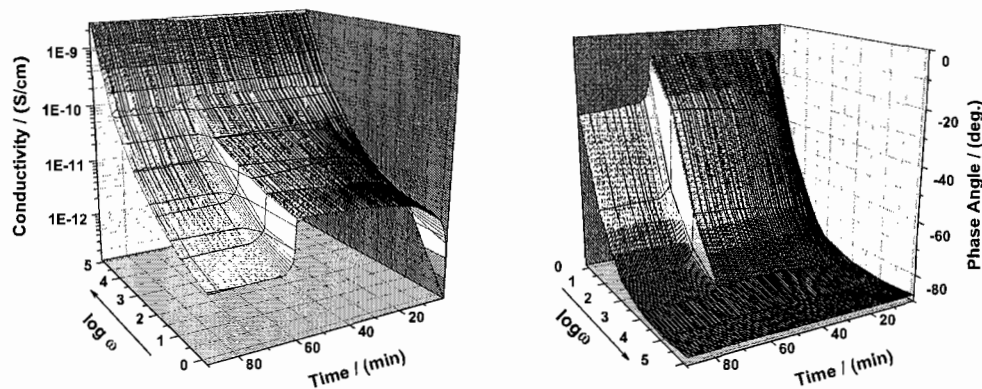
FIGURE 5.16: The change in conductivity and phase angle of a Au|PA$_A$|PA$_C$|Au sample as a function of time during the evolution to steady-state and relaxation from steady-state at f=0.1HZ, 1HZ, 10HZ, 120HZ, 2kHZ, 20kHZ, for a reverse bias of 1.5 V. The data at f=120HZ was interpolated from that of f=100HZ and f=200HZ.

the Au|PA$_A$|PA$_C$|Au junction's asymmetric I-V response, a control experiment was carried out on a modified structure in which an additional 50Å Au layer was inserted between the two ionomer layers. Previous electrochemical studies on polyacetylene ionomers have shown that a thin Au layer is permeable to mobile ions when the sample is soaked with acetonitrile. It is believed that when the sample is dried, a Au layer between the PA$_A$ and PA$_C$ will significantly impede the ion flow across the interface if not blocking the ion flow completely. Therefore it is predicted that a Au|PA$_A$|Au|PA$_C$|Au sample should behave similar to a normal Au|PA$_A$|PA$_C$|Au sample when soaked with acetonitrile, and behave just like two Au|Ionomer|Au samples in series when it is dried.

The result of such an experiment on a Au|PA$_A$|Au|PA$_C$|Au sample is shown in Fig-5.17. It can be seen that the I-V response of a dried Au|PA$_A$|Au|PA$_C$|Au sample (thick line) does not exhibit significant asymmetry, while exposing the sample to acetonitrile vapor for 3 minutes was enough to induce a dramatic change in its I-V response (open circles, right ordinate). Drying the sample under active vacuum for several hours after the exposure to acetonitrile vapor changes the Au|PA$_A$|Au|PA$_C$|Au
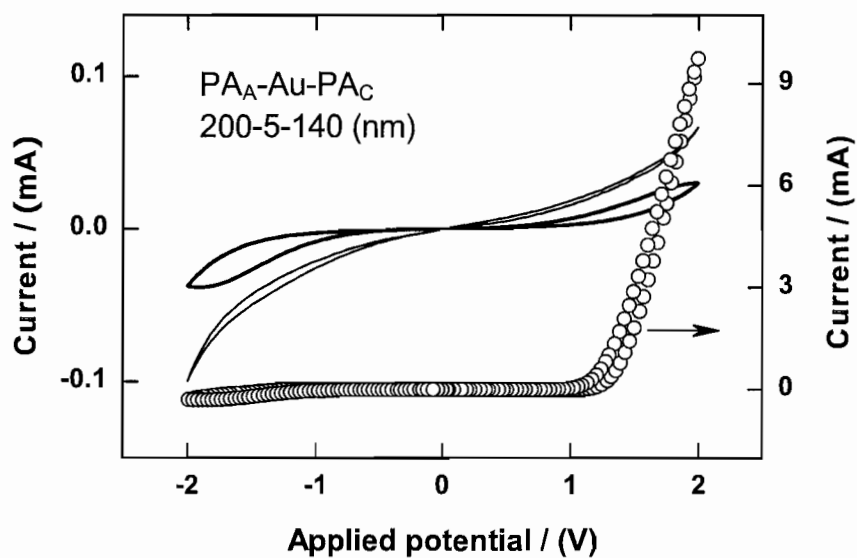
FIGURE 5.17: The change in the I-V response of a $Au|PA_A|Au|PA_C|Au$ sample due to the change of acetonitrile vapor presence. Thick line: in vacuum, before exposure to solvent vapor. Open circles: sample equilibrate with acetonitrile vapor at room temperature. Thin line: in vacuum, after removing the solvent vapor. A scan rate of 0.1 V/s was used.

sample's I-V response (thin line) back to symmetric, but with slightly higher current and less hysteresis than the I-V curve before exposure to acetonitrile vapor.

The dramatic change in the I-V response of the $Au|PA_A|Au|PA_C|Au$ sample after exposure to acetonitrile vapor argues that the ability for mobile ions to exchange across the $PA_A|PA_C$ interface is crucial to the rectifying behavior.

5.3.7 The origin of asymmetric I-V response

A comparison of the $Au|PA_A|PA_C|Au$ structure's capacitance spectrum to that of the $Au|Ionomer|Au$ structure in Chapter-II indicated the existence of an interfacial capacitance between the PA_A layer and the PA_C layer. The results in Chapter-III and Chapter-IV have shown that the charge injection process as well as the electronic charge transport process of the two ionomers are very similar, and the results in this chapter have shown that the ion transport across the $PA_A|PA_C$ interface plays a crucial role in the asymmetric current-voltage response of the $Au|PA_A|PA_C|Au$ structure.

Base on these results, it is logical to assume that an ionic depletion region across the $PA_A|PA_C$ interface exists as a result of mobile ion equilibration, and the direction dependence of ion transport across this depletion region is responsible for the asymmetric I-V response of the $Au|PA_A|PA_C|Au$ junction. A working mechanism, which will be called "dynamic pn junction model", of the mix-conducting $Au|PA_A|PA_C|Au$ junction is consequently proposed as following:

1. Equilibration of mobile ions between the PA_A layer and the PA_C layer results in a built-in field across the $PA_A|PA_C$ interface.

2. At equilibrium, local charge neutrality holds in the bulk of the material excluding the two electrode surface regions and the depletion region near the $PA_A|PA_C$ interface.

3. Equilibration of electronic charge carriers under the influence of a built-in electric field results in the self p-doping of the PA$_A$ layer and the self n-doping of the PA$_C$ layer at zero bias.

4. An applied bias changes the concentration of electronic charge carriers in each ionomer layer through charge injection and consequently changes the concentration of charge-compensating ions until a new dynamic equilibrium is established.

5. The equilibrium concentration of electronic charge carriers at each applied bias determines the overall conductivity of the Au|PA$_A$|PA$_C$|Au junction.

A schematic of the electronic energy levels of the Au|PA$_A$|PA$_C$|Au junction at different biases according the the proposed working mechanism is shown in Fig-5.18. At zero bias (Fig-5.18(a)), the band bending caused by the built-in electric field leads to self p-doping of the PA$_A$ layer and self n-doping of the PA$_C$ layer, charge compensation of holes in PA$_A$ is provided by the diffusion of cations into PA$_C$ as well as the diffusion of anions from PA$_C$ into PA$_A$ and vice versus for electrons in PA$_C$. At forward bias (Fig-5.18(b)), the injection of holes into PA$_A$ increases the p-doping level (and hence the conductivity) of the PA$_A$ layer while driving more mobile cations into the PA$_C$ layer. Consequently, the potential difference across the depletion region decreases. A similar process involving electron injection happens in the PA$_C$ layer. At reverse bias (Fig-5.18(c)), the injection of electrons into the PA$_A$ layer first lead to a decrease of the p-doping level from zero bias, then an increase of n-doping level as the bias magnitude further increases. A similar change of doping level due to the injection of holes happens in the PA$_C$ layer. During the transition between p-doping and n-doping as the magnitude of reverse bias increases, there is an initial decrease of net electronic charge carrier densities in both layers. This initial decrease in charge carrier density could potentially be observed from the change in AC conductivity of the junction as a function of applied reverse bias magnitude.
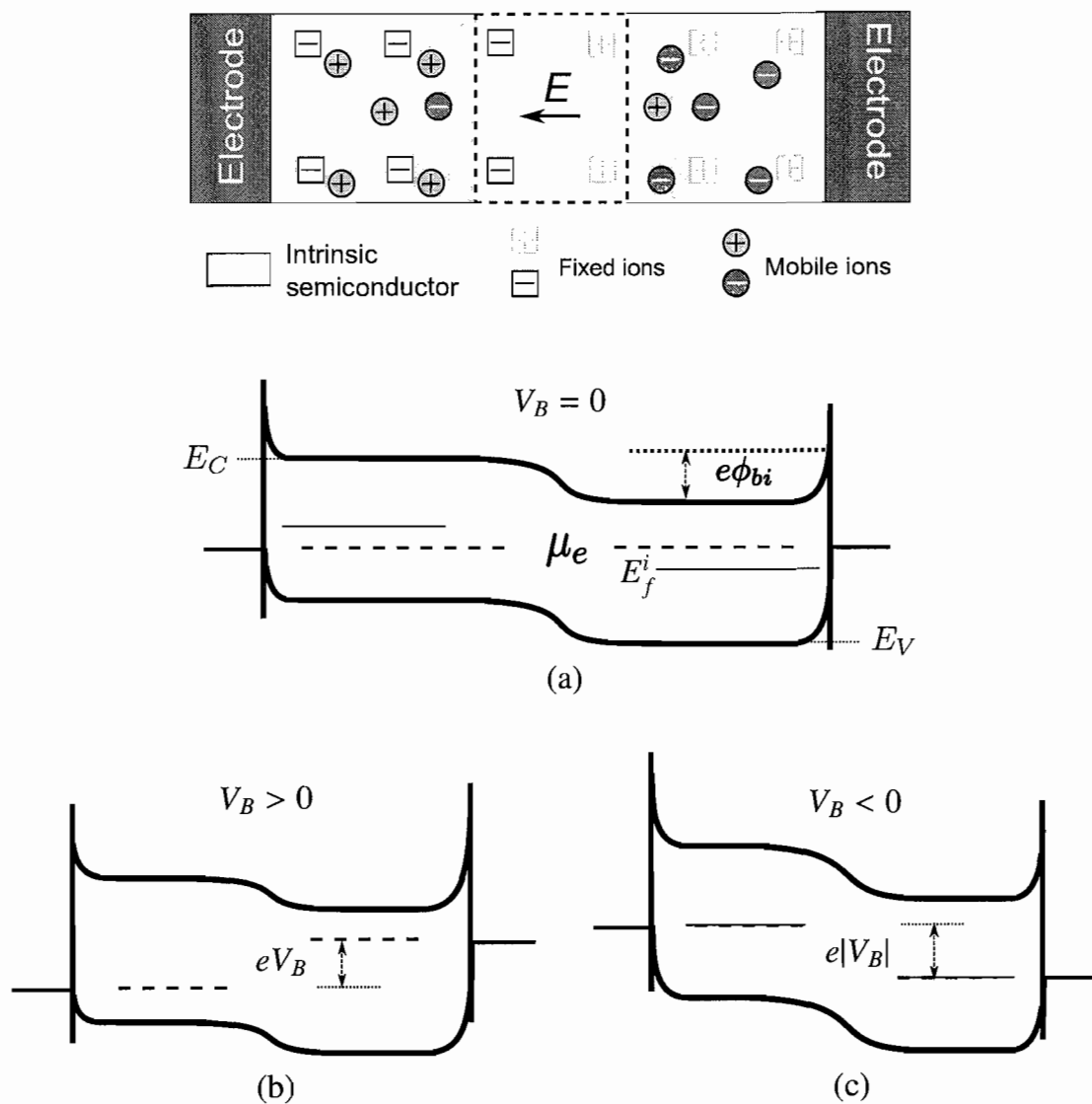
FIGURE 5.18: A schematic of the electronic energy levels of the Au|PA$_A$|PA$_C$|Au junction at zero bias (a), forward bias (b), and reverse bias (c). E_f^i is the intrinsic Fermi level, and μ_e is the chemical potential of electrons.

The charge compensation for the injected electronic charge carriers under reverse bias is, however, more difficult compared to that under forward bias, since the injected electrons in the PA_A layer will have to be compensated by the additional accumulation of mobile cations in the PA_A layer in excess of the density of fixed anions (and vice versus for hole injection into PA_C). The accumulation of excess cations in PA_A is against the process of cation diffusion into PA_C as a result of the concentration gradient across the $PA_A|PA_C$ interface. This accumulation will inevitable widen the depletion region thus increasing the potential difference across the depletion region. Therefore the doping level in both the PA_A layer and the PA_C layer are limited by the capacitance of the depletion region when the junction is under reverse bias. The relationship between the short-circuit charge and bias magnitude shown in Fig-5.8 for reverse biases of $|V_B|>1.3$ V was indeed similar to the charge-voltage relation of a capacitor with 6 $\mu F/cm^2$ capacitance.

The working mechanism of a mix-conducting $Au|PA_A|PA_C|Au$ junction as described by the above dynamic pn junction model is fundamentally different from that of a purely electronic pn junction, in that the doping level of each ionomer layer is dynamically changing with the applied bias, and the asymmetry in the I-V response is the consequence of a difference in the achievable doping level between forward and reverse bias. The dynamic pn junction model also suggest that a smaller effective capacitance of the $PA_A|PA_C$ interface could improve the rectification ratio of the junction by reducing the achievable doping level at reverse biases.

According to the dynamic pn junction model, the magnitude of the built-in potential ϕ_{bi} at zero bias can be estimated through the equilibrium conditions for the mobile charge carriers. The PA_A side of the device will be referred to as the "left" side and the PA_C side of the device the "right" side. For simplicity, it is assumed that ions are completely dissociated and that all charge densities are symmetric with respect to the $PA_A|PA_C$ interface, the mobile cation (anion) concentration in the PA_A layer is the same as the mobile anion (cation) concentration in the PA_C layer,

i.e. $n_C^L = n_A^R$ and $n_A^L = n_C^R$, and the hole (electron) concentration in the PA$_C$ layer is the same as the electron (hole) concentration in the PA$_A$ layer, i.e. $n_h^L = n_e^R$ and $n_e^L = n_h^R$.

At zero bias, the equilibrium of mobile cations and electrons requires that:

$$\phi_{bi} = \frac{k_B T}{q} \ln \frac{n_C^L}{n_C^R} = \frac{k_B T}{q} \ln \frac{n_e^R}{n_e^L} \tag{5.1}$$

where k_B is the Boltzmann constant, T is temperature, and q is the charge of a proton. Eq. (5.1) implies that:

$$n_C^L n_e^L = n_C^R n_e^R$$

Local neutrality further requires that:

$$n_h^L \approx n_h^L - n_e^L = n_0 + n_A^L - n_C^L \approx 2n_A^L \tag{5.2}$$

where n_0 is the density of fixed ions. Therefore

$$n_C^L n_e^L \approx 2(n_C^R)^2$$

with the law of mass action for electronic charge carries, $n_i^2 = n_e^L n_h^L = n_e^R n_h^R$, and Eq. (5.2) we then have:

$$n_C^L n_i^2 \approx 4(n_C^R)^3 \tag{5.3}$$

Combining Eq. (5.3) with Eq. (5.1) gives:

$$\phi_{bi} = \frac{k_B T}{q} \ln \frac{n_C^L}{n_C^R} = \frac{2}{3} \frac{k_B T}{q} \ln \frac{2n_C^L}{n_i} \tag{5.4}$$

If one assumes that n_C^L always approximately equals to the stoichiometric ion density of $2 \times 10^{21}/\text{cm}^3$, Eq. (5.4) says that if the intrinsic electronic charge carrier density n_i is known then ϕ_{bi} can be estimated, and vice versus. A rough estimate of the ϕ_{bi} at zero bias base on $n_i = 2 \times 10^{11}$ /cm^3 (a band gap of $E_g = 1.4$ eV, and an equal effective density of state of $N_s = 10^{23}$ /cm^3 for both conduction band and valence band) gives $\phi_{bi} \approx 0.35$ V.

5.4 Summary

In this chapter, current-voltage and impedance measurements were used to investigate the origin of the asymmetric I-V response of the $Au|PA_A|PA_C|Au$ junction. The time evolution of the junction's overall current $I_B(t)$ under bias shows that the mobility of cations in the PA_A layer was limiting the response speed of the junction. And the bias dependance of $I_B(t)$ indicates that significant electronic charge carriers can be injected at both signs of bias.

The bias dependance of short-circuit charge indicates that the injection of electronic charge carriers at reverse bias was coupled to a non-Faradaic process that involves only interfacial capacitances, while the charge injection at forward bias was coupled to a Faradaic process that involves the capacitance of the entire ionomer layer.

Small amplitude AC impedance spectra of the $Au|PA_A|PA_C|Au$ junction at the steady-state of both forward and reverse biases indicate that the amount of injected electronic charge carriers were significantly higher at forward bias than at reverse bias of same magnitude, and that the injected holes has a higher mobility than the injected electrons.

Control experiment on $Au|PA_A|Au|PA_C|Au$ structure demonstrates that the ion transport across the $PA_A|PA_C$ interface plays a crucial role in the asymmetric I-V response of the $Au|PA_A|PA_C|Au$junction.

Based on experimental results from this chapter and previous chapters, a dynamic pn junction model was proposed to describe the working mechanism of the mix-conducting $Au|PA_A|PA_C|Au$ junction. The model was able to explain the observed changes of both the short-circuit charge and the steady-state current with applied bias. The model was then used to estimate the built-in potential across the ionic depletion region near the $PA_A|PA_C$ interface.

CHAPTER VI

PHOTOVOLTAIC RESPONSE OF POLYACETYLENE IONOMERS AND THEIR HETERO-IONIC JUNCTION

In this chapter, the photovoltaic response of the $Au|PA_A|PA_C|Au$ junction as well as each individual ionomer in $Au|Ionomer|Au$ configuration will be investigated to verify the working mechanism of the mix-conducting junction.

6.1 Introduction

The dynamic *pn* junction model that was proposed in Chapter-V as well as the ionic P-N junction hypothesis in Chapter-I suggest that one should be able to observe photovoltaic response from the $Au|PA_A|PA_C|Au$ junction, owing to the existence of the built-in electric field and the fact that photo-generation of charge carriers in polyacetylene has been observed to have reasonably high efficiency.[82, 83, 9]

Photovoltaic response, however, was not observed in the earlier studies on the $Au|PA_A|PA_C|Au$ junction.[19] Less than optimal experimental design and sample quality as well as an inefficient energy conversion process may have prevented the discovery of such photovoltaic response. During the experiments in previous chapters, it was found that internal micro shorts having resistance on the order of $M\Omega$ often exist in some samples but are not readily detectable unless the sample is dried and carefully tested. Such micro shorts could have made photovoltage much harder to detect if the signal was weak.

With improved sample quality and optimized instrument set up, the photovoltaic response of the $Au|PA_A|PA_C|Au$ junction as well as the single-layer $Au|Ionomer|Au$ structure will be investigated in this chapter, to verify whether dissimilar self-

doping of the PA_A and PA_C layer predicted by the model will indeed lead to photovoltaic response in a mix-conducting hetero-ionic junction that otherwise has nearly symmetric electronic properties.

6.2 Experimental details

Bi-layer $Au|PA_A|PA_C|Au$ samples and single-layer $Au|Ionomer|Au$ samples were prepared and annealed following the same procedures as described in the experimental details section in Chapter-II. The sample was kept under vacuum (P<20 mTorr) during all experiments.

A Keithley 236 Source-Measure Unit was used for both photocurrent and photovoltage measurements. A custom Labview program was used for controlling the instrument and recording data. The light source used for photovoltaic response experiments was either a 30 mW green diode Laser at $\lambda = 532$ nm with a beam size of about 1 mm, or a tunable 5W Diode-Pumped Solid-State Laser from Coherent, Inc. that has a beam size of about 3 mm.

6.3 Results and discussion

In presenting the results throughout this chapter, the positive electrode refers to the electrode that was interfaced with the PA_A layer for $Au|PA_A|PA_C|Au$ samples, and refers to the top electrode for $Au|Ionomer|Au$ samples. During laser illumination, if light enters the sample through the top electrode (which is also the electrode connecting to the PA_A layer for $Au|PA_A|PA_C|Au$ samples), it is referred to as "Front illumination" .

6.3.1 The time evolution of photovoltaic response

When a $Au|PA_A|PA_C|Au$ sample that is free from micro electrical shorts was illuminated by a 30 mW green laser at $\lambda = 532$ nm, photovoltaic response was

indeed observed. The open-circuit voltage V_{OC} of a 270|200 nm Au|PA$_A$|PA$_C$|Au sample under the back (PA$_C$) side illumination of a focused 30 mW green laser is shown in Fig-6.1 as a function of time.
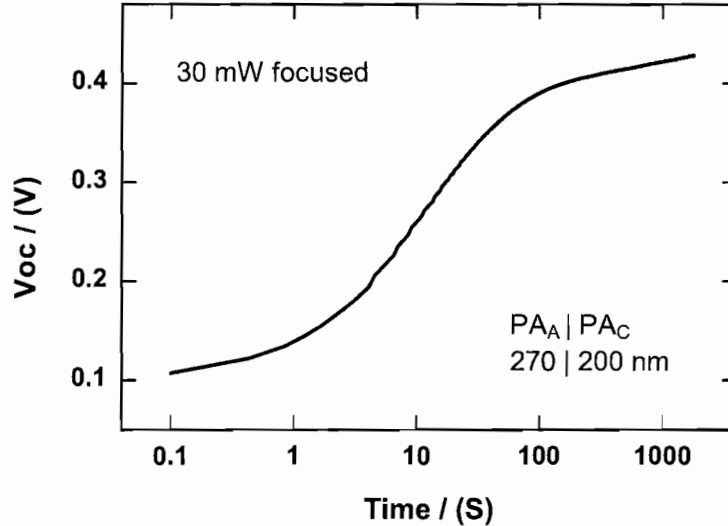
FIGURE 6.1: The change of open-circuit voltage with time of a Au|PA$_A$|PA$_C$|Au sample illuminated by a focused 30 mW laser at λ=532 nm.

It is seen that the open-circuit voltage started off at about 0.1 V and increases substantially during the fist minute under illumination before leveling off slowly at longer time with a final value of about 0.43 V at $t = 30$ minute. The time scale of this slow rise in V_{OC}(t) is typical of the cation redistribution in the PA$_A$ layer, as can be seen by a comparison between Fig-6.1 and Fig-5.1 in Chapter-V. The time dependance of V_{OC}(t) indicates that the generation and separation of electronic charge carriers has lead to the corresponding redistribution of compensating ions.

6.3.2 Dependence on illuminating direction

To rule out the possibility that the photovoltaic response could result from the two electrode interfaces through an asymmetry in light intensity due to absorption of the material, the responses of a 160|150 nm Au|PA$_A$|PA$_C$|Au sample under both

front (PA$_A$) side and back (PA$_C$) side illumination were compared in Fig-6.2. The response of the short-circuit current to light is shown in the top panel, while the response of V_{OC}(t) is shown in the bottom panel.
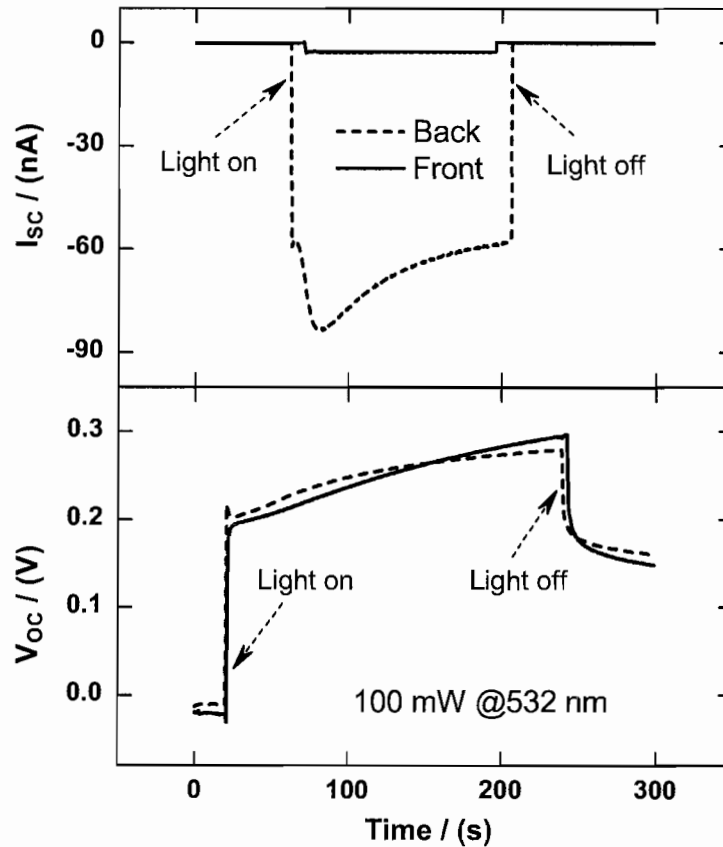
FIGURE 6.2: The response of a Au|PA$_A$|PA$_C$|Au sample to the illumination of a 100 mW green light at λ=532 nm, with a beam size slightly larger than the sample area of 0.125 cm^2. The change of current with the on/off of illumination is shown in the top graph, and the change in open-circuit voltage is shown in the bottom graph. Solid lines: illuminated from the PA$_C$ side. Dashed lines: illuminated from the PA$_A$ side.

It can be seen from Fig-6.2 that the sign of both short-circuit current and open-circuit voltage didn't change with the direction of illumination. It is interesting that, although the open-circuit voltages are similar for both back and front illumination,

the short-circuit current during the font illumination was much lower. This difference in short-circuit current between front and back illumination will be discussed later.

Given the similarity in electronic properties between the PA_A and the PA_C layer, the unidirectional photovoltaic response of the $Au|PA_A|PA_C|Au$ structure strongly suggests that the preferential separation of photon generated holes and electrons resulted from the asymmetry across the $PA_A|PA_C$ interface rather than from the effect of electrode interfaces.

6.3.3 Thickness dependence

Experimental results from different samples revealed that the efficiency of photo energy conversion was dependent on the sample thickness. Fig-6.3 shows the I-V curves of two samples of different thickness under same illumination condition. It is observed that the thinner sample shows a lower open-circuit voltage but a much higher short-circuit current than the thicker sample.

The thickness dependance of the open-circuit potential and short-circuit current can be explained by the effect of sample thickness on internal resistance when the $Au|PA_A|PA_C|Au$ functions as a power source under illumination. At open-circuit, the lower internal electronic resistance of the thinner sample functions as a shunt resistor and makes recombination of photon generated electrons and holes faster, thus lowering the measured open-circuit voltage. At short-circuit, however, thinner PA_A and PA_C layers (lower internal resistances) facilitate the transport of separated charge carriers to the electrodes where they are collected, therefore resulted in higher short-circuit current for the thinner sample.

6.3.4 The photoresponse of individual ionomer

For the purpose of control experiment, the response of the nominally symmetric $Au|Ionomer|Au$ structure to illumination was also investigated. The photovoltaic
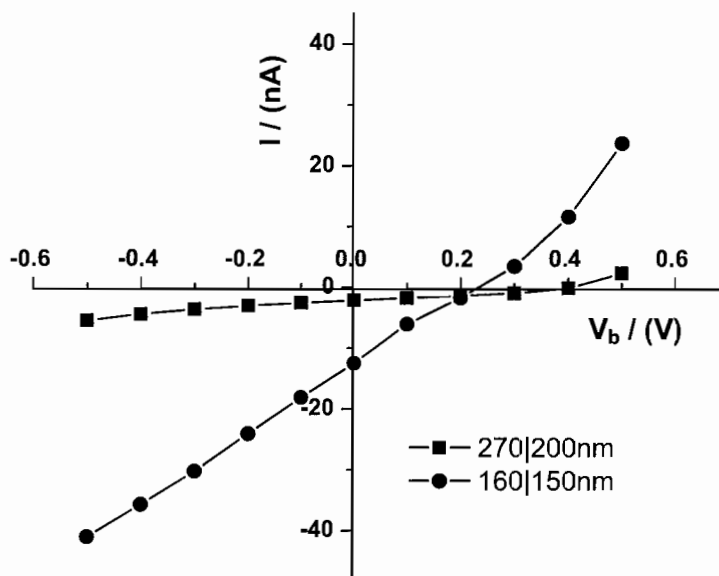
FIGURE 6.3: The I-V curve of two Au|PA$_A$|PA$_C$|Au samples of different thickenss under full device area (0.125 cm^2) illumination of a 30 mW green laser at λ=532 nm from the PA$_C$ side of the device.

response of a Au|PA$_A$|Au sample is shown in Fig-6.4 for both directions of illumination. It can be seen that the photovoltaic response of the Au|PA$_A$|Au was indeed symmetric, with the illuminated electrode always at lower potential.

The symmetric response of the Au|PA$_A$|Au sample to light is consistent with the built-in symmetry of the structure. While the polarity of the short-circuit current and open-circuit voltage can be explained by the difference in mobility between holes and electrons and the attenuation of light intensity within the ionomer film. The results from Chapter-III indicated that electrons are much less mobile than hole in both PA$_A$ and PA$_C$. Due to absorbtion by the material, the intensity of light is stronger at the side of incidence. When higher concentration of holes and electrons are generated near the illuminated electrode, holes will diffuse away faster than electrons which results in a higher concentration of electrons near the illuminated electrode, therefore the illuminated side is always the negative electrode. The magnitude of the
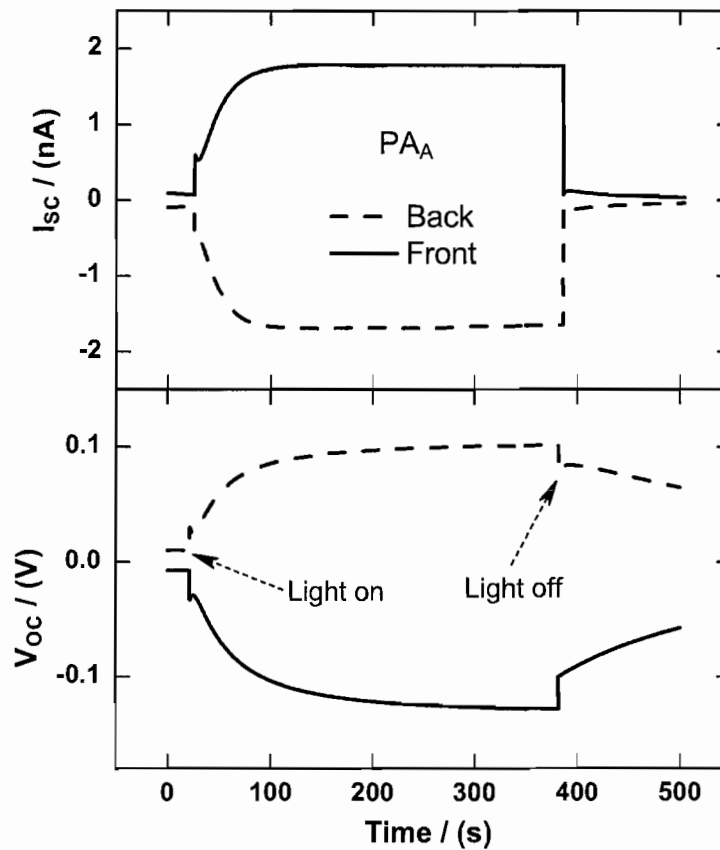
FIGURE 6.4: The response of a 560 nm Au|PA$_A$|Au sample to the illumination of a focused 30 mW green light at $\lambda=532$ nm. The change of current with the on/off of illumination is shown in the top graph, and the change in open-circuit voltage is shown in the bottom graph. Solid lines: illuminated through the top electrode. Dashed lines: illuminated through the bottom electrode. Positive potential corresponds to top electrode (+) versus bottom electrode (-).

short-circuit current and the open-circuit voltage will then depend on the absorbtion coefficient as well as the thickness of the ionomer.
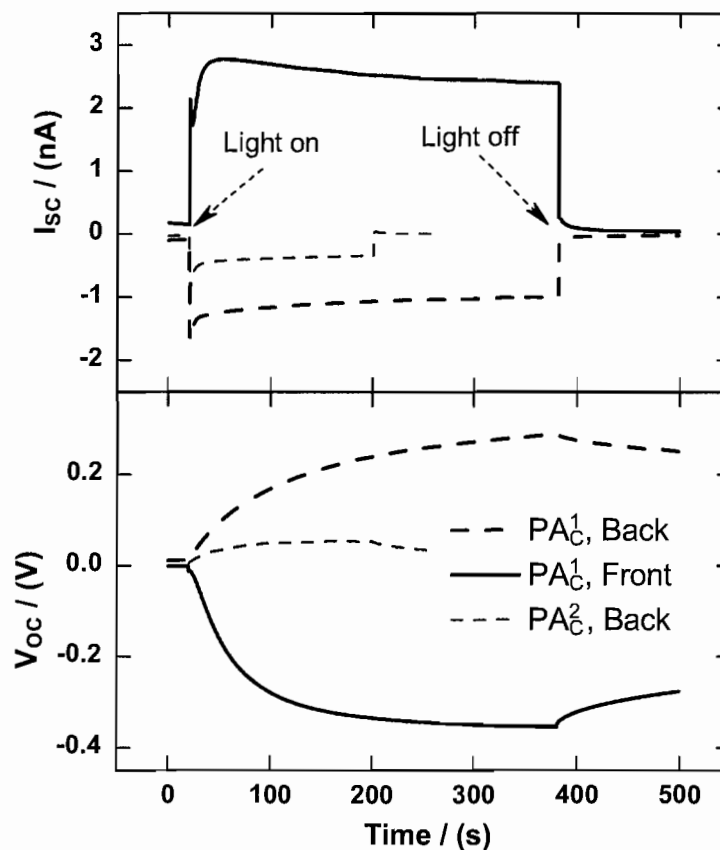
FIGURE 6.5: The photovoltaic response of two Au|PA_C|Au samples of different thickness under the illumination of a focused 30 mW green light at λ=532 nm. PA_C^1—200 nm, PA_C^2—120 nm. The change of current with the on/off of illumination is shown in the top graph, and the change in open-circuit voltage is shown in the bottom graph. Solid lines: illuminated through the top electrode. Dashed lines: illuminated through the bottom electrode. Positive potential corresponds to top electrode (+) versus bottom electrode (-).

The photovoltaic responses of two PA_C samples of different thickness are shown in Fig-6.5. For the thinner sample, only the response to back illumination is shown. It is seen that the sign of both short-circuit current and open-circuit voltage changes with illumination direction, although the magnitudes of I_{SC} and V_{OC} are not as symmetric

as that of the PA_A sample (Fig-6.4) upon switching illumination direction. The difference in the magnitude of response between front and back illumination might be attributed to a difference in optical path, and hence intensity loss due to interfacial reflection, between the two illumination directions, because the bottom (back) Au electrode is in contact with glass substrate while the top (front) Au electrode is in contact with air. The thinner sample was observed to exhibit substantially lower magnitude of both short-circuit current and open-circuit voltage under the same illumination condition, presumably due to a smaller difference in carrier concentration between the front and back electrode interfaces.

6.3.5 Light intensity dependence of the response

The light intensity dependance of the open-circuit voltage and short-circuit current for the $Au|PA_A|PA_C|Au$ junction was also investigated. the It is seen from Fig-6.1 and Fig-6.2 that both V_{OC} and I_{SC} evolve with time under continuous illumination, therefore to compare the responses at different light intensity, the open-circuit voltage and short-circuit current values at $t \approx 200$ seconds was used based on the observation from Fig-6.1 that the change in $V_{OC}(t)$ was slow after 200 seconds of illumination. The intensity dependance of V_{OC} and I_{SC} for a 160|150 nm $Au|PA_A|PA_C|Au$ sample is shown in Fig-6.6 as a function of laser output power. Since the laser beam spot size doesn't change during the experiment, the light intensity is directly proportional to laser power.

From Fig-6.6, it is observed that the short-circuit current of the $Au|PA_A|PA_C|Au$ junction increases with increasing laser power, while the V_{OC} increases initially then saturates at about 400 mW. Consistent with the observation in Fig-6.2, illuminating the sample from the PA_A side resulted in significantly lower short-circuit current than illuminating from the PA_C side, although the ratio between the I_{SC} of back illumination and the I_{SC} of front illumination decreases with increasing light intensity. The open-circuit voltage differs to a much lesser extend compared to short-circuit
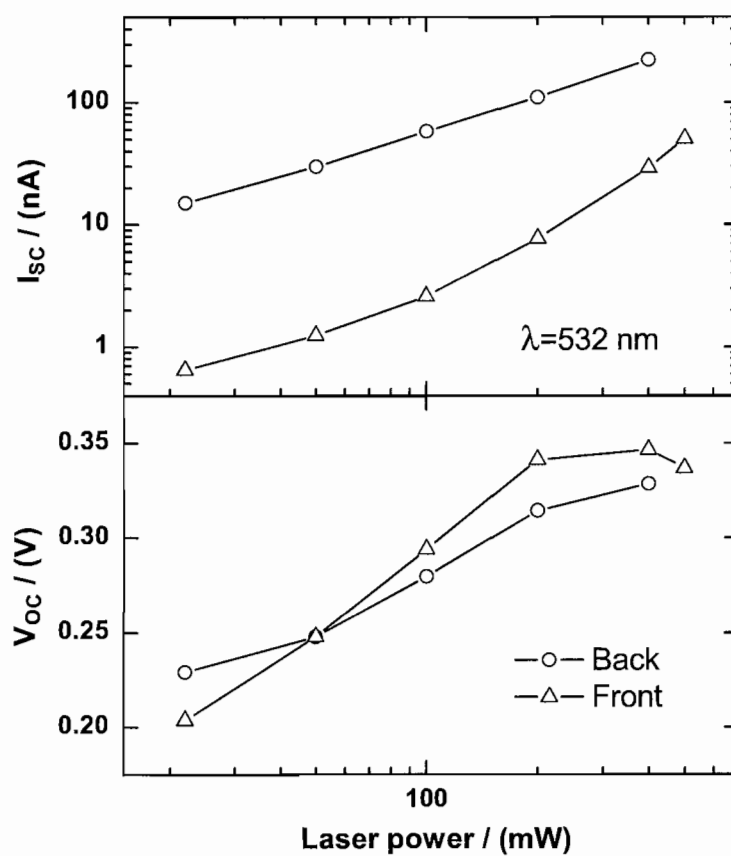
FIGURE 6.6: Light intensity dependance of the photovoltaic response for a 160|150 nm $Au|PA_A|PA_C|Au$ sample, under full device area (0.125 cm^2) illumination of green laser at $\lambda=532$ nm.

current upon switching illuminating direction. At lower light intensity (<50 mW), the sample shows lower V_{OC} under front illumination but the difference reverses at higher light intensity.

6.3.6 Photovoltaic response of the ionomer junction

The observed photovoltaic response of the Au|PA$_A$|PA$_C$|Au junction can be explained by the dynamic pn junction model proposed in the previous chapter. A schematic of the junction's response to uniform illumination according to the dynamic pn junction model is shown in Fig-6.7. The electronic properties of PA$_A$ and PA$_C$ are assumed to be identical.

In the absence of light, the PA$_A$ layer and the PA$_C$ layer are p-doped and n-doped, respectively, due to the equilibration of mobile charges across the PA$_A$|PA$_C$ interface, but the chemical potential of electrons is uniform throughout the device. The open-circuit potential V_{OC} is therefore zero.

When the Au|PA$_A$|PA$_C$|Au junction is uniformly illuminated, in the bulk of the junction the excitation of electrons from valence band to conduction band moves the quasi Fermi level of the electrons in the valence band, E_{fv}, closer to the valence band edge while at the same time also moves the quasi Fermi level of the electrons in the conduction band, E_{fc}, closer to the conduction band edge. This splitting between E_{fv} and E_{fc} enables the junction under illumination to supply electric power to the external circuit. For a material with intrinsic electron density n_i, the splitting between E_{fc} and E_{fv} is determined by the steady-state electron and hole concentration, n_e and n_h, under illumination through the relation:

$$E_{fc} - E_{fv} = k_B T \ln \frac{n_e n_h}{n_i^2} \qquad (6.1)$$

In the p-type material, the difference between E_{fv} and the unilluminated Fermi level is smaller than the difference between E_{fc} and the unilluminated Fermi level due to the higher concentration of holes already exist, and the opposite is true in the n-type
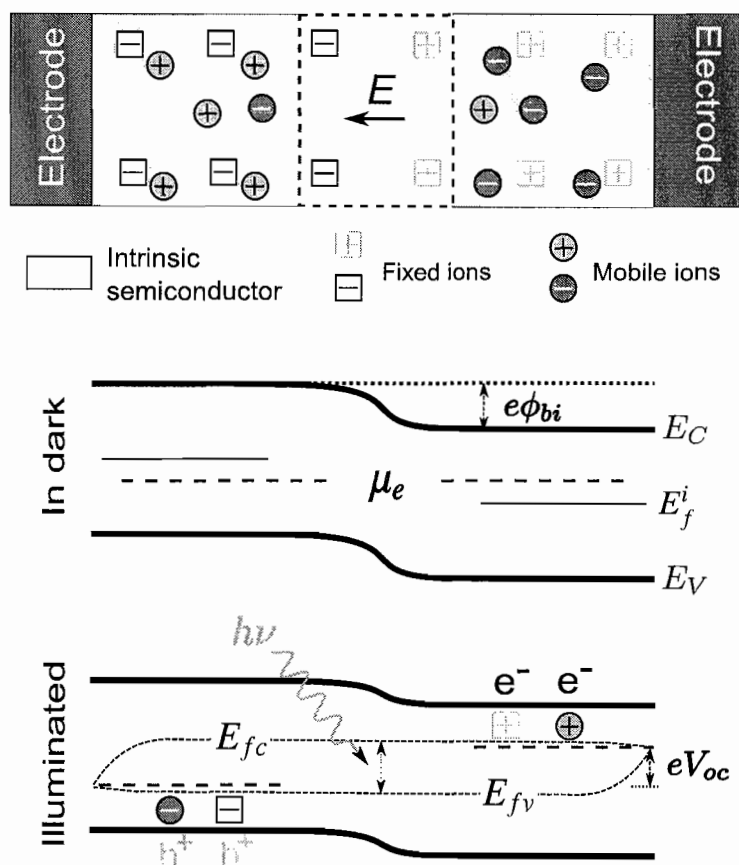
FIGURE 6.7: A schematic of the photovoltaic response of a $\mathrm{Au|PA_A|PA_C|Au}$ junction. E_{fc} and E_{fv} are, respectively, the quasi Fermi levels of electrons in the conduction band and valence band under uniform illumination. μ_e is the chemical potential of electrons when the sample is in the dark.

material. Because of recombination at the electrode surface, E_{fc} and E_{fv} converges to Fermi level of each electrode.

At open-circuit, no net current should exist at steady-state throughout the junction, therefore near the electrode surface, the electronic current due to the change of E_{fc} and the hole current due to the change of E_{fv} should cancel out with each other. In the p-doped material, the conductivity of holes are much higher than the conductivity of electrons, hence the change in E_{fv} as it approaches the electrode is correspondingly slower than the change in E_{fc}, and the opposite changes happen in the n-doped material. The offset between the Fermi level of the electrode in contact with the p-doped material and the Fermi level of the electrode in contact with the n-doped material determines the maximum energy that can be extracted by recombining an electron-hole pair through the external circuit, which is eV_{OC}.

In a pure electronic pn junction, the doping levels of both the p-type and n-type material and thus the Fermi levels of their contacting electrodes are fixed, therefore the maximum V_{OC} is fixed. In the mix-conducting hetero-ionic jucntion, however, the mobile ions can redistribute in response to changes in electronic charge carrier concentration, hence the doping levels of both the p-type and the n-type material will change accordingly until the system achieves a new equilibrium, in which the separation of equilibrium Fermi levels (determined by doping level) between the p-type material and the n-type material is close to the splitting between E_{fc} and E_{fv}. Therefore ideally the measured V_{OC} of the $Au|PA_A|PA_C|Au$ junction is determined only by the generation and recombination process in the material, i.e. $V_{OC} \approx E_{fc} - E_{fv}$. This represents a fundamental difference between a pure electronic pn junction and a mix-conducting hetero-ionic junction.

The change of doping level in the $Au|PA_A|PA_C|Au$ junction during illumination is consistent with the observation that the open-circuit voltage evolves with a time constant that is typical of ion redistribution in the PA_A, and consistent with the observed relationship between steady-state open-circuit voltage and light intensity.

Under the symmetric material assumption and relatively weak illumination ($n_C^L \approx$ constant), the open-circuit voltage of a dynamic pn junction can therefore be calculated through the following relation according to Fig-6.7 and Eq. (5.2)

$$V_{OC} = \frac{k_B T}{e} \left(2 \ln \frac{n_e^R}{n_i} - \ln \frac{n_C^L}{n_C^R} \right) = \frac{k_B T}{e} \ln \frac{(n_e^R)^3}{2 n_C^L n_i^2} \tag{6.2}$$

Where the steady-state electron concentration in the n-type (PA$_C$) material, n_e^R, changes with light intensity Φ_L.

In the case when n_e^R changes linearly with light intensity Φ_L, Eq. (6.2) predicts that within the low light intensity regime, a plot of V_{OC} versus $\ln \Phi_L$ will ideally have a slope of $3k_B T/e$, or V_{OC} will change by 0.18 V per decade of change in light intensity. This prediction is supported by observation that, the linear region of V_{OC} versus log of laser power in Fig-6.6 shows a slope of $\approx 2k_B T/e$ for back illumination and a slope of $\approx 2.5 k_B T/e$ for front illumination. The weaker than predicted dependence is likely due to a sub-linear relationship between n_e^R and Φ_L as a result of the balance between carrier generation and recombination processes under illumination.

Eq. (6.2) also leads to a method for experimentally estimating the magnitude of ϕ_{bi}. Immediately after the junction is illuminated with sufficiently strong light($E_{fc} - E_{fv} \geq \phi_{bi}$), the large amount of generated electronic carriers could neutralize the ionic space charge to achieve a flat band condition before the mobile ions have time to redistribute. Therefore the initial value of V_{OC} immediately after light is turned on should ideally equal to the magnitude of ϕ_{bi}.

In the actual Au|PA$_A$|PA$_C$|Au junction, the mobility of electrons are believed to be much lower than that of holes based on the results from previous chapters, and this difference in mobility between holes and electrons has two practical implications. The first implication is that the measured V_{OC} value will be less than $E_{fc} - E_{fv}$, because near the PA$_C$|Au interface, a larger driving force for electrons (thus larger change in E_{fc}) will be needed to balance the hole current, therefore part of $E_{fc} - E_{fv}$ will have to be sacrificed.

The second implication is that the magnitude of the short-circuit current will depend on the direction of illumination if the sample is not uniformly illuminated. When the $Au|PA_A|PA_C|Au$ junction is illuminated from the PA_C side, the intensity of light in the PA_C layer will be stronger than in the PA_A layer, and more charge carriers will be generated in the PA_C layer, vice versus when the sample is illuminated from the PA_A side. Due to much higher mobility, holes in the PA_C layer will have a longer diffusion length than electrons in the PA_A layer, therefore when illuminated from the PA_A side, the number of electrons generated in the PA_A layer that are able to reach the PA_C layer and get collected will be much less than the number of holes generated in the PA_C layer that are able to reach the PA_A layer when the sample is illuminated from the PA_C side. This will result in a lower current for front illumination at the same light intensity, which was indeed observed in both Fig-6.2 and Fig-6.6.

The low mobility of electrons in both PA_A and PA_C also suggest that a potential way to improve the energy conversion efficiency of a $Au|PA_A|PA_C|Au$ junction is to make the thickness of the PA_A layer commensurate with the diffusion length of electrons in the p-doped PA_A and the thickness of the PA_C layer commensurate with the diffusion length of holes in the n-doped PA_C.

6.4 Summary

Photovoltaic responses of the $Au|PA_A|PA_C|Au$ junction as well as the single-layer $Au|Ionomer|Au$ structure were investigated in this chapter. The observation of unidirectional open-circuit voltage and short-circuit current on the $Au|PA_A|PA_C|Au$ junction under illumination indicates that the PA_A layer was p-doped and the PA_C layer was n-doped at steady-state. And the change of open-circuit voltage with time under continuous illumination further suggests that ion redistribution was involved during the system's evolution to steady-state.

The symmetric photovoltaic response of the single-layer $Au|Ionomer|Au$ structure, and the dependence of the $Au|PA_A|PA_C|Au$ structure's short-circuit current on

illumination direction supports the assumption that the mobility of electrons are lower than the mobility of holes in both PA$_A$ and PA$_C$.

Light intensity dependence of the Au|PA$_A$|PA$_C$|Au junction's open-circuit voltage in the weak illumination regime was found to be consistent with the prediction of the dynamic pn junction model.

CHAPTER VII

CONCLUSIONS AND FUTURE WORK

7.1 Conclusions

The work in this dissertation seeks to understand the interaction between ionic charge transport and electronic charge transport in mixed ionic-electronic conductor systems, with a particular focus on identifying the mechanism of asymmetric electronic charge transport in hetero-ionic MIEC junctions in which the two constituent materials have opposite signs of mobile ions. To address the discrepancies between two existing hypotheses about the origin of asymmetric electronic charge transport in hetero-ionic MIEC junctions, a series of current-voltage and AC impedance experiments as well as photoresponse experiments were carried out on anionically and cationically functionalized polyacetylenes, PA_A and PA_C, respectively, and their junctions.

Small amplitude AC impedance spectroscopy was first used in Chapter-II to investigate the ionic charge transport in both PA_A and PA_C. The results provided important information about the ionic aspects of each ionomer such as the ionic conductivity, the activation energy of ion transport, and the Debye length of ionic double layer near the electrode-ionomer interface. The impedance experiment revealed that although the ionic conductivity of the PA_A was lower than that of the PA_C by about an order of magnitude at same temperature, the interfacial ionic double layer capacitance of the PA_A was about twice that of the PA_C. Modeling of the impedance data also suggested that ions are fully dissociated in both the PA_A and the PA_C, and the mobile ions seemed to be moving in a crowded environment.

Comparison of impedance experiment results among the $Au|PA_A|Au$ structure, the $Au|PA_C|Au$ structure, and the hetero-ionic $Au|PA_A|PA_C|Au$ structure indicates that an interfacial capacitance exists at the $PA_A|PA_C$ interface.

The process of electronic charge injection from Au electrode into each ionomer at the presence of electrolyte was investigated in Chapter-III through the use of symmetric electrochemical cell, in which the electronic conduction pathway within the ionomer was intentionally disrupted. The results of electronic charge injection experiment revealed that holes can be easily injected into both the PA_A and the PA_C, and the injection process was coupled to the charging of an ionic double layer at the opposite electrode until electron injection begins. The onset voltages for electron injection into the PA_A and the PA_C were found to be similar, although the injection of electrons into the PA_A was found to be less reversible. This experiment also revealed that the injection of holes into both ionomers leads to much more significant increase in the electronic conductivity of the material than the injection of electrons, which indicates that holes are more mobile than electrons in both the PA_A and the PA_C. The impact of different coupling mechanisms (Faradaic vs. non-Faradaic) between ionic and electronic charge carriers in an electrochemical transistor on the device's performance was also demonstrated in Chapter-III.

Current-voltage experiments on single-layer $Au|PA_A|Au$ structure and $Au|PA_C|Au$ structure in Chapter-IV clearly demonstrated that ion redistribution within the ionomer leads to enhanced injection of electronic charge carriers into the ionomer, which in turn leads to substantial increase in the material's electronic conductivity. Comparison of experiment results between the two materials further revealed that the electrical response of the PA_A and the PA_C are indeed very similar despite there significant difference in ionic conductivity, and the response time of the mix-conducing system was determined by the redistribution time of the mobile ions.

The similarities between the $Au|PA_A|Au$ structure and the $Au|PA_C|Au$ structure in both electronic charge carrier injection process and steady-state current-voltage

relationship, together with the finding that the ionic double layer capacitance of the two structures only differ by less than a factor of two lead to the conclusion that, the asymmetric I-V response of the $Au|PA_A|PA_C|Au$ structure must originated from the asymmetry in ionic transport across the $PA_A|PA_C$ interface.

The $Au|PA_A|PA_C|Au$ junction's time dependent response to constant applied biases as well as its steady-state properties at each bias were then investigated in Chapter-V for the purpose of understanding how the overall electronic conductivity of the $Au|PA_A|PA_C|Au$ junction was coupled to the asymmetric transport of ions across the $PA_A|PA_C$ interface. Comparison of the amount of injected electronic charges between forward and reverse biases revealed that significant amount of electronic charges can be injected in both bias directions, but the charge injection at reverse biases was coupled to the ionic capacitance of the $PA_A|PA_C$ interface. A control experiment further demonstrated that once the transport of mobile ions across the $PA_A|PA_C$ interface is blocked, the asymmetry in electronic transport disappears. Impedance response of the $Au|PA_A|PA_C|Au$ junction under constant bias indicated that the injected holes have a much higher mobility than the injected electrons.

Analysis of the above experimental findings eventually lead to the proposal of a dynamic pn junction model to describe the working mechanism of the $Au|PA_A|PA_C|Au$ junction. This model relies on the same assumption of ionic charge equilibration across the MIEC|MIEC interface as in the existing ionic P-N junction hypothesis. In addition to a qualitative description of the interaction between the ionic and the electronic charge transport in the $Au|PA_A|PA_C|Au$ junction, the dynamic pn junction model also provides practical ways to estimate the magnitude of the built-in potential difference across the ionic depletion region, as well as providing guiding principles for improving the rectification ratio of the junction.

The dynamic pn junction model was further supported by the observation of photovoltaic response from the $Au|PA_A|PA_C|Au$ junction in Chapter-VI. The details in the $Au|PA_A|PA_C|Au$ junction's response to illumination, e.g. the time dependence

and light intensity dependence of the open-circuit voltage, can be adequately explained by the dynamic *pn* junction model and the ionomers' specific properties, e.g. mobility difference between electrons and holes. The photovoltaic response of the $Au|PA_A|PA_C|Au$ junction also highlighted a fundamental difference between the working mechanism of a pure electronic *pn* junction and a mix-conducting hetero-ionic junction, in that the doping level of a mix-conducting junction changes with the level of photo excitation.

In summary, experimental investigations in this dissertation have provided important knowledge about the interaction between ionic and electronic charge transports in mix-conducting polyacetylene ionomers and their junctions. The work in this dissertation also resulted in an improved model of hetero-ionic MIEC junctions that is capable of quantitatively describing the current-voltage, AC impedance, and photovoltaic responses of such junction.

7.2 Future work

According to the dynamic *pn* junction model, one unique property of a mix-conducting hetero-ionic junction is its ability to dynamically adjust its doping level to match the level of photo excitation, there is only minimum doping when the junction is in the dark. This could be advantageous as organic solar energy conversion devices, since organic semiconductors tend to degrade faster when doped.[84] Therefore, one possible future direction is to explore new materials and optimize the device structure of mix-conducting hetero-ionic junctions for photovoltaic applications.

The work in Chapter-IV has shown that the ion mobility in MIECs doesn't seem to have a significant effect on the steady-state electronic transport except for changing the response time of the device. But the effect of ion concentration on electronic charge transport has not been systematically explored. This offers another possible direction for future investigation of MIEC systems.

BIBLIOGRAPHY

[1] C. K. Chiang, C. R. Fincher, Y. W. Park, A. J. Heeger, H. Shirakawa, E. J. Louis, S. C. Gau, and A. G. Macdiarmid, "Electrical-Conductivity in Doped Polyacetylene," Phys. Rev. Lett. **39**, 1098–1101 (1977).

[2] Q. B. Pei, G. Yu, C. Zhang, Y. Yang, and A. J. Heeger, "Polymer Light-Emitting Electrochemical-Cells," Science **269**, 1086–1088 (1995).

[3] Q. B. Pei, Y. Yang, G. Yu, C. Zhang, and A. J. Heeger, "Polymer light-emitting electrochemical cells: In situ formation of a light-emitting p-n junction," J. Am. Chem. Soc. **118**, 3922–3929 (1996).

[4] J. Gao and J. Dane, "Planar polymer light-emitting electrochemical cells with extremely large interelectrode spacing," Appl. Phys. Lett. **83**, 3027–3029 (2003).

[5] L. Edman, "Bringing light to solid-state electrolytes: The polymer light-emitting electrochemical cell," Electrochim. Acta **50**, 3878–3885 (2005).

[6] J. Gao, G. Yu, and A. J. Heeger, "Polymer p-i-n junction photovoltaic cells," Adv. Mater. **10**, 692–695 (1998).

[7] K. M. Coakley and M. D. McGehee, "Conjugated polymer photovoltaic cells," Chem. Mater. **16**, 4533–4542 (2004).

[8] G. Yu, J. Gao, J. C. Hummelen, F. Wudl, and A. J. Heeger, "Polymer Photovoltaic Cells - Enhanced Efficiencies Via a Network of Internal Donor-Acceptor Heterojunctions," Science **270**, 1789–1791 (1995).

[9] A. Moliton and R. C. Hiorns, "Review of electronic and optical properties of semiconducting pi-conjugated polymers: applications in optoelectronics," Polym. Int. **53**, 1397–1412 (2004).

[10] S. Gunes, H. Neugebauer, and N. S. Sariciftci, "Conjugated polymer-based organic solar cells," Chem. Rev. **107**, 1324–1338 (2007).

[11] J. A. Rogers and Z. Bao, "Printed plastic electronics and paperlike displays," J Polym Sci Pol Chem **40**, 3327–3334 (2002).

[12] F. Eder, H. Klauk, M. Halik, U. Zschieschang, G. Schmid, and C. Dehm, "Organic electronics on paper," Appl. Phys. Lett. **84**, 2673–2675 (2004).

[13] X. Yang and J. Loos, "Toward high-performance polymer solar cells: The importance of morphology control," Macromolecules **40**, 1353–1362 (2007).

[14] K. H. Lee, G. Lee, K. Lee, M. S. Oh, and S. Im, "Flexible low voltage nonvolatile memory transistors with pentacene channel and ferroelectric polymer," Appl. Phys. Lett. **94**, – (2009).

[15] J. Gao, G. Yu, and A. J. Heeger, "Polymer light-emitting electrochemical cells with frozen p-i-n junction," Appl. Phys. Lett. **71**, 1293–1295 (1997).

[16] J.-H. Shin, S. Xiao, A. Fransson, and L. Edman, "Polymer light-emitting electrochemical cells: Frozen-junction operation of an ïonic liquiddevice," Appl. Phys. Lett. **87**, 043 506/1–043 506/3 (2005).

[17] M. R. Pinto and K. S. Schanze, "Conjugated polyelectrolytes: Synthesis and applications," Synthesis-Stuttgart pp. 1293–1309 (2002).

[18] C. H. W. Cheng and M. C. Lonergan, "A conjugated polymer pn junction," J. Am. Chem. Soc. **126**, 10 536–10 537 (2004).

[19] C. H. W. Cheng, S. W. Boettcher, D. H. Johnston, and M. C. Lonergan, "Unidirectional current in a polyacetylene hetero-ionic junction," J. Am. Chem. Soc. **126**, 8666–8667 (2004).

[20] D. A. Bernards, S. Flores-Torres, H. D. Abruna, and G. G. Malliaras, "Observation of electroluminescence and photovoltaic response in ionic junctions," Science **313**, 1416–1419 (2006).

[21] B. Lovrecek, A. Despic, and J. O. Bockris, "Electrolytic junctions with rectifying properties," J. Phys. Chem. **63**, 750–751 (1959).

[22] R. P. Buck, N. A. Surridge, and R. W. Murray, "Liquid Solid Polyelectrolyte Diodes and Semiconductor Analogs," J. Electrochem. Soc. **139**, 136–144 (1992).

[23] C. H. W. Cheng, F. D. Lin, and M. C. Lonergan, "Charge transport in a mixed ionically/electronically conducting, cationic, polyacetylene ionomer between ion-blocking electrodes," J. Phys. Chem. B **109**, 10 168–10 178 (2005).

[24] M. C. Lonergan, C. H. Cheng, B. L. Langsdorf, and X. Zhou, "Electrochemical characterization of polyacetylene ionomers and polyelectrolyte-mediated electrochemistry toward interfaces between dissimilarly doped conjugated polymers," J. Am. Chem. Soc. **124**, 690–701 (2002).

[25] B. L. Langsdorf, <u>Synthesis, characterization, and electronic properties of soluble, ionically functionalized polyacetylene analogues</u>, Thesis (ph d), University of Oregon, 2001. (2001).

[26] A. D. Robertson, A. R. West, and A. G. Ritchie, "Review of crystalline lithium-ion conductors suitable for high temperature battery applications," Solid State Ionics **104**, 1–11 (1997).

[27] J. C. Boivin and G. Mairesse, "Recent Material Developments in Fast Oxide Ion Conductors," Chem. Mater. **10**, 2870–2888 (1998).

[28] J. J. Fontanella, M. C. Wintersgill, M. K. Smith, J. Semancik, and C. G. Andeen, "Effect of High-Pressure on Electrical Relaxation in Poly (Propylene-Oxide) and Electrical-Conductivity in Poly(Propylene Oxide) Complexed with Lithium-Salts," J. Appl. Phys. **60**, 2665–2671 (1986).

[29] M. A. Ratner and D. F. Shriver, "Ion-Transport in Solvent-Free Polymers," Chem. Rev. **88**, 109–124 (1988).

[30] F. M. Gray, <u>Solid polymer electrolytes : fundamentals and technological applications</u> (VCH, New York, NY, 1991).

[31] B. B. Owens, "Solid state electrolytes: overview of materials and applications during the last third of the Twentieth Century," J. Power Sources **90**, 2–8 (2000).

[32] M. D. Ingram, "Ionic conductivity in glass," Phys. Chem. Glasses **28**, 215–34 (1987).

[33] B. L. Langsdorf, X. Zhou, D. H. Adler, and M. C. Lonergan, "Synthesis and characterization of soluble, ionically functionalized polyacetylenes," Macromolecules **32**, 2796–2798 (1999).

[34] C. B. Gorman, E. J. Ginsburg, and R. H. Grubbs, "Soluble, Highly Conjugated Derivatives of Polyacetylene from the Ring-Opening Metathesis Polymerization of Monosubstituted Cyclooctatetraenes - Synthesis and the Relationship between Polymer Structure and Physical-Properties," J. Am. Chem. Soc. **115**, 1397–1409 (1993).

[35] J. Brandrup, E. H. Immergut, and E. A. Grulke, <u>Polymer handbook</u> (Wiley, New York :, 1999), 4th ed edn.

[36] Y. Segui, B. Ai, C. Bagnol, J. Pistre, Y. Danto, and A. S. Barriere, "Metal electrode diffusion into polymer films," J. Appl. Phys. **50**, 2973–4 (1979).

[37] C. von Bechtolsheim, V. Zaporojtchenko, and F. Faupel, "Interface structure and formation between gold and trimethylcyclohexane polycarbonate," J. Mater. Res. **14**, 3538–3543 (1999).

[38] P. A. M. Steeman and J. Vanturnhout, "Fine-Structure in the Parameters of Dielectric and Viscoelastic Relaxations," Macromolecules **27**, 5421–5427 (1994).

[39] S. Zhang, S. Dou, R. H. Colby, and J. Runt, "Glass transition and ionic conduction in plasticized and doped ionomers," J. Non-Cryst. Solids **351**, 2825–2830 (2005).

[40] A. K. Jonscher, "Universal Dielectric Response," Nature **267**, 673–679 (1977).

[41] J. R. Macdonald, "Universality, the Barton Nakajima Namikawa relation, and scaling for dispersive ionic materials," Phys. Rev. B **71**, – (2005).

[42] J. R. Macdonald, "Accurate fitting of immittance spectroscopy frequency-response data using the stretched exponential model," J. Non-Cryst. Solids **212**, 95–116 (1997).

[43] J. R. Macdonald and L. D. Potter, "A Flexible Procedure for Analyzing Impedance Spectroscopy Results - Description and Illustrations," Solid State Ionics **24**, 61–79 (1987).

[44] P. B. Macedo, C. T. Moynihan, and R. Bose, "Role of Ionic Diffusion in Polarization in Vitreous Ionic Conductors," Phys. Chem. Glasses **13**, 171–179 (1972).

[45] G. Williams and D. C. Watts, "Non-Symmetrical Dielectric Relaxation Behaviour Arising from a Simple Empirical Decay Function," Transactions of the Faraday Society **66**, 80 (1970).

[46] J. R. Macdonald, "Frequency-Response of Unified Dielectric and Conductive Systems Involving an Exponential-Distribution of Activation-Energies," J. Appl. Phys. **58**, 1955–1970 (1985).

[47] H. Scher and M. Lax, "Impurity Hopping Conduction as a Continuous Time Random-Walk," Bulletin of the American Physical Society **17**, 30 (1972).

[48] J. R. Macdonald, "Conductivity of disordered solids: Resolution of discrepancies between micro- and macro-response models," Phys. Rev. B **6305**, – (2001).

[49] J. R. Macdonald and J. C. Phillips, "Topological derivation of shape exponents for stretched exponential relaxation," J. Chem. Phys. **122**, – (2005).

[50] D. P. Almond, G. K. Duncan, and A. R. West, "The Determination of Hopping Rates and Carrier Concentrations in Ionic Conductors by a New Analysis of Ac Conductivity," Solid State Ionics **8**, 159–164 (1983).

[51] O. L. Anderson and D. A. Stuart, "Calculation of activation energy of ionic conductivity in silica glasses by classical methods," J. Am. Ceram. Soc. **37**, 573–80 (1954).

[52] R. A. Huggins, in <u>Diffusion in solids: recent developments</u>, A. S. Nowick and J. J. Burton, eds. (Academic Press, New York, 1975), p. 491.

[53] D. Ravaine and J. L. Souquet, "Thermodynamic Approach to Ionic-Conductivity in Oxide Glasses .1. Correlation of Ionic-Conductivity with Chemical Potential of Alkali Oxide in Oxide Glasses," Phys. Chem. Glasses **18**, 27–31 (1977).

[54] C. K. Chiang and A. D. Franklin, "Electrical impedance spectra of trans-polyacetylene," Solid State Commun. **40**, 775–9 (1981).

[55] P. M. Grant and M. Krounbi, "Ac Conductivity of Semiconducting Trans-Polyacetylene," Solid State Commun. **36**, 291–295 (1980).

[56] R. J. Klein, S. Zhang, S. Dou, B. H. Jones, R. H. Colby, and J. Runt, "Modeling electrode polarization in dielectric spectroscopy: Ion mobility and mobile ion concentration of single-ion polymer electrolytes," J. Chem. Phys. **124**, 144 903/1–144 903/8 (2006).

[57] J. R. Macdonald, "Theory of space-charge polarization and electrode-discharge effects," J. Chem. Phys. **58**, 4982–5001 (1973).

[58] W. Scheider, "Theory of the frequency dispersion of electrode polarization. Topology of networks with fractional power frequency dependence," J. Phys. Chem. **79**, 127–36 (1975).

[59] A. Wagner and H. Kliem, "Dispersive ionic space charge relaxation in solid polymer electrolytes. I. Experimental system polyethylene oxide," J. Appl. Phys. **91**, 6630–6637 (2002).

[60] P. Gonon and F. El Kamel, "Dielectric response of cu/amorphous BaTiO3/Cu capacitors," J. Appl. Phys. **101**, – (2007).

[61] F. L. Klavetter and R. H. Grubbs, "Polyclooctatetraene (Polyacetylene) - Synthesis and Properties," J. Am. Chem. Soc. **110**, 7807–7813 (1988).

[62] H.-C. Chang and J. Geroge, "Polarization in Electrolytic Solutions. Part I. Theory," The Journal of Chemical Physics **20**, 1071–1077 (1952).

[63] J. R. Macdonald, "Theory of ac Space-Charge Polarization Effects in Photoconductors, Semiconductors, and Electrolytes," Physical Review **92**, 4 (1953).

[64] R. J. Friauf, "Polarization effects in the ionic conductivity of silver bromide," J. Chem. Phys. **22**, 1329–38 (1954).

[65] J. H. Beaumont and P. W. M. Jacobs, "Polarization in potassium chloride crystals," J. Phys. Chem. Solids **28**, 657–67 (1967).

[66] M. J. Panzer, C. R. Newman, and C. D. Frisbie, "Low-voltage operation of a pentacene field-effect transistor with a polymer electrolyte gate dielectric," Appl. Phys. Lett. **86**, – (2005).

[67] H. Shimotani, G. Diguet, and Y. Iwasa, "Direct comparison of field-effect and electrochemical doping in regioregular poly(3-hexylthiophene)," Appl. Phys. Lett. **86**, – (2005).

[68] X. L. Chen, Z. N. Bao, J. H. Schon, A. J. Lovinger, Y. Y. Lin, B. Crone, A. Dodabalapur, and B. Batlogg, "Ion-modulated ambipolar electrical conduction in thin-film transistors based on amorphous conjugated polymers," Appl. Phys. Lett. **78**, 228–230 (2001).

[69] D. Nilsson, M. X. Chen, T. Kugler, T. Remonen, M. Armgarth, and M. Berggren, "Bi-stable and dynamic current modulation in electrochemical organic transistors," Adv. Mater. **14**, 51–54 (2002).

[70] W. G. Pell and B. E. Conway, "Peculiarities and requirements of asymmetric capacitor devices based on combination of capacitor and battery-type electrodes," J. Power Sources **136**, 334–345 (2004).

[71] L. Edman, M. Pauchard, D. Moses, and A. J. Heeger, "Planar polymer light-emitting device with fast kinetics at a low voltage," J. Appl. Phys. **95**, 4357–4361 (2004).

[72] G. P. Kittlesen, H. S. White, and M. S. Wrighton, "A Microelectrochemical Diode with Sub-Micron Contact Spacing Based on the Connection of 2 Microelectrodes Using Dissimilar Redox Polymers," J. Am. Chem. Soc. **107**, 7373–7380 (1985).

[73] D. Ofer, R. M. Crooks, and M. S. Wrighton, "Potential Dependence of the Conductivity of Highly Oxidized Polythiophenes, Polypyrroles, and Polyaniline - Finite Windows of High Conductivity," J. Am. Chem. Soc. **112**, 7869–7879 (1990).

[74] J. W. Thackeray, H. S. White, and M. S. Wrighton, "Poly(3-Methylthiophene)-Coated Electrodes - Optical and Electrical-Properties as a Function of Redox Potential and Amplification of Electrical and Chemical Signals Using Poly(3-Methylthiophene)-Based Microelectrochemical Transistors," J. Phys. Chem. **89**, 5133–5140 (1985).

[75] D. J. Dick, A. J. Heeger, Y. Yang, and Q. B. Pei, "Imaging the structure of the p-n junction in polymer light-emitting electrochemical cells," Adv. Mater. **8**, 985–987 (1996).

[76] H. Rudmann, S. Shimada, and M. F. Rubner, "Operational mechanism of light-emitting devices based on Ru(II) complexes: Evidence for electrochemical junction formation," J. Appl. Phys. **94**, 115–122 (2003).

[77] J. D. Slinker, J. A. DeFranco, M. J. Jaquith, W. R. Silveira, Y. W. Zhong, J. M. Moran-Mirabal, H. G. Craighead, H. D. Abruna, J. A. Marohn, and G. G. Malliaras, "Direct measurement of the electric-field distribution in a light-emitting electrochemical cell," Nat. Mater. **6**, 894–899 (2007).

[78] L. S. C. Pingree, D. B. Rodovsky, D. C. Coffey, G. P. Bartholomew, and D. S. Ginger, "Scanning kelvin probe imaging of the potential profiles in fixed and dynamic planar LECs," J. Am. Chem. Soc. **129**, 15 903–15 910 (2007).

[79] D. L. Smith, "Steady state model for polymer light-emitting electrochemical cells," J. Appl. Phys. **81**, 2869–2880 (1997).

[80] J. C. deMello, N. Tessler, S. C. Graham, and R. H. Friend, "Ionic space-charge effects in polymer light-emitting diodes," Phys. Rev. B **57**, 12 951–12 963 (1998).

[81] Q. Pei and A. J. Heeger, "Operating mechanism of light-emitting electrochemical cells," Nat. Mater. **7**, 167–167 (2008).

[82] L. Lauchlan, S. Etemad, T. C. Chung, A. J. Heeger, and A. G. Macdiarmid, "Photoexcitations in Polyacetylene," Phys. Rev. B **24**, 3701–3711 (1981).

[83] B. R. Weinberger, "Photoconductivity, Photovoltages, and Photogenerated Solitons in Polyacetylene," Phys. Rev. Lett. **50**, 1693–1696 (1983).

[84] M. S. Lee and K. C. Huang, "Photovoltaic Properties of Electrochemically Doped Polyacetylene and Its Stability," Solid State Electron **37**, 1899–1901 (1994).